

Nucleosynthesis and evolution of AGB stars in binary systems

Nucleosynthesis and evolution of AGB stars in binary systems

Nucleosynthese en evolutie van AGB sterren in dubbelstersystemen

(met een samenvatting in het Nederlands)

Proefschrift

ter verkrijging van de graad van doctor aan de Universiteit Utrecht op gezag van de rector magnificus, prof.dr. W.H. Gispen, ingevolge het besluit van het college voor promoties in het openbaar te verdedigen op dinsdag 31 oktober 2007 des middags te 12.45 uur

door

Axel Antonio Bonačić Marinović
geboren op 20 april 1977 te Santiago, Chili.

Promotor: Prof. Dr. N. Langer

Co-promotor: Dr. O. R. Pols

Contents

Curriculum Vitæ	ix
1 Introduction	1
1.1 Asymptotic giant branch stars	1
1.2 The <i>s</i> -process nucleosynthesis	2
1.3 AGB stars in binary systems	3
1.4 Systems with their primary beyond the AGB phase	4
1.5 Contribution from this thesis	6
1.5.1 Constraining unknowns in AGB evolution and nucleosynthesis	6
1.5.2 Orbital eccentricities of systems with a former AGB star	7
1.5.3 Population synthesis of barium stars with AGB mass-loss and eccentricity enhancement	8
I Nucleosynthesis in AGB stars	9
2 <i>s</i>-Process in stellar population synthesis	11
2.1 Introduction	12
2.2 The AGB models	13
2.2.1 Minimum core mass for third dredge-up	14
2.2.2 Third dredge-up efficiency	14
2.2.3 Effectiveness of ^{13}C as a neutron source	15
2.2.4 Size of the ^{13}C pocket	15
2.2.5 Mass loss	16
2.3 Population synthesis	17
2.4 Results	18

2.4.1	Intrinsic <i>s</i> -enhanced stars	20
2.4.2	Extrinsic <i>s</i> -enhanced stars	28
2.5	Conclusions and discussion	32
3	The <i>s</i>-process in MACHO 47.2496.8	35
3.1	Introduction	36
3.2	Results	39
3.3	Stellar population synthesis models	39
3.4	Conclusion	41
II	Eccentric binary systems with AGB stars	43
4	AGB stars in eccentric binary systems	45
4.1	Introduction	46
4.2	Variation of orbital parameters	47
4.2.1	Angular momentum and energy	47
4.2.2	Behaviour of the wind	49
4.3	Rate of eccentricity change	49
4.3.1	Constant wind and constant mass accretion	50
4.3.2	Accretion from a fast isotropic wind	50
4.3.3	Accretion from the slow wind of an AGB star	51
4.3.4	Mass loss from an AGB star	52
4.4	Comparison of timescales	53
4.4.1	Eccentricity of the Sirius system	54
4.4.2	Eccentricities of the barium stars	58
4.5	Conclusions	60
5	Population synthesis of eccentric barium stars	63
5.1	Introduction	64
5.2	The binary evolution models	66
5.2.1	Enhanced mass loss from AGB stars in binary systems	66
5.2.2	Mass accretion on the companion	67
5.2.3	Strength of the tidal convective dissipation	68

CONTENTS

vii

5.2.4	Variation of orbital elements due to mass loss and mass accretion . . .	68
5.2.5	Common envelope evolution	69
5.3	Population synthesis	70
5.4	Results	71
5.4.1	Analysis of systems with equal initial masses and eccentricity	72
5.4.2	Comparison of results from the 4-dimensional space of initial parameters to observational data	76
5.5	Conclusions and discussion	81
A	Details of the synthetic TP-AGB model	83
A.1	TP-AGB initial H-depleted core mass	83
A.2	CO core mass and luminosity on E-AGB phase	85
A.3	Luminosity during the TP-AGB phase	86
A.4	Radius during TP-AGB phase	88
B	Derivation of variation of orbital parameters	91
B.1	Variation of the Orbital Energy	91
B.2	Variation of the Orbital Angular Momentum	93
B.3	The Variation of the Semi-Major Axis	94
	Samenvatting	95
	Resumen	99
	Summary	103
	Acknowledgements	107

Curriculum Vitæ

Axel Bonačić Marinović was born on the 20th of April, 1977, in Santiago, Chile. He entered the School of Engineering at Pontificia Universidad Católica de Chile in 1995. In 1998 he changed his studies subject and entered the Faculty of Physics at the same university, where he obtained the degree of Licenciado in Astronomy in the beginning of 2001. He continued there his post-graduate studies working in the subject of neutron stars under the supervision of Prof. Andreas Reisenegger and obtained the degree of Magister in Physics on the 4th of September, 2003. In October of that year he moved to the Netherlands and started his PhD in Astronomy working as an Assistant in Opleiding under the supervision of Dr. Onno Pols, from the stellar evolution group lead by Prof. Norbert Langer, at the Sterrenkundig Instituut Utrecht. This thesis manuscript is based on the results of that PhD work and the defence of this thesis will take place on the 31st of October, 2007.

Chapter 1

Introduction

1.1 Asymptotic giant branch stars

Asymptotic giant branch (AGB) stars are low- to intermediate-mass stars ($M \lesssim 8 M_{\odot}$) in their final phases of evolution. Their luminosities are in the range of approximately one to a few times $10^4 L_{\odot}$ and their radii are of the order of 1-3 AU. The AGB phase of evolution begins when the star has exhausted its central helium content after the core helium burning phase. At this point the hydrogen- and helium-exhausted core becomes degenerate and is mainly composed of carbon and oxygen (C-O core). On top of the C-O core a layer of hydrogen-exhausted helium-rich material is located, and above this, lies an extended hydrogen-rich envelope, which contains most of the mass of the star. The envelope is mainly convective, excepting for a thin radiative layer at its base. The AGB phase is divided in the early (E-)AGB and the thermally pulsating (TP-)AGB phases.

During the E-AGB phase helium is burnt steadily at the base of the helium-rich layer and the ashes of this process become part of the C-O core. Thus, the star becomes more luminous and expands as its C-O core grows. If the C-O core becomes massive enough ($\gtrsim 0.65 M_{\odot}$), the highly luminous helium shell-burning drives convection in the helium layer, which joins with the convective hydrogen-rich envelope and modifies its composition. This process is known as second dredge-up. Subsequently the star is left with a thin helium-rich shell located between the C-O core and the hydrogen-rich envelope. In case the core is not massive enough to trigger a second dredge-up, the C-O core grows upward, eroding the helium-rich layer from below until the latter becomes thin. Whether second dredge-up occurs or not, the star reaches the configuration of a thin helium-rich layer (intershell) located in between the degenerate C-O core and the extended hydrogen-rich envelope. This marks the end of the E-AGB phase and the start of the TP-AGB phase.

The main source of luminosity in TP-AGB stars is hydrogen shell burning, whose ashes become part of the intershell. The intershell hence grows in mass and its temperature rises steadily, until it is hot enough to ignite helium at its base, producing a thermally unstable runaway of energy called thermal pulse (TP) which drives convection in the intershell. At

this point the helium-burning shell is extinguished. Subsequently, the intershell settles back into radiative equilibrium and the hydrogen-rich convective envelope may penetrate into the intershell, mixing material to the surface of the star. This mixing phenomenon is called third dredge-up (TDU) and enriches the stellar envelope with helium burning products. After third dredge-up takes place shell hydrogen-burning starts again. This cycle is repeated from a few to several hundred times, continuing along the TP-AGB lifetime of the star until the envelope mass is lost. Subsequently, a planetary nebula is formed and the former core of the star remains as a cooling white dwarf. For a recent review on AGB stars see Herwig (2005).

There are many uncertainties on the physics of TP-AGB stars. In particular, we still miss a clear description of the TDU phenomenon (e.g., Frost & Lattanzio 1996; Mowlavi 1999) and of the mass loss experienced by these stars (see, e.g., Marigo 2002). Observational data can help us in constraining these uncertain processes.

1.2 The *s*-process nucleosynthesis

Elements which are heavier than iron are produced mostly by neutron capture processes when heavy nuclide seeds are exposed to a significant flux of neutrons. Almost half of these heavy elements are produced via the *slow* neutron capture process (*s*-process), during which neutron densities are of the order of $\sim 10^8 \text{ n cm}^{-3}$ and hence β^- -decay rates of unstable heavy nuclides are faster than their neutron capture rates. Thus the resulting path of neutron captures follows the valley of β^- -stability in a chart of nuclides. The other half of elements heavier than iron are instead produced by the *rapid* neutron capture process (*r*-process), during which neutron densities are $\gtrsim 10^{20} \text{ n cm}^{-3}$ and hence β^- -decay rates are slower than neutron-capture rates. For a detailed review on the production of heavy elements the reader is referred to Meyer (1994).

While the details of the astrophysical site of the *r*-process, likely connected to supernova type II explosions, are still debated, it is well known that TP-AGB stars are main factories of *s*-process elements in the Universe (see, e.g., Busso et al. 1999). During the period in between thermal pulses the temperature in the intershell is high enough ($\sim 90 \times 10^6 \text{ K}$) for the $^{13}\text{C}(\alpha, n)^{16}\text{O}$ reaction to occur. This reaction can effectively provide neutrons for the *s*-process if a ^{13}C -rich region or pocket exists in the intershell. ^{13}C can be produced via the $^{12}\text{C}(p, \gamma)^{13}\text{N}(\beta^+ \nu)^{13}\text{C}$ reaction, for which protons are needed. Hence, it is commonly assumed that these protons come from the hydrogen-rich envelope and penetrate the top of the intershell after the third dredge-up has occurred, as a result of a mixing process of as yet uncertain nature. Semi-convection (Hollowell & Iben 1988), hydrodynamical overshooting (Herwig et al. 1997), rotation (Langer et al. 1999; Herwig et al. 2003), and gravity waves (Denissenkov & Tout 2003) have all been proposed. However, the description of these processes is incomplete and involves free parameters. Consequently the amount of mass in the ^{13}C pocket and the ^{13}C abundance profile inside it are still uncertain. Moreover, the abundance of the main neutron poison, ^{14}N , which steals neutrons from the *s*-process via the $^{14}\text{N}(n, p)^{14}\text{C}$ reaction, is also uncertain.

The uncertainties in the neutron source and the uncertainties in the evolution of the stellar structure affect the abundance predictions in different ways. For example, the efficiency of the third dredge-up and the extent in mass of the ^{13}C pocket both affect the enhancement of heavy elements in the star. On the other hand, the relative abundance of *s*-process elements is more or less independent of the amount of TDU, but mostly determined by the ^{13}C abundance profile. For a discussion see, e.g., Busso et al. (2001) and Lugaro et al. (2003). To obtain a better understanding of the origin of heavy elements accurate modelling of the evolution and nucleosynthesis in AGB stars is needed, which has to be verified by exhaustive comparison to observations if the many existing uncertainties are to be resolved.

1.3 AGB stars in binary systems

Stars in binary or multiple-component stellar systems are not an exception: about half of the visible stars are in these systems and this fraction is considered to be representative of that in our galaxy. These systems must be studied in addition to the single stars because the interaction between the component stars may alter their individual evolution and nucleosynthesis. Mass is the most important property of a star because it determines to first order its overall evolution and nucleosynthesis. In a binary system, the masses of the two stars are also the most important parameters because they determine the dynamics of the orbit. Stars lose mass during their life in form of a wind, particularly in their latest stages of evolution, and if they happen to be in a binary system this alters the properties of the orbit. The companion may accrete part of that mass and this will affect its evolution, by turning it into a more massive star, alter its chemical abundances, and also modify the orbit. If the binary components are sufficiently close to each other, mass can be stripped from one star by the gravitational field of its companion and this will strongly affect its evolution.

An important process affecting the orbital evolution of a binary system is tidal interaction. Tidal forces arise from the differential gravitational pull exerted on a star by its companion. They deform the star by stretching it along the line connecting both stars. If the rotation of the star is not synchronised with the orbital angular velocity, i.e., with the tidal deformation, then energy is dissipated in the deformed star. This decreases the total dynamical energy of the binary system and causes the system components to exchange angular momentum, modifying the orbital properties. The first Lagrangian point (L1), located between the two stars, is where the effective gravitational potential in a frame co-rotating with the system has a local maximum. The equipotential surface that passes by L1 has two lobes which intersect at L1 and are called Roche lobes. Each lobe contains one of the stars and determines the volume inside which a particle is bound to the star. The extreme case of tidal deformation is when a star fills its Roche lobe and part of its mass flows into the Roche lobe of the companion through L1 in a process called Roche-lobe overflow. The Roche-lobe radius is defined as the radius of a sphere containing the same volume that the Roche lobe does. This parameter is useful given that Roche lobes are not spherical, while most stellar models are. Thus it is assumed that a stellar model experiences Roche-lobe overflow when its radius is of the same size as its

Roche-lobe radius.

Mass loss and mass transfer are usually modelled in two different regimes, depending on the distance between the components. If the stars are smaller than their respective Roche lobes, their mass-loss rates are modelled as those of single stars, and their masses may be enhanced via wind accretion. On the other hand, if one of the components fills its Roche lobe, then the mass loss occurs primarily via Roche-lobe overflow, with a rate typically orders of magnitude higher than the wind mass-loss rates. Given that most stars have a very steep density profile in their photosphere, the discontinuity in mass-loss rate occurring when a star fills its Roche lobe is a good description of the actual situation. However, giant stars, particularly AGB objects, are “fluffy”¹, i.e., their density gradient is so shallow in the outer parts of the envelope that it makes it very difficult to define a stellar surface or edge. This implies that for AGB stars in binary systems a smooth transition must exist between single-star wind mass-loss and mass-loss by Roche-lobe overflow, depending on the proximity of the components. A description of mass loss that accounts for this smooth transition would provide an enhanced AGB mass-loss rate, as compared to the single-star mass-loss rate, therefore modifying the evolution of the binary system, especially if mass loss and mass transfer vary along the orbit.

Our understanding of how mass transfer processes occur in binary systems containing AGB stars can be improved via direct observations of systems known to contain a star which is the descendant of an AGB star, such as those composed of a white dwarf and a main sequence or a red giant star, we can obtain valuable information on how the binary interaction took place at the time when the primary was an AGB star. The study of the orbital properties of these systems and of the chemical abundances of the secondary, provides us the evolutionary endpoints that models of mass transfer, mass loss and nucleosynthesis in AGB stars must reproduce.

1.4 Systems with their primary beyond the AGB phase

We will now consider binary systems consisting of a white dwarf and a companion which is a main-sequence star or a red giant. The orbital properties and the heavy element abundances in these systems have not changed after the primary finished its AGB phase and became a white dwarf. Hence, their properties can be used to constrain how mass loss and accretion has occurred during the AGB phase.

A puzzling situation arises when studying the distribution of the eccentricities of these systems in terms of their orbital periods or separations. According to the current binary evolution picture, systems in which the AGB star is close to filling its Roche-lobe experience strong dissipation of energy due to the tidal interaction. This leads to the circularisation of the orbit on timescales shorter than the AGB lifetime, implying that all systems with a periastron distance of about 4 AU or smaller (i.e., periods of about 10 years or shorter) should be circularised.

¹Expression employed recurrently by Dr. O. R. Pols to characterise AGB stars and which describes them particularly well.

However, several observed binary systems with a primary beyond the AGB phase and with a shorter period show a significant eccentricity.

An important case is the Sirius system, whose orbital properties and the mass of its components are well known due to its proximity to the Solar System. This system contains a $1.05 M_{\odot}$ white dwarf as primary star and a $2.1 M_{\odot}$ main-sequence star as secondary component. The orbital period is of 50 years, however, due to its high eccentricity ($e = 0.59$), the distance between its components at the periastron passage is of 8.1 AU, meaning that the primary was very close to fill its Roche lobe by the time it was an AGB star or may have actually filled it. Hence, this system must have experienced such a strong tidal dissipation that it is expected to be completely circularised at the time when the primary becomes a white dwarf (see Chapter 4). In fact, models of binary evolution of possible progenitors of Sirius, assuming only tidal dissipation due to convective damping, show that only those systems that have periods longer than about 180 years are able to remain as eccentric as Sirius.

Another puzzling case is that of barium stars, of which there are a significant number. Barium stars are G- or K-type giants which show abundances of *s*-process elements, most prominently barium, that are abnormally high for their evolutionary stage. These stars are found in binary systems with white dwarf companions, which constitutes evidence for mass accretion from their companions when the latter were asymptotic giant branch (AGB) stars. Barium star binary systems are observed to have periods between 80 and 10000 days and most of the systems having periods larger than about 600 days are significantly eccentric (Jorissen et al. 1998). This is in contradiction with calculations of binary evolution models including only tidal circularisation. These models predict that only systems with periods larger than about 3500-4000 days remain eccentric after the primary goes through the AGB phase (Pols et al. 2003). Moreover, systems with periods shorter than about 1000 days should have gone through an unstable Roche-lobe overflow mass transfer phase and a subsequent common envelope phase, which also circularises the orbit. The fact that observed systems with such short period are still eccentric suggests that they should have been significantly eccentric at the time when Roche-lobe overflow mass transfer commenced. The tidal circularisation timescales of such systems are of the order of several hundreds of years, thus they can remain eccentric only if there exists an eccentricity-enhancing mechanism capable of counteracting the circularisation effect of the tidal dissipation.

The eccentricity–period distribution is not the only riddle in barium-star systems: also the distribution of their *s*-process abundances as a function of the period is unexplained satisfactorily. The highest observed *s*-process enhancements in barium stars, of up to about 20 times higher than solar, are seen in systems with periods ranging between 300 to 5000 days. Binary evolution models that account for these enhancements also predict a large number of *s*-enhanced systems with periods longer than 10000, which are not observed. This is further indication that our current understanding of mass transfer and mass loss in binary systems containing an AGB star is incomplete.

The problems that arise from modelling binary evolution of systems including an AGB star appear to have their roots in the over-simplified assumption of constant mass loss along

eccentric orbits, which is a direct consequence of incorrectly assuming that AGB stars have a well defined radius and that they will behave like single stars as long as they keep inside their Roche lobe. This assumption, of course, affects predictions of the amount of mass accreted by the companion.

1.5 Contribution from this thesis

This thesis is divided in two parts: the first part is focused on the evolution of AGB stars as single objects and the second part is focused on the evolution of AGB stars as components of binary systems. Most of the work has been carried out by employing a rapid synthetic stellar evolution code. Detailed evolutionary codes solve the stellar structure differential equations for different mesh points in a star. A rapid synthetic code, instead, computes stellar models using fitting formulae based on the detailed models to calculate relevant stellar quantities, such as core mass, luminosity, radius, etc., given an initial stellar mass and metallicity. This makes the calculations of the stellar evolution, which in the detailed models take from several tens of minutes to hours, to take at most several tenths of a second. This allows us to compare observations against synthesised populations of stars, providing a powerful tool to understand stellar evolution from a statistical point of view. A stellar population synthesis run follows the evolution of systems in a grid of initial conditions, weighing their contribution according to their probability of being observed. In this way we test not only if the models reproduce the observed data individually, but also if a system is likely to be observed or not. Uncertain physical mechanisms are described in our rapid models by using free parameters, which allows us to alter these parameters in such a way that the population synthesis results adjust the best to the observed distributions. This enables us to better constrain uncertain processes in AGB stars and in binary systems.

1.5.1 Constraining unknowns in AGB evolution and nucleosynthesis

In Chapter 2 we study the evolution and nucleosynthesis of *s*-process enhanced *intrinsic* stars. These are TP-AGB stars that have self-enriched their envelopes of *s*-process elements synthesised in their interiors via TDU. The relative abundances of *s*-process elements give information about the amount of ^{13}C that effectively acts as a source of neutrons for the *s*-process. We call this effective ^{13}C abundance “ $^{13}\text{C}_{\text{eff}}$ ” and normalise it so that $^{13}\text{C}_{\text{eff}} = 1$ corresponds to the standard case defined by Gallino et al. (1998). We compare our predicted $[\text{hs}/\text{ls}]^2$, where hs and ls represent abundances of *s*-process elements belonging to the Ba and Sr peak, respectively, to the observed $[\text{hs}/\text{ls}]$ of different sets of Galactic-disk and Galactic-halo *intrinsic* stars. The observations in the metallicity range $[\text{Fe}/\text{H}] \gtrsim -1$ are well fitted by $2/3 \lesssim ^{13}\text{C}_{\text{eff}} \lesssim 4/3$, a factor of 10 range smaller than that required by previous studies based on individual stellar models. The spread in $[\text{hs}/\text{ls}]$ required to match the observations arises in our stellar popula-

²We employ the usual notation $[X/Y] = \log_{10} \left[\frac{(X/Y)_{\text{observed}}}{(X/Y)_{\text{solar}}} \right]$.

tion models from following the evolution the AGB stars for a detailed grid of initial masses at each metallicity, instead of comparing a “typical” pulse for a “typical” star, as it was done in previous works (see, e.g., Busso et al. 2001). We also study statistically the properties of post-AGB stars, which allows us to constrain the minimum value for the asymptotic efficiency on the third dredge up (λ_{\min}) to ≈ 0.2 , and the mass of the ^{13}C pocket to $\approx 1/40$ of the mass of the intershell. Moreover, we also find that the minimum core-mass for third dredge-up to occur is about $0.065 M_{\odot}$ smaller than what the detailed models of Karakas et al. (2002) predict. This implies that third dredge-up takes place in stars with lower initial mass masses.

We also compare our predicted [Pb/hs] to observational data of “lead” stars. Lead stars are low-metallicity *extrinsic* objects, i.e., they became polluted by an AGB companion in a binary system. This class of observations indicates that at $[\text{Fe}/\text{H}] \lesssim -1$ a somewhat lower value $^{13}\text{C}_{\text{eff}} \approx 1/3$, perhaps down to $\approx 1/12$, is needed.

In Chapter 3 we apply the same approach as in Chapter 2, but this time we compare our model predictions to the chemical abundances of the object MACHO 47.2496.8, gathered by Reyniers et al. (2007). This is a post-AGB star in the Large Magellanic Cloud, most likely intrinsically polluted of *s*-process elements and with metallicity $[\text{Fe}/\text{H}] = -1.4$. It is the lowest-metallicity *s*-process enhanced intrinsic object ever found. We find that the chemical properties of MACHO 47.2496.8 are reproduced with the same values of λ_{\min} , size of the ^{13}C pocket and minimum core-mass for third dredge-up that we found in Chapter 2 to reproduce observational properties of Galactic post-AGB stars. The trend of objects with $[\text{Fe}/\text{H}] \lesssim -1$ being reproduced with a lower value of $^{13}\text{C}_{\text{eff}}$ than objects with Galactic-disk metallicity is also confirmed in this second study as the *s*-process element distribution of MACHO 47.2496.8 is well reproduced by assuming $1/6 < ^{13}\text{C}_{\text{eff}} < 1/3$. The fact that models with the same choice of parameters properly fit objects in different galaxies gives us confidence that the constraints we find have a universal character, which the detailed models will have to address in the future.

1.5.2 Orbital eccentricities of systems with a former AGB star

The second part of this thesis begins from Chapter 4, where the evolution of the orbital parameters due to AGB wind mass loss and mass transfer is revised. Most of the previous analysis had been done without considering conservation of angular momentum (e.g., Boffin & Jorissen 1988). We revisit the problem by treating it in a non-rotating reference frame with its origin in the centre of mass of the binary system, without reducing it into a one body problem. This makes the variational equations more complicated, however, it makes it easier to keep a clear and consistent analysis. At the same time we state the variational equations in such a way that we can follow the evolution of the system even if parameters are not constant along the orbit. This is useful when treating systems with AGB components given that their mass loss rates may change depending on the distance to the companion, which, in the case of eccentric orbits, varies depending on the orbital phase angle. Given that AGB envelopes are “fluffy” we propose a smooth transition between the single-star wind mass-loss regime and the Roche-lobe overflow mass-loss regime, which scales with the sixth power of the ratio of the AGB-star radius to its Roche-lobe radius. Due to the enhanced mass-loss during peri-

astron passages, the eccentricity of the system is enhanced in a significantly short timescale, providing a mechanism which can compete with the strong circularisation that relatively close binary systems experience due to the tidal interaction. We trace the binary evolution of Sirius-like systems, i.e., with a white dwarf and a main-sequence companion with similar masses as Sirius A and Sirius B, respectively. We show that using binary evolution models where only tidal dissipation is considered, synthetic Sirius-like systems with the orbital properties of Sirius cannot be produced if reasonable values of tidal dissipation strength are assumed. Subsequently, we show that including in our models the prescription of eccentricity-enhancement due to variable mass loss described above, we produce synthetic systems with similar orbital properties as Sirius by reducing the tidal dissipation strength within a reasonable range.

In Chapter 4 we show that the eccentricity-pumping mechanism we propose provides a possible explanation for the problem of eccentric barium star systems. We estimate the effect of this mechanism as applied at the moment of evolution when the AGB star has its largest radius, i.e., when tidal dissipation is strongest, and conclude that under the usually assumed values of tidal strength it is still not possible to explain systems with periods shorter than about 3000 days. However, we show that with a reasonably weaker tidal dissipation strength we can explain eccentric systems with periods as short as about 1100 days. This is only an estimate and binary population synthesis runs have to be carried out in order to obtain conclusive results. This is performed in Chapter 5.

1.5.3 Population synthesis of barium stars with AGB mass-loss and eccentricity enhancement

In Chapter 5 we carry out stellar population synthesis with our rapid synthetic code, including the prescription for mass-loss and eccentricity enhancement. This prescription allows us to obtain a better match to observed properties of barium-star systems, in particular if we reduce the tidal strength in a factor of 4. This somewhat weaker tidal dissipation may also allow systems to enter a common envelope phase while still eccentric. Our description of common envelope evolution prevents binaries filling their Roche lobes to remain eccentric, so we still cannot explain those observed eccentric systems which have a periods shorter than about 1000 days. A remaining problem is that we always find a too high number of systems with periods larger than 10000 days, as compared to the observations, which may indicate that the accretion at long periods is less efficient than assumed. This issue will have to be addressed in the future.

Part I

Nucleosynthesis in AGB stars

Chapter 2

The *s*-process in stellar population synthesis: a new approach to understanding AGB stars

A.A. Bonačić Marinović, R.G. Izzard, M. Lugaro, O.R. Pols,
Astronomy & Astrophysics, v. 469, p. 1013-1025 (2007)

Abstract Thermally pulsating asymptotic giant branch (AGB) stars are the main producers of slow neutron capture (*s*-) process elements, but there are still large uncertainties associated with the formation of the main neutron source, ^{13}C , and with the physics of these stars in general. Observations of *s*-process element enhancements in stars can be used as constraints on theoretical models. For the first time we have applied stellar population synthesis to the problem of *s*-process nucleosynthesis in AGB stars, in order to derive constraints on free parameters describing the physics behind the third dredge-up and the properties of the neutron source. We utilise a rapid evolution and nucleosynthesis code to synthesise different populations of *s*-enhanced stars, and compare them to their observational counterparts to find out which values of the free parameters in the code produce synthetic populations that fit the observed populations best. These free parameters are the amount of third dredge-up, the minimum core mass for third dredge-up, the effectiveness of ^{13}C as a source of neutrons, and the size in mass of the ^{13}C pocket. We find that galactic disk objects are reproduced by a spread of a factor of two in the effectiveness of the ^{13}C neutron source. Lower metallicity objects can be reproduced only by lowering the average value of the effectiveness of the ^{13}C neutron source needed for the galactic disk objects by at least a factor of 3. Using observations of *s*-process elements in post-AGB stars as constraints we find that dredge-up has to start at a lower core mass than predicted by current theoretical models, that it has to be substantial ($\lambda \gtrsim 0.2$) in stars with mass $M \lesssim 1.5 M_{\odot}$, and that the mass of the ^{13}C pocket must be about 1/40 that of the intershell region.

2.1 Introduction

About half of elements that are heavier than iron are produced by slow neutron captures (*s*-process) in the deep layers of thermally pulsating (TP-) asymptotic giant branch (AGB) stars, which represent the late evolutionary phase of objects with an initial mass of $M \lesssim 8 M_{\odot}$. These stars have degenerate carbon-oxygen cores surrounded by two burning shells, and they undergo a cyclic instability of the helium-burning shell known as thermal pulses. The *s*-process elements are believed to be synthesised in the thin helium-rich layer between the helium-burning and hydrogen-burning shells known as the inter-shell region, or *intershell*. After each thermal pulse the hydrogen-rich convective envelope may penetrate into the intershell and bring the synthesised heavy elements, together with the products of helium burning (mainly carbon), to the stellar surface in a phenomenon called *third dredge-up* (TDU). Strong stellar winds gradually ablate the envelope and enrich the interstellar medium with the nucleosynthesis products. Many of the physical processes taking place in TP-AGB stars are still highly uncertain, such as how the main source of free neutrons required for the *s*-process is produced (see below), under which conditions TDU occurs and how efficient it is, and the what strength and driving mechanism of mass loss is. Many of these uncertainties are related to our poor understanding of mixing processes in stars. For a recent review of AGB stars see Herwig (2005), and for a discussion of uncertainties in AGB stellar models see, e.g., Lugaro et al. (2003).

The synthesis of *s*-process elements requires a source of free neutrons that can be captured by iron seeds to build up heavier nuclei along the isotopic stability valley. During the period of quiescent hydrogen-shell burning in between thermal pulses, the inter-pulse period, the conditions in the intershell (temperature, density and helium abundance) favour the $^{13}\text{C}(\alpha, n)^{16}\text{O}$ reaction. For this reaction to be an effective source of free neutrons, a ^{13}C -rich region or *pocket* in the intershell is needed. The production of ^{13}C takes place by means of the $^{12}\text{C}(p, \gamma)^{13}\text{N}(\beta^+ \nu)^{13}\text{C}$ reaction. It is assumed that the protons needed for this reaction penetrate the top of the intershell after TDU has occurred, as a result of a mixing process of an as yet uncertain nature: semi-convection (Hollowell & Iben 1988), hydrodynamical overshooting (Herwig et al. 1997), rotation (Langer et al. 1999; Herwig et al. 2003), and gravity waves (Denissenkov & Tout 2003) have all been proposed. As a consequence large uncertainties exist in the mass size of the ^{13}C pocket and the ^{13}C abundance profile inside it. In addition, due to the existence of several neutron poisons, especially ^{14}N , not all free neutrons released by the $^{13}\text{C}(\alpha, n)^{16}\text{O}$ reaction participate in the *s*-process, so the effectiveness of ^{13}C as a neutron source for the *s*-process is also very uncertain. Another neutron burst is also released in the convective intershell during the thermal pulses due to the $^{22}\text{Ne}(\alpha, n)^{25}\text{Mg}$ reaction, but the activation of this reaction is only marginal, which makes its contribution to the neutron exposure smaller than that of the $^{13}\text{C}(\alpha, n)^{16}\text{O}$ reaction (see Busso et al. 1999 for a review of *s*-process nucleosynthesis in AGB stars).

Among stars that are enhanced in *s*-process elements (*s*-enhanced stars), one distinguishes intrinsic and extrinsic objects. Intrinsic *s*-enhanced stars are typically late-type giants of spectral classes S and C that show over-abundances of *s*-process elements (see, e.g., Smith & Lambert 1990; Abia et al. 2002), including the radioactive element Tc (Merrill 1952). With

a half-life of a few million years, the presence of Tc lines indicates that the synthesis of *s*-process elements happened recently and in situ. Therefore intrinsic *s*-enhanced stars must be objects in the TP-AGB phase or post-AGB phase, which have recently experienced thermal pulses and TDU. The study of elemental abundances in these stars gives clues to the uncertain physical phenomena that take place in their interiors. Extrinsic *s*-enhanced stars also show over-abundances of *s*-process elements, but no Tc lines are present (Jorissen et al. 1993). This indicates that Tc has decayed since the *s*-process elements were synthesised. In addition, extrinsic stars are often observed to be in an evolution phase earlier than the TP-AGB; i.e., they are (sub)giants or main sequence stars. This implies that the *s*-process elements were not produced in situ, but that they have been accreted from a more massive TP-AGB companion star. These stars can therefore act as probes for studying mass transfer processes in binaries and for tracing the nucleosynthesis that occurred in their companion stars.

Busso et al. (2001) carried out a detailed comparison between observations of *s*-process enhanced stars and model predictions for the *s*-process in single AGB stars of different metallicities. They found that a large spread (a factor of ~ 20) in the effectiveness (see §2.2.3 for a definition of this parameter) of the main neutron source ^{13}C was needed to match spectroscopic observations at a given metallicity. Their analysis is based on a small set of initial stellar masses, and they have taken only the final abundances of their stars into consideration. In this paper we improve on their analysis by comparing observations of different types of stars belonging to the AGB family to stellar population synthesis models computed with the inclusion of the *s*-process. Our use of a rapid synthetic evolution code allows us to study a large set of finely spaced initial masses and metallicities and to trace the complete AGB evolution of each star. Using this method we are able to put much tighter constraints on the effectiveness of ^{13}C as a neutron source. In addition, by comparing our models to post-AGB observations, we also put constraints on the minimum core mass for TDU, the TDU efficiency, and the size of the ^{13}C pocket.

The AGB stellar models and the associated free parameters are described in §2.2. Our stellar population synthesis method is described in §2.3 and the results are presented in §2.4. In §2.5 we discuss our results and draw our conclusions.

2.2 The AGB models

Our TP-AGB star models are calculated with a modified version of the rapid evolutionary code by Hurley et al. (2000) and Izzard et al. (2004). We limit ourselves to a brief overview of the ingredients of this code and a discussion of the most important free parameters. A detailed description of our modifications and improvements can be found in Appendix A. Stellar evolution and nucleosynthesis are modelled synthetically, i.e., by means of analytical fits to the detailed evolutionary models of Karakas et al. (2002) and Stancliffe et al. (2004), and in some cases by tabular interpolation of these detailed models. Fits and interpolations depend on global stellar parameters, such as metallicity, mass, and core mass. This synthetic approach makes the calculation of the evolution very fast. The *s*-process element nucleosynthesis is cal-

culated by interpolating results based on detailed models by Gallino et al. (1998), as described below. With these models we are able to follow the chemical abundances of stars as a function of time, from their initial abundances at the beginning of the main sequence, for which we use those of Anders & Grevesse (1989), to their chemically enhanced abundances of the latest evolutionary TP-AGB and post-AGB phases.

Many uncertainties exist in the detailed evolutionary models, which we treat as free parameters. In the following subsections we discuss the free parameters that are most relevant for stellar chemical evolution.

2.2.1 Minimum core mass for third dredge-up

Detailed models of TP-AGB stellar evolution which find TDU show that it only occurs when the stellar core mass is greater than about $0.6 M_{\odot}$ (e.g., Boothroyd & Sackmann 1988; Lattanzio 1989; Straniero et al. 1997), but there is disagreement of about 10% on the exact value of this minimum core mass (see, e.g., Lugaro et al. 2003). The luminosity and surface abundances of carbon and *s*-process elements in TP-AGB stars of mass $M \lesssim 2 M_{\odot}$ depend strongly on this minimum core mass. We have modelled the TDU by using the fit to the models of Karakas et al. (2002) from Izzard et al. (2004), which includes the free parameter $\Delta M_{\text{c}}^{\text{min}}$. This parameter offsets the minimum core mass by a fixed amount compared to the results of Karakas et al. (2002), allowing stars of low mass to undergo TDU, even if they do not do so in the detailed models.

2.2.2 Third dredge-up efficiency

Detailed evolution models disagree on the amount of third dredge-up that occurs in a star of a particular mass and metallicity, i.e., how deep the convective envelope penetrates the intershell (see, e.g., Frost & Lattanzio 1996 and Mowlavi 1999 for discussion). The amount of dredge-up can be measured by the *third dredge-up efficiency*

$$\lambda = \frac{\Delta M_{\text{TDU}}}{\Delta M_{\text{H}}}, \quad (2.1)$$

where ΔM_{TDU} is the reduction in mass of the hydrogen exhausted core as a result of dredge-up and ΔM_{H} is the amount of mass by which the hydrogen-exhausted core increased due to hydrogen burning during the previous inter-pulse period. Thus, if $\lambda = 0$ there is no dredge-up at all, while if $\lambda = 1$ there is no net growth of the hydrogen-exhausted core. We apply the parametrisation from Izzard et al. (2004) in which λ grows asymptotically with pulse number to a maximum value of

$$\lambda_{\text{max}} = \max(\lambda_{\text{min}}, \lambda_{\text{max}}^{\text{fit}}). \quad (2.2)$$

Here $\lambda_{\text{max}}^{\text{fit}}$ is a function of mass and metallicity, which fits the λ_{max} value of the detailed models (Karakas et al. 2002), and the free parameter λ_{min} is used to set a lower limit. In this way stars

that show negligible TDU efficiency in the detailed models are allowed to have a substantial TDU efficiency when λ_{\min} is set to be greater than zero.

2.2.3 Effectiveness of ^{13}C as a neutron source

At the end of a TDU episode protons from the bottom of the H-rich envelope may penetrate beyond the chemical boundary into the helium- and carbon-rich intershell. They react with ^{12}C to produce ^{13}N , which decays into ^{13}C forming the ^{13}C pocket. If there are enough protons, ^{13}C will also capture protons and produce ^{14}N . The ^{13}C in the pocket is a source of neutrons by means of the $^{13}\text{C}(\alpha, n)^{16}\text{O}$ reaction, but it has to compete with ^{14}N as a sink of free neutrons due to the $^{14}\text{N}(n, p)^{14}\text{C}$ reaction, which has a relatively high neutron capture cross section. As a result of this competition an *effective local ^{13}C abundance* can be defined, which parameterises the number of free neutrons per heavy seed nucleus in the intershell available for the *s*-process to take place. The abundance ratios of *s*-process elements in the ^{13}C pocket are determined by this local ^{13}C abundance, which is scaled relative to a standard case. This standard case was defined by Gallino et al. (1998) and Busso et al. (2001), based on the ^{13}C pocket found by Hollowell & Iben (1988) in their detailed evolutionary calculations. Gallino et al. (1998) show that, with this pocket, low-mass AGB stars of half solar metallicity produce the main *s*-process component for the Sun. We denote this scaled effective ^{13}C abundance as $^{13}\text{C}_{\text{eff}}$, so that the standard case corresponds to $^{13}\text{C}_{\text{eff}} = 1$.

Comparing the absolute elemental abundances produced by *s*-process models directly to observations is difficult because they depend on the dilution of material from the intershell into the envelope, which in turn depends on several uncertain factors such as the size in mass of the ^{13}C pocket, the amount of TDU, mass loss, and mass accretion. However, the *s*-process element abundance ratios mostly remain unaffected by these processes, so they provide direct constraints on $^{13}\text{C}_{\text{eff}}$ (see §2.4).

2.2.4 Size of the ^{13}C pocket

In order to calculate the abundances in the stellar envelope we must know the element mass fraction in the intershell at the moment when the star undergoes TDU. For *s*-process elements, we calculate these intershell abundances by using the results of detailed models from Gallino et al. (1998), which consist of a grid of intershell elemental abundances at the time of TDU for stellar masses of 1.5, 3, and 5 M_{\odot} , metallicities $10^{-4} \leq Z \leq 0.02$, effective local ^{13}C abundance ($1/24 \leq ^{13}\text{C}_{\text{eff}} \leq 2$) and number of thermal pulse followed by TDU ($2 \leq N_{\text{TDU}} \leq 29$). We know the mass of the ^{13}C pocket and of the intershell in these detailed models, which we use to trace back the local element mass fractions in the ^{13}C pocket just before the thermal pulse occurs. We map a grid of *s*-process element mass fractions in the ^{13}C pocket for different stellar masses, metallicities, $^{13}\text{C}_{\text{eff}}$, and pulse number, which is independent of the choice of the size of the ^{13}C pocket and that of the intershell. We interpolate linearly on this grid and if the stellar mass and/or pulse number needed for the calculation is out of the grid bounds we

use the result of the closest point on the grid.

Note that with this procedure we do not properly account for the ^{22}Ne neutron source. However, this neutron source does not contribute to defining the overall *s*-process distribution, at least for stellar models of mass $M \lesssim 4 M_{\odot}$, which are believed to be the counterparts of the observed *s*-process enhanced stars that we will discuss in §2.4 (e.g., Abia et al. 2001).

We assume that the ^{13}C pocket mass is a fixed fraction, $f_{^{13}\text{C,IS}}$, of the mass of the intershell at the moment just before TDU occurs, M_{IS} , which in turn is approximated well by the maximum mass of the convective intershell pocket during the thermal pulse. We employ the relation proposed by Iben (1977) for the maximum convective intershell mass,

$$\log_{10}(M_{\text{IS}}) = -1.835 + 1.73M_{\text{c}} - 2.67M_{\text{c}}^2, \quad (2.3)$$

where M_{c} is the mass of the H-exhausted core. This relation is derived for core masses higher than $0.95M_{\odot}$, but when extrapolated to lower core masses, it yields intershell mass values similar to those considered by Gallino et al. (1998) in their detailed models. The value of $f_{^{13}\text{C,IS}}$ can be constrained by observations of surface abundances of *s*-process elements, although these abundances also depend on the amount of dredge-up that the star has experienced. This degeneracy is broken by studying the abundances of other elements that are not synthesised via the *s*-process, as discussed in §2.4.1.

2.2.5 Mass loss

Mass loss is an uncertain factor in AGB evolution which affects the enhancement of *s*-process elements on the surface of a TP-AGB star (Straniero et al. 2003). The mass loss rate determines the stellar lifetime as a TP-AGB star by truncating it when the envelope is lost. In the models of Gallino et al. (1998) the intershell *s*-process abundance ratios vary from one pulse to another, until after roughly 20 pulses they reach an asymptotic value. The asymptotic values are usually considered to be the *s*-element ratios of a typical pulse and are often compared to the observed ratios (e.g., Busso et al. 2001; Straniero et al. 2003; Reyniers et al. 2004). Depending on the mass loss rate applied in the models, a star with mass $M \lesssim 1.5M_{\odot}$ can undergo from very few thermal pulses (or none) to several tens, which affects its surface composition and yield during the TP-AGB phase. In this work we use the mass-loss prescription by Vassiliadis & Wood (1993):

$$\log_{10} \frac{\dot{M}_{\text{AGB}}}{M_{\odot} \text{ yr}^{-1}} = -11.4 + 0.025 \left[\frac{P}{\text{day}} - 100 \max \left(\frac{M - 2.5M_{\odot}}{M_{\odot}}, 0 \right) \right], \quad (2.4)$$

where $\log P/\text{day} = -2.07 + 1.94 \log R/R_{\odot} - 0.9 \log M/M_{\odot}$ is the logarithm of the Mira pulsation period. We do not attempt to vary the AGB mass-loss rate, but we discuss the consequences of this assumption on our results in §2.5.

The mass-loss rate during the giant branch phase affects the envelope mass at the moment when a star begins its TP-AGB phase. We have modelled mass-loss from giant branch stars with the widely used prescription by Reimers (1975),

$$\dot{M}_{\text{GB}} = 4 \times 10^{-13} \eta_{\text{GB}} (L/L_{\odot}) (R/R_{\odot}) (M/M_{\odot})^{-1} M_{\odot} \text{ yr}^{-1}, \quad (2.5)$$

with $\eta_{\text{GB}} = 0.3$, which is within the limits set by the morphology of horizontal branch stars in the galactic globular clusters (Iben & Renzini 1983; Carraro et al. 1996).

2.3 Population synthesis

We make use of our synthetic evolutionary models to carry out population synthesis of single stars, on a grid of 50 logarithmically spaced metallicities ranging between $10^{-4} \leq Z \leq 0.025$ and 500 logarithmically spaced initial masses, whose range depends on the metallicity and on whether we are modelling a population of intrinsic or extrinsic *s*-enhanced stars.

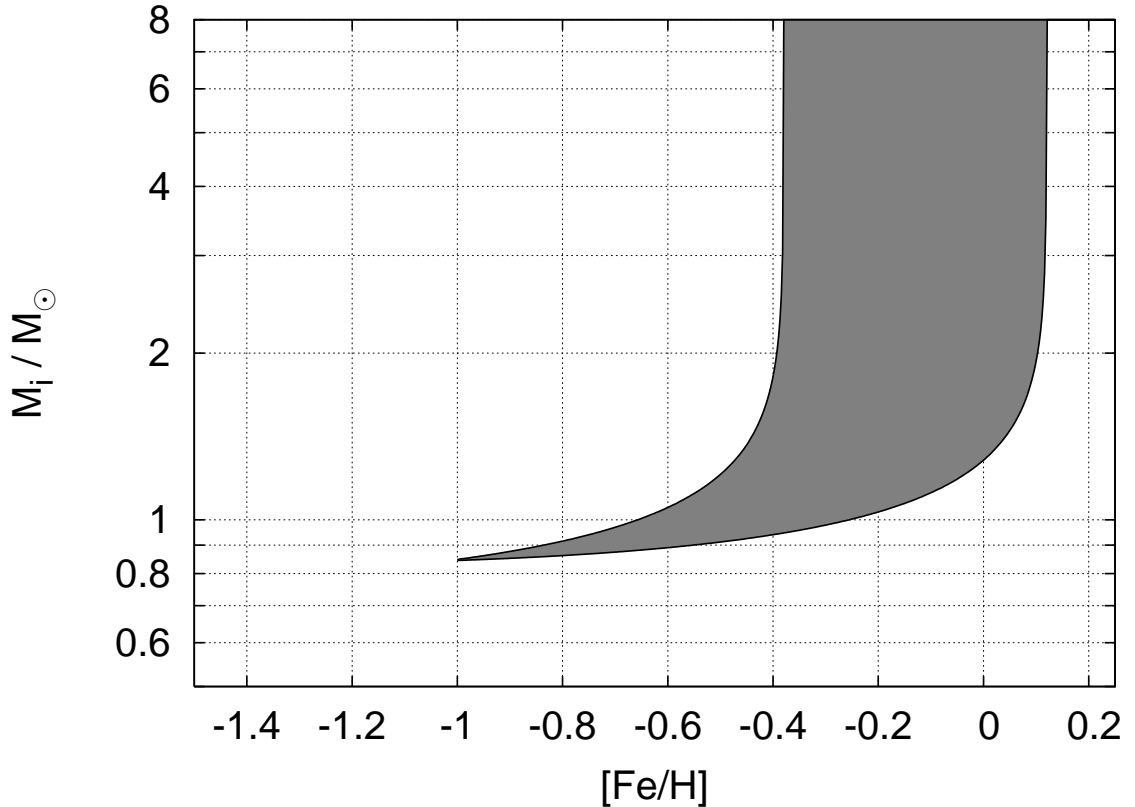


Figure 2.1: Range of initial masses, M_i , of our population synthesis grid as a function of metallicity, depicted by the shaded area. For a given metallicity this shows the initial-mass range of stars which can be observed in the TP-AGB phase, with a maximum mass of $8 M_{\odot}$.

In the case of intrinsic stars, for each metallicity we apply the initial mass ranges shown in Fig. 2.1, with $8 M_{\odot}$ as a maximum. We derive these ranges from combining our stellar

evolution models with the age–metallicity relation (AMR) for the galactic disk of Pont & Eyer (2004)

$$\left[\frac{\text{Fe}}{\text{H}} \right] = \log_{10} \left(\frac{t - 17.82}{-23.24} \right) \pm 0.25 \text{ dex}, \quad (2.6)$$

where the notation for the element number density ratio $\left[\frac{X}{Y} \right] = \log_{10} \left(\frac{n_X}{n_Y} / \frac{n_{X\odot}}{n_{Y\odot}} \right)$ is used and t is the age in Gyr, with the age of the Universe (13.7 Gyr) as its upper limit. Then, from our single-star models we consider the range of initial masses for which a star spends at least some of its TP-AGB life within the age range allowed by the AMR. The probability for an intrinsic star to have a given abundance is weighted by the time it spends showing this abundance and by its contribution according to the initial mass function (IMF). We use the IMF, ξ , of Kroupa et al. (1993), given by

$$\xi(M_i) = \begin{cases} 0.035 M_i^{-1.3} & \text{if } 0.08 < M_i < 0.5, \\ 0.019 M_i^{-2.2} & \text{if } 0.5 < M_i < 1.0, \\ 0.019 M_i^{-2.7} & \text{if } 1.0 < M_i, \end{cases} \quad (2.7)$$

where M_i is the initial stellar mass in solar units.

Given that we employ single stellar models, we treat the case of extrinsic stars indirectly. These stars have acquired their *s*-process enhancements by accreting part of the mass ejected by an initially more massive binary companion. Therefore we assume a simple model in which the initial mass of the companion is assumed to be distributed according to the single-star IMF. Hence the probability of an extrinsic star to show a given elemental abundance is weighted by the amount of mass which is lost by its companion in the form of that element and by the IMF weight of this companion. Because mass transfer could have occurred at any time since the formation of the system, we consider all stars whose evolution is beyond the TP-AGB phase, which in each metallicity bin corresponds to initial masses greater than the lower limit in Fig. 2.1 and smaller than $8 M_{\odot}$. For the models with $[\text{Fe}/\text{H}] < -1$ we consider $0.8 M_{\odot}$ to be the lower initial mass limit.

2.4 Results

In this section we present the results of our population synthesis models and compare them to different sets of observational data. The observations provide measurements of the surface abundances of *s*-process elements relative to that of iron. Following the convention, we calculate for each star in our grid its *heavy s*-process (hs) element abundance ratio,

$$\left[\frac{\text{hs}}{\text{Fe}} \right] = \frac{1}{5} \left(\left[\frac{\text{Ba}}{\text{Fe}} \right] + \left[\frac{\text{La}}{\text{Fe}} \right] + \left[\frac{\text{Ce}}{\text{Fe}} \right] + \left[\frac{\text{Nd}}{\text{Fe}} \right] + \left[\frac{\text{Sm}}{\text{Fe}} \right] \right), \quad (2.8)$$

and *light s*-process (ls) element abundance ratio,

$$\left[\frac{\text{ls}}{\text{Fe}} \right] = \frac{1}{2} \left(\left[\frac{\text{Y}}{\text{Fe}} \right] + \left[\frac{\text{Zr}}{\text{Fe}} \right] \right). \quad (2.9)$$

These ratios are altered by dilution in the stellar envelope, which is affected by several uncertain factors such as the size in mass of the ^{13}C pocket, the amount of TDU, mass loss and, in the case of binaries, mass accretion. We also study the ratio of hs-elements to ls-elements,

$$\left[\frac{\text{hs}}{\text{ls}} \right] = \left[\frac{\text{hs}}{\text{Fe}} \right] - \left[\frac{\text{ls}}{\text{Fe}} \right]. \quad (2.10)$$

This ratio reaches the $[\text{hs}/\text{ls}]$ values of the intershell after a number of pulses asymptotically, making it mostly unaffected by dilution.

The asymptotic envelope ratio is therefore only determined by $^{13}\text{C}_{\text{eff}}$ (see §2.2.3), but not by other free parameters in our model, such as the size of the ^{13}C pocket ($f_{13\text{C,IS}}$). Figure 2.2 shows the envelope $[\text{hs}/\text{ls}]$ ratios obtained from the models of Busso et al. (2001), which in each model reach their corresponding intershell asymptotic value, but take a number of pulses to do so. Hence, considering stars that have experienced only a few TDU episodes, either because they are in an early stage of the TP-AGB phase or because they have masses of $M \lesssim 1.5 M_{\odot}$, results in a natural spread of $[\text{hs}/\text{ls}]$ values. Only in AGB stars with $M \gtrsim 5 M_{\odot}$ is the amount of dredged-up material is so small that the surface $[\text{hs}/\text{ls}]$ ratios differ from those of the intershell.

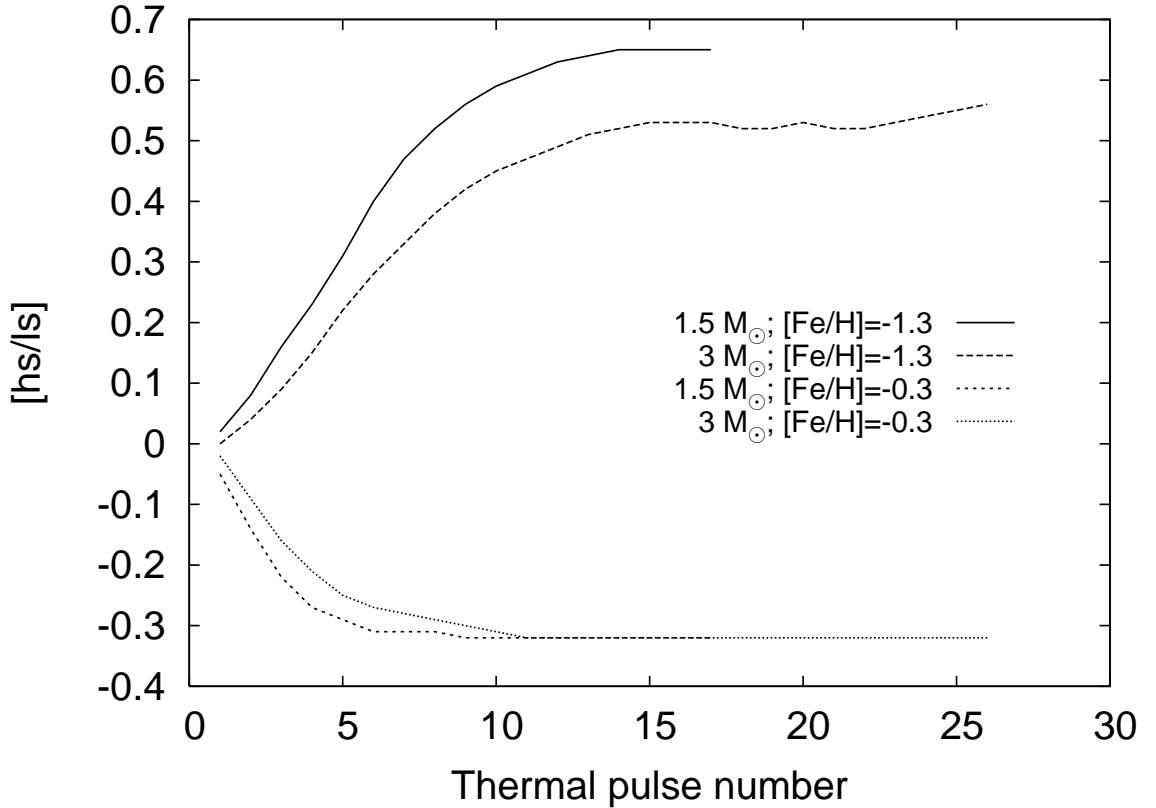


Figure 2.2: Envelope $[\text{hs}/\text{ls}]$ during the evolution of $1.5 M_{\odot}$ and $3 M_{\odot}$ star models of different metallicity, as indicated in the panel, and with $^{13}\text{C}_{\text{eff}}=1$.

To compare these abundance ratios with the observed data we have binned the resulting number distribution with a resolution of 0.1 dex. Whenever a star has a certain abundance ratio, its probability is added to the corresponding bin. This is done separately for the different metallicity bins and in each we normalise the resulting probability distribution by dividing it by its highest value.

We select those stars to be *s*-enhanced that have [ls/Fe] and/or [hs/Fe] larger than 0.1 dex. First we analyse the [hs/ls] ratios of intrinsic *s*-enhanced stars, which only have a strong dependence on the $^{13}\text{C}_{\text{eff}}$ value. In all the runs we use $\Delta M_{\text{c}}^{\text{min}} = -0.065M_{\odot}$, $\lambda_{\text{min}} = 0.2$, and $f_{^{13}\text{C,IS}} = 1/40$, based on our attempts to fit the post-AGB star observations of [Zr/Fe] ratios and carbon abundances, as explained in detail in §2.4.1. In §2.4.2 we study the [hs/ls] ratios, but this time of extrinsic *s*-enhanced stars, which give clues on $^{13}\text{C}_{\text{eff}}$ at metallicities lower than that of the galactic disk.

2.4.1 Intrinsic *s*-enhanced stars

[hs/ls] ratios of MS/S stars

The MS/S stars are late-type giants that show lines of ZrO and TiO, indicating that they are enhanced in *s*-element abundance, have low surface temperature, and their C/O ratio is lower than unity. To account for these stars we selected *s*-enhanced stars in the TP-AGB phase of evolution from our population synthesis with a surface effective temperature lower than 3500 K and $\text{C/O} < 1$ in their envelope. We compared our results for the [hs/ls] ratio to observational data of intrinsic MS/S stars gathered by Busso et al. (2001). In Fig. 2.3 our results only appear at $[\text{Fe}/\text{H}] \gtrsim -0.6$ because low-metallicity stars that undergo TDU episodes are too hot to be classified as MS/S objects. This is consistent with the observations. Increasing $^{13}\text{C}_{\text{eff}}$ in our models increases the [hs/ls] ratios on the low-metallicity side of the plot, but at high metallicities the [hs/ls] ratios are decreased. This is explained as follows. If the number of heavy iron seeds is decreased for a given number of available free neutrons, then the [ls/Fe] ratio increases due to *s*-process reactions and [hs/ls] decreases, as is observed at high metallicities in our results. But if [Fe/H] is decreased even more, the synthesis of ls-elements saturates and the hs-element abundance increases with respect to iron, raising both ratios [hs/Fe] and [hs/ls], as can be seen in our models at low metallicities (Travaglio et al. 1999; Busso et al. 2001). Thus $^{13}\text{C}_{\text{eff}}$ basically determines at which metallicity our models will show [hs/ls] ratios below solar and where they will rise to solar and beyond. This effect cannot be seen clearly in our MS/S star synthesis due to the lack of *s*-enhanced MS/S stars below $[\text{Fe}/\text{H}] \sim -0.6$, but is common to all the stellar populations that we have synthesised and is more evident in SC and C stars and post-AGB stars (§2.4.1 and §2.4.1, respectively). In contrast with other studies where only the asymptotic values of [hs/ls] are considered (e.g., Goriely & Mowlavi 2000; Busso et al. 2001), a natural spread in this ratio is observed in our results. This is explained by our tracing of the whole TP-AGB evolution, where the initial dozen pulses have different *s*-process ratios. Stars of mass $M \lesssim 1.5 M_{\odot}$, which are the most numerous due to the IMF and which do not undergo more than 10–20 pulses, contribute most to this effect. Fig. 2.3 shows

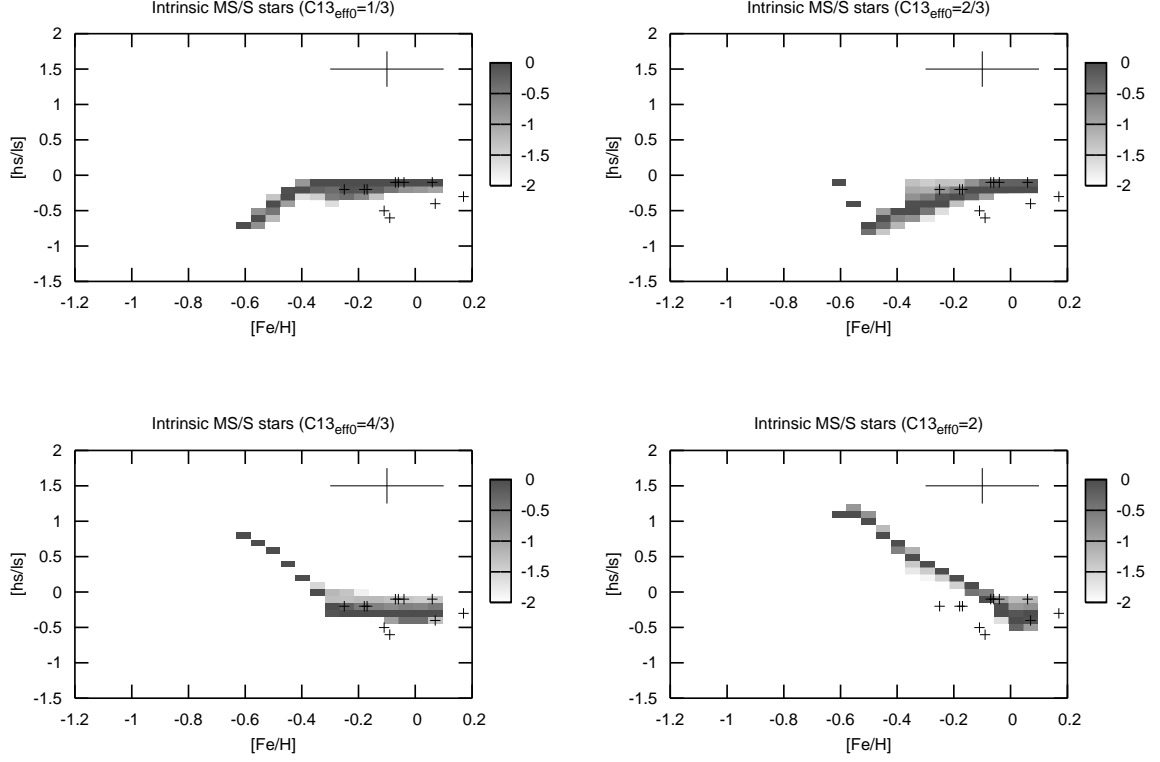


Figure 2.3: Intrinsic MS/S stellar population synthesis results compared to the observations. The panels show our results calculated with four increasing $^{13}\text{C}_{\text{eff}}$ values as indicated above the panels. The grey scale is a logarithmic measure of the normalised number distribution of stars over $[hs/l_s]$. The crosses are the observational data gathered by Busso et al. (2001), which have an average error given by the size of the cross in the upper right of each plot.

that the best fit to the observed distribution of MS/S stars is obtained with $^{13}\text{C}_{\text{eff}} \approx 4/3$ and a spread in $^{13}\text{C}_{\text{eff}}$ values is not needed to match all the observations. Given that the error bars on the individual observations are large (as indicated in Fig. 2.3), and that the observed $[hs/l_s]$ values are close to 0, the value of $^{13}\text{C}_{\text{eff}}$ is not strongly constrained by these observations. The (on average) negative values of $[hs/l_s]$ are matched, within observational errors, by the models if $^{13}\text{C}_{\text{eff}}$ is between $2/3$ and 2 . As the $[hs/l_s]$ ratio is not sensitive to dilution, changes in the other free parameters do not affect these results.

$[hs/l_s]$ ratios of SC and C stars

SC and C stars are late-type giants that show lines of carbide molecules in their spectrum, which indicates that there is more C than O by number. In the case of the SC stars, the C/O ratio is close to unity, given that they also show ZrO lines. To reproduce these stars we select from our population synthesis results those *s*-enhanced TP-AGB stars which have $C/O > 1$.

We compare our synthetic [hs/ls] ratios with the observational data gathered by Busso et al. (2001) and from Abia et al. (2002) as shown in Fig. 2.4. The spread in the [hs/ls] ratio is explained in the same way as for MS/S stars. The spread is smaller at low metallicities due to the small range of initial stellar masses considered at these metallicities resulting from the AMR (see Fig. 2.1). The effect of changing $^{13}\text{C}_{\text{eff}}$ on our synthetic [hs/ls] ratios is clearer

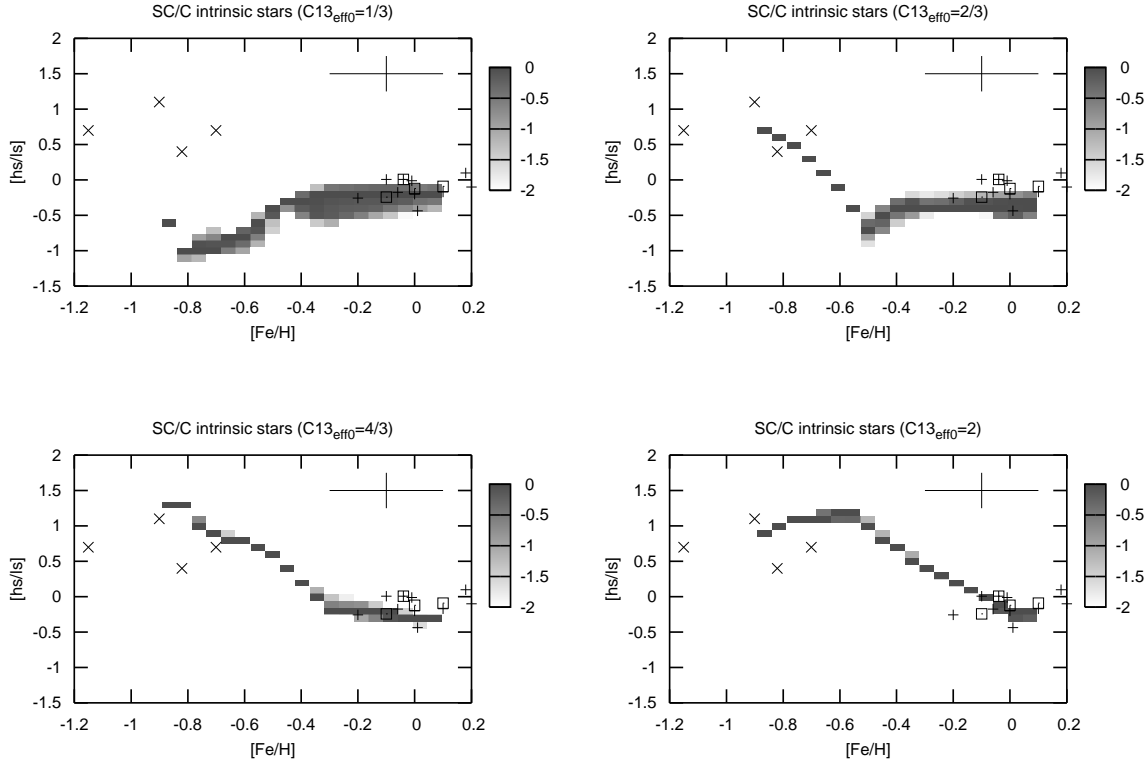


Figure 2.4: As Fig. 2.3, but for intrinsic SC and C stars. The horizontal crosses are observational data of intrinsic SC/C star gathered by Busso et al. (2001), complemented with data of Abia et al. (2002). The squares are SC/C stars in which the presence of Tc is doubtful (Abia et al. 2002) and the diagonal crosses are halo C stars from Busso et al. (2001). The observations have an average error given by the size of the cross in the upper right of each plot.

in this population of stars than in the MS/S stars, particularly for $[\text{Fe}/\text{H}] \lesssim -0.4$. As in the case of the MS/S stars, the other free parameters do not affect the [hs/ls] ratios. Most of the observed SC and C stars cluster around $[\text{Fe}/\text{H}] \approx 0$ and slightly negative values of [hs/ls]. These stars can be fitted with any value of $^{13}\text{C}_{\text{eff}}$. The diagonal crosses in Fig. 2.4 are halo C stars suspected to be intrinsic. They are not expected to follow the same AMR as those in the galactic disk, but the fact that they are old and of low mass is approximately modelled by our AMR. Three of these stars are matched by our models for values of $^{13}\text{C}_{\text{eff}} \gtrsim 2/3$, but a lower $^{13}\text{C}_{\text{eff}}$ cannot reproduce their [hs/ls]. The lack of stars below $[\text{Fe}/\text{H}] \sim -1$ in our models is due to the fact that, with our adopted AMR, lower metallicity stars do not become TP-AGB stars

within the age of the Universe. This effect is observed in all our results involving intrinsic stars and is consistent with the observations.

[hs/ls] ratios of post-AGB stars

Post-AGB stars are in the fast evolutionary phase between the AGB and white dwarf track. They suffer from strong mass loss and are hot, but not hot enough to ionise their circumstellar medium. We select them from our models by choosing those *s*-enhanced TP-AGB stars that have less than $0.03M_{\odot}$ left in their envelopes. We compare our synthetic population to the observational data gathered by Busso et al. (2001), van Winckel (2003), Reyniers et al. (2004), and Giridhar & Arellano Ferro (2005). Fig. 2.5 shows a spread, mostly at high metallicities, which is due to the different initial stellar masses taken into account in our population synthesis, the range of which becomes narrower towards low metallicities as we follow the AMR. Stars with $M \lesssim 1.5 M_{\odot}$ experience a small number of TDU episodes. After their last thermal pulse (when they are observed as post-AGB stars) they have not yet reached the asymptotic [hs/ls] ratio, which contributes to the spread observed. Most of the data can be fitted with

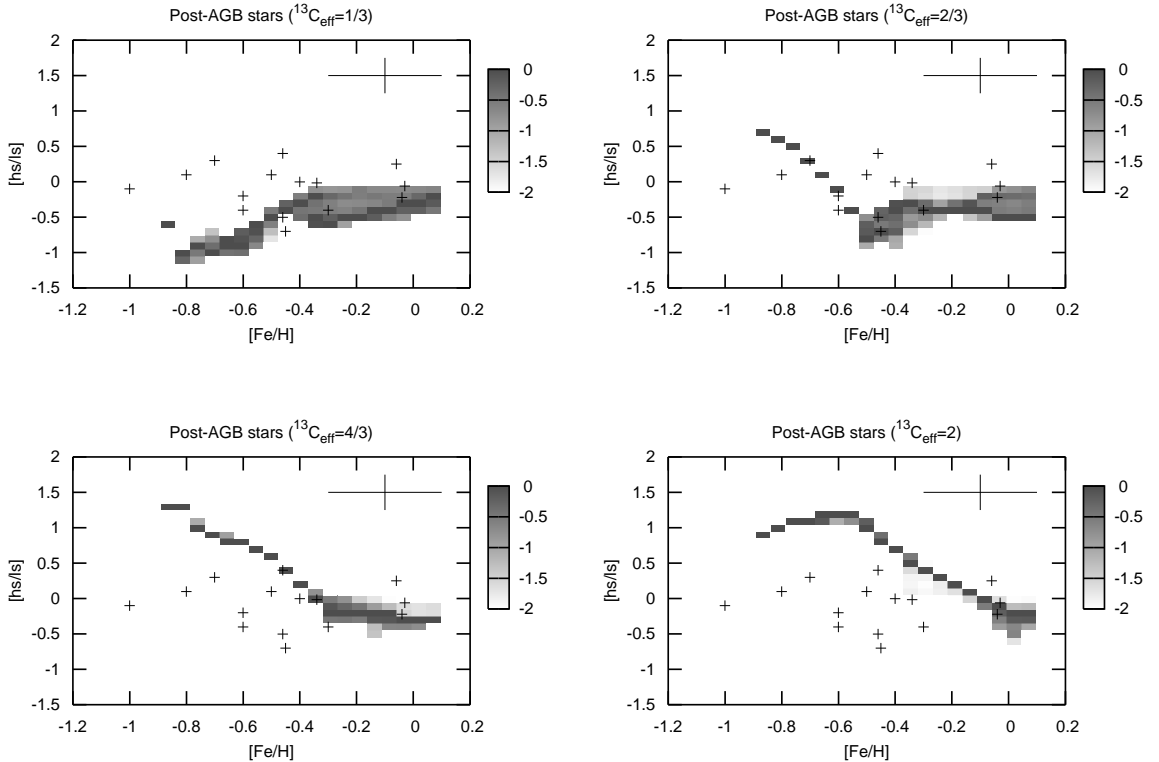


Figure 2.5: As Fig. 2.3, but for post-AGB stars The horizontal crosses are the observational data (see references in the text), which have an average error given by the size of the cross in the upper right of each plot.

$2/3 \lesssim {}^{13}\text{C}_{\text{eff}} \lesssim 4/3$, within the observational errors. There is only one exception at $[\text{Fe}/\text{H}] \sim -1$, which apparently needs a somewhat smaller ${}^{13}\text{C}_{\text{eff}}$. This object, IRAS07134+1005, has a very high heliocentric velocity (Van Winckel & Reyniers 2000) suggesting that it belongs to the galactic halo rather than the galactic disk.

Zr and C abundances of post-AGB stars

Post-AGB stars can also be used to provide constraints on the minimum core mass for TDU, the TDU efficiency, and the size of the ${}^{13}\text{C}$ pocket. The observed values of $[\text{Zr}/\text{Fe}]$ show a bimodal distribution: $[\text{Zr}/\text{Fe}] \approx 0$ and $1 \lesssim [\text{Zr}/\text{Fe}] \lesssim 2$, which suggests that some post-AGB stars did not experience TDU, while others did and suffered a strong enhancement of Zr (van Winckel 2003). This can be explained when we consider low mass stars ($M \lesssim 1.5 M_{\odot}$) at sub-solar metallicities. They have low-mass envelopes which easily become strongly *s*-enhanced. As shown in Fig. 2.6, only one TDU episode after the intershell material has become *s*-

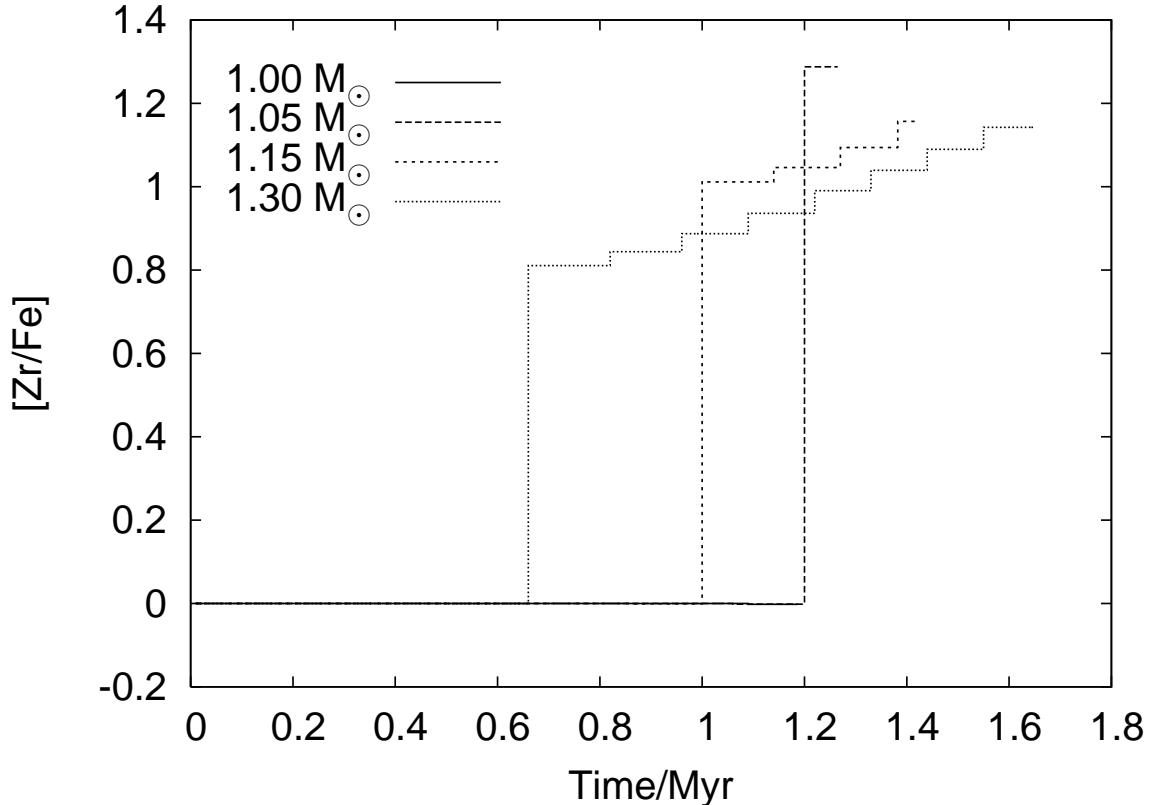


Figure 2.6: Enhancement of Zr in TP-AGB stars as function of time. The models shown are for $[\text{Fe}/\text{H}] = -0.5$, with initial masses as indicated in the figure. When the stars reach the post-AGB phase, i.e., by the end of their evolution, there is a strong Zr enhancement (~ 1 dex) as long as at least one *s*-enriched dredge-up episode has taken place. If no dredge-up occurs there is no enhancement at all, as seen in the case of the $1M_{\odot}$ star.

enriched is enough to raise their envelope abundance ratios by almost 1 dex. We compare the observational [Zr/Fe] ratios of van Winckel (2003), Reyniers et al. (2004) and Giridhar & Arellano Ferro (2005) to our models, from which we consider all post-AGB stars, both *s*-enhanced and not *s*-enhanced.

Intrinsically *s*-enhanced post-AGB stars are observed at metallicities as low as [Fe/H] ~ -1.0 (van Winckel 2003). When taking into account the AMR, this implies that at metallicities [Fe/H] $\lesssim -0.7$ stars with initial masses above $0.9 M_{\odot}$ must experience TDU. At [Fe/H] $\lesssim -0.3$, the observed number of *s*-enhanced stars (which experienced TDU) is comparable to that of stars with [Zr/Fe] ≈ 0 (which did not undergo TDU). Thus, taking into account the IMF and the initial mass range given by the AMR at low metallicities, we estimate the minimum initial mass at which TDU must take place so that the number of *s*-enhanced stars is similar to that of non-enhanced stars. Applying this in our models, we find the corresponding minimum core mass for TDU as a function of metallicity. The resulting relation between minimum core mass and metallicity is best modelled by the fitting formula of Karakas et al. (2002), with an offset $\Delta M_c^{\min} = -0.065 M_{\odot}$. This outcome depends somewhat on the adopted age-metallicity relation that sets the initial mass range of TP-AGB stars at each metallicity (Fig. 2.1), but the sensitivity of the mass of a low-mass star to its lifetime is only slight. Our result depends more strongly on the choice of mass loss. To test this we applied different mass-loss rates on the TP-AGB with the prescription of Reimers (1975), Eq. (2.5), by varying the coefficient η_{GB} from 0.5 to 3.0, and find that $0.055 \lesssim \Delta M_c^{\min} \lesssim 0.075$. This result is consistent with the findings of, e.g., Groenewegen & de Jong (1993), Marigo et al. (1999), Izzard et al. (2004), and Stancliffe et al. (2005) when studying the carbon star luminosity functions of the Small and Large Magellanic Clouds.

We now address the question of how much intershell material is dredged up to the surface. The surface *s*-process enhancement in our models is controlled by the dredge-up efficiency (λ) and by the fractional mass of the ^{13}C pocket relative to the intershell ($f_{13\text{C,IS}}$). The carbon enrichment in the envelope depends only on the amount of dredge-up, independent of the size of the ^{13}C pocket. The observations show that below [Fe/H] ~ -0.3 all *s*-enhanced post-AGB stars have C/O > 1 and that the non-enhanced ones have C/O < 1 (van Winckel 2003). We use this information to break the degeneracy between λ and $f_{13\text{C,IS}}$. Let $N_{s,\text{noC}}$ be the observed number of *s*-enriched post-AGB stars that have C/O < 1 and N_s be total number of *s*-enriched post-AGB objects. Fig. 2.7 illustrates the ratio $N_{s,\text{noC}}/N_s$ as a function of metallicity calculated with our models for different values of λ_{\min} . With a simple application of Bayesian statistics we calculate that, given the observed data distribution, $N_{s,\text{noC}}/N_s = 0$ and $N_s = 11$, there is a 32% probability that $N_{s,\text{noC}}/N_s > 0.09$ and only a 5% probability that $N_{s,\text{noC}}/N_s > 0.23$. The latter sets the 95% confidence limit $\lambda_{\min} \gtrsim 0.2$, as shown in Fig. 2.7. With this lower limit we calibrate $f_{13\text{C,IS}}$ to fit the Zr enhancement of post-AGB stars. Fig. 2.8 shows our population synthesis results for the [Zr/Fe] ratio calculated with different values of λ_{\min} and $f_{13\text{C,IS}}$, compared to the observations. The upper left panel shows our results for $\lambda_{\min} = 0$. With this choice there are no *s*-enhanced post-AGB stars at low metallicities ([Fe/H] $\lesssim -0.4$) since these would all be low-mass stars due to the AMR and they experience negligible dredge-up. This is in contradiction to the observations. Moreover, as shown above (Fig. 2.7), a choice of

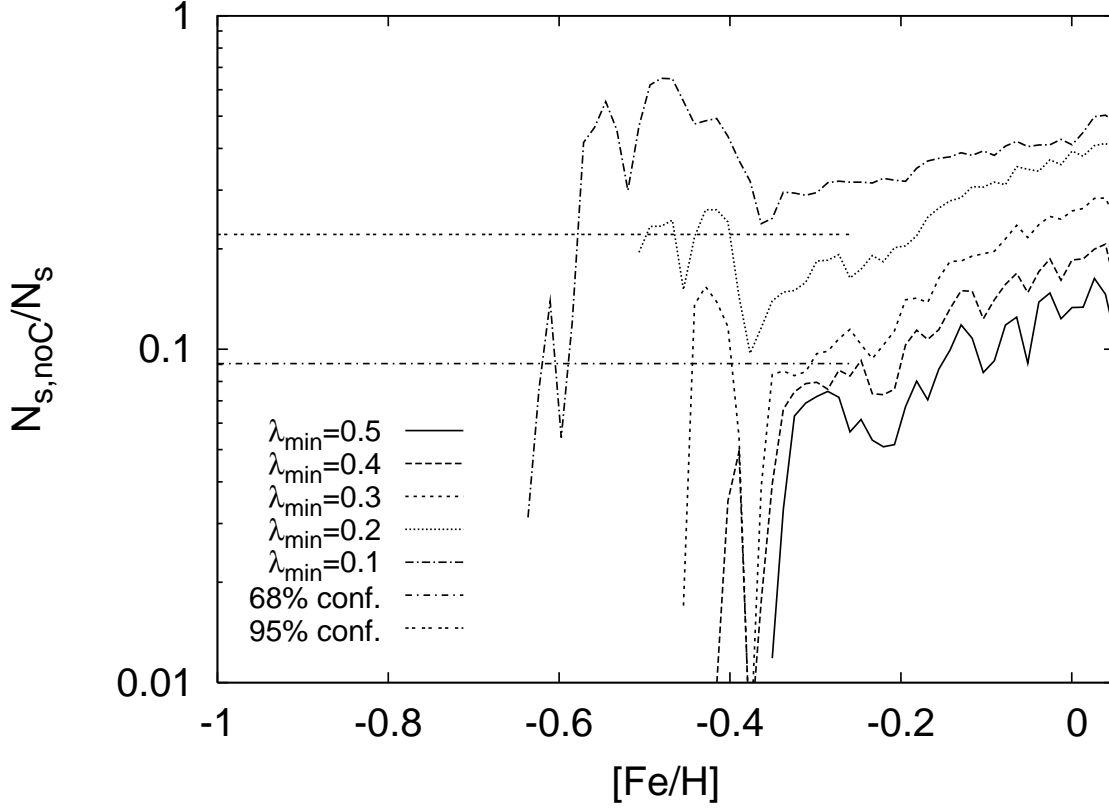


Figure 2.7: Ratio of the number of *s*-enhanced post-AGB stars which have $C/O < 1$ ($N_{s,noC}$) to the number of *s*-enhanced post-AGB stars (N_s) from our synthetic models. The curves show the ratios calculated with different values of λ_{min} , as indicated in the figure. The straight dash-dotted and double-dotted lines show the upper limit to the $N_{s,noC}/N_s$ ratio at $[Fe/H] \lesssim -0.3$, with a confidence of 68% and 95%, respectively, given the distribution of the observed data.

$\lambda_{min} < 0.2$ is not compatible with the number of carbon enhanced stars. If we choose $\lambda_{min} = 0.2$ (upper right panel) then low-metallicity *s*-enhanced post-AGB stars are indeed produced. The large spread in the *s*-enhancement at higher metallicities is due to stars with mass $M \gtrsim 3 M_{\odot}$. However, the choice $f_{13C,IS} = 0.05$, which roughly corresponds to that used by Gallino et al. (1998) for their detailed nucleosynthesis calculations, gives too much Zr for many of the *s*-enhanced post-AGB stars with $[Fe/H] \lesssim -0.5$. The lower right panel shows that most of the observations can be reproduced with $\lambda_{min} = 0.2$ and $f_{13C,IS} \approx 1/40$, with two exceptions which are extremely *s*-enhanced. From the constraint that all *s*-enhanced post-AGB stars are carbon stars, there is a 68% confidence lower limit on λ_{min} of 0.4. This implies that $f_{13C,IS} \approx 1/100$ is needed to fit the post-AGB observations (lower right panel of Fig 2.8). However, this choice of $f_{13C,IS}$ gives synthesised $[ls/Fe]$ and $[hs/Fe]$ ratios which are too small to reproduce those observed in MS/S, SC, and C stars. Fig. 2.9 shows a comparison of the observed $[ls/Fe]$ and $[hs/Fe]$ of MS/S, SC, and C stars to our models, calculated with $\Delta M_c^{min} = -0.065 M_{\odot}$, $\lambda_{min} = 0.2$, $f_{13C,IS} = 1/40$ and $^{13}C_{eff} = 4/3$. Most of the MS/S star abundances are fitted within

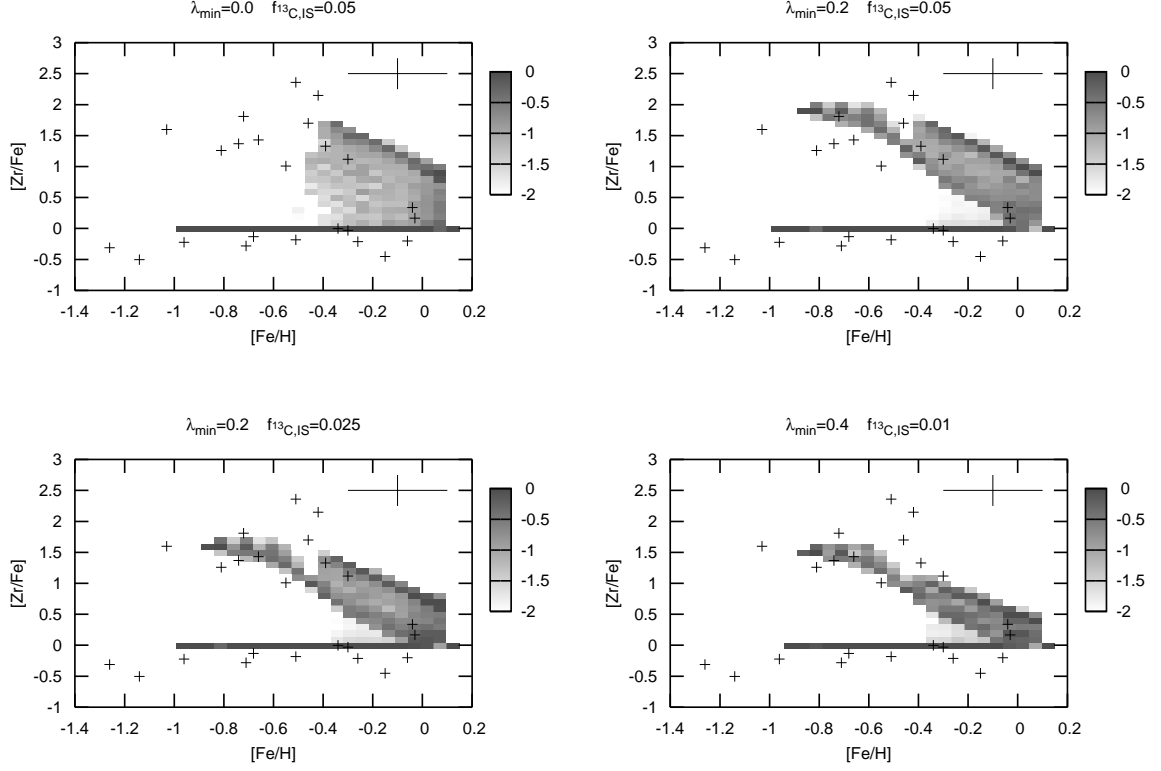


Figure 2.8: Post-AGB stellar population synthesis results compared to the observations. The grey scale is a logarithmic measure of the normalised number distribution of stars in the $[Zr/Fe]$ – $[Fe/H]$ plane for $^{13}C_{\text{eff}} = 2/3$. As indicated above the panels, plots are presented for different values of λ_{\min} and $f_{13C,IS}$. The crosses are the observational data (see references in the text), which have an average error given by the size of the cross in the upper right of each plot.

the errors, with two high-metallicity exceptions that are only matched with a larger choice of $^{13}C_{\text{eff}}$ or $f_{13C,IS}$. The s -process abundances of most of the SC and C stars in the galactic disk are also matched well using the same choice of free parameters, except for three low metallicity objects that need a smaller $^{13}C_{\text{eff}}$.

From the combined evidence of MS/S, SC, C, and post-AGB stars, we find that with a few exceptions, all observations of intrinsic s -enhanced stars can be matched by models with the following set of parameters:

- $\Delta M_{\text{c}}^{\min} = -0.065M_{\odot}$
- $\lambda_{\min} = 0.2$
- $f_{13C,IS} = 1/40$
- $2/3 \leq ^{13}C_{\text{eff}} \leq 4/3$.

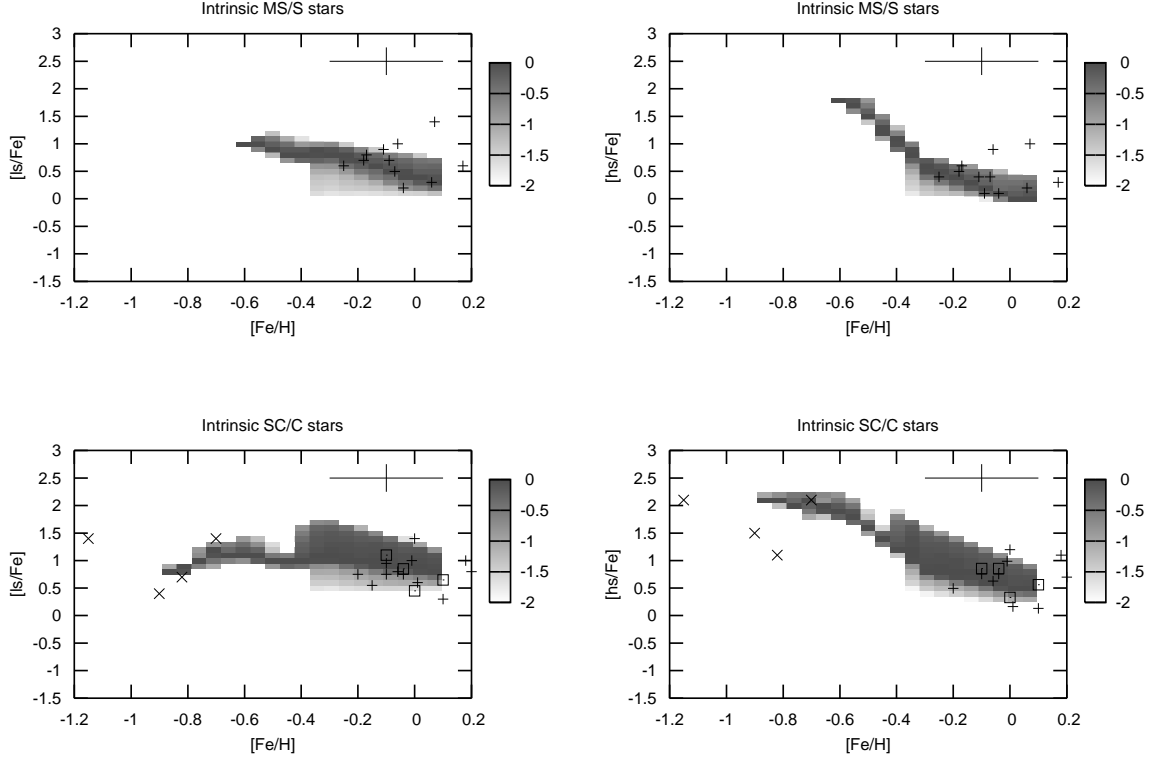


Figure 2.9: Stellar population synthesis results of MS/S stars (top panels) and SC/C stars (bottom panels) compared to the observations. The grey scale is a logarithmic measure of the normalised number distribution of stars in the $[\text{ls}/\text{Fe}]$ – $[\text{Fe}/\text{H}]$ plane (left panels) and the $[\text{hs}/\text{Fe}]$ – $[\text{Fe}/\text{H}]$ plane (right panels), using $^{13}\text{C}_{\text{eff}} = 4/3$ (as derived in §2.4.1 and §2.4.1), $\lambda_{\text{min}} = 0.2$ and $f_{^{13}\text{C},\text{IS}} = 0.025$. The observational data are from the same references and with the same coding as those of Fig. 2.3 and Fig. 2.4, which have an average error given by the size of the cross in the upper right of each plot.

However, the constraints we have set here depend somewhat on our choice of other rather uncertain parameters, namely the mass-loss rate and age–metallicity relation (see § 2.5).

2.4.2 Extrinsic *s*-enhanced stars

Extrinsic *s*-enhanced stars can be in any evolutionary stage prior to the TP-AGB phase, but they are mainly giants and main sequence stars. Their absolute *s*-process abundances cannot be studied without complete binary evolution models, but the abundance ratios of *s*-process elements are not substantially affected by binary processes. The $[\text{hs}/\text{ls}]$ ratio represents that of the former TP-AGB companion which produced the *s*-process elements and it can be reasonably approximated by taking into account the yields of single stellar evolution models. Fig. 2.10 shows a comparison of our synthetic $[\text{hs}/\text{ls}]$ ratios to the extrinsic star data from Busso et al. (2001), Aoki et al. (2002), Abia et al. (2002) and van Eck et al. (2003). Similar to our

results for intrinsic stars, the spread observed in these results is due to the range of initial masses that we use, although, in this case the mass range is wider and includes AGB stars up to 7-8 M_{\odot} . An AGB star of $M \gtrsim 5 M_{\odot}$ has a very thin intershell and a massive envelope, so its surface [hs/l_s] ratio varies smoothly between its value in the intershell and the solar ratio.

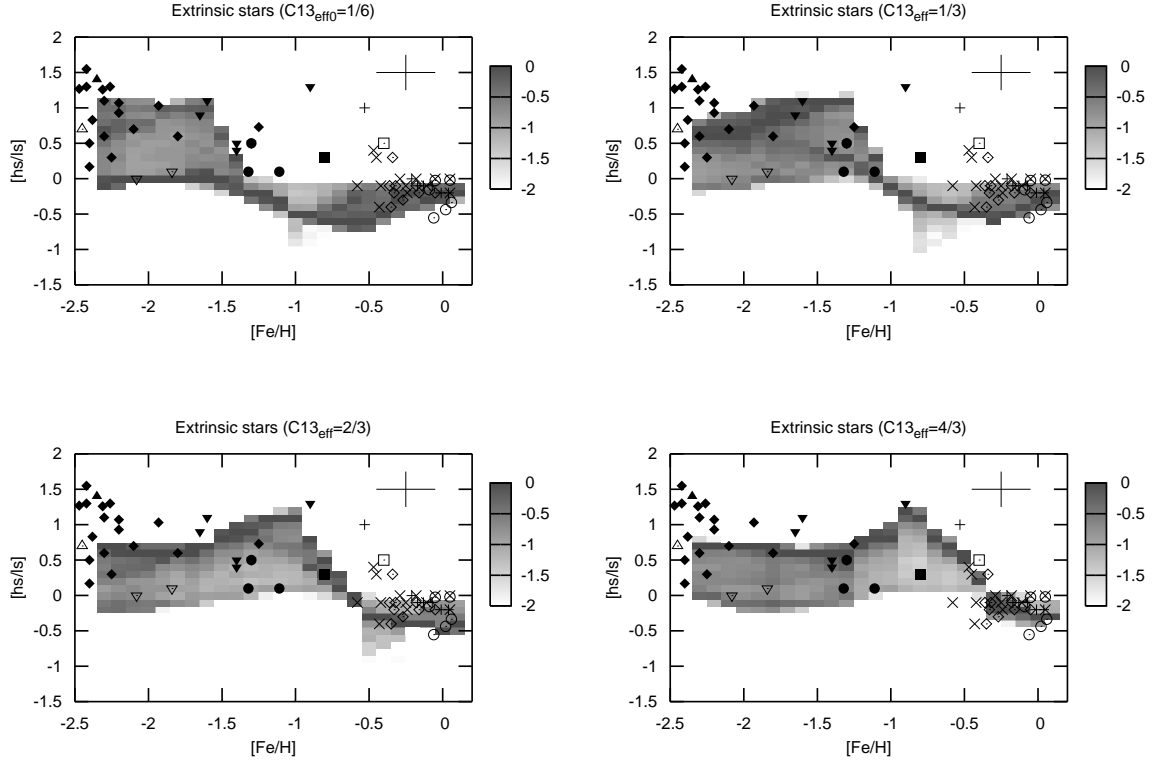


Figure 2.10: Population synthesis results for single-star yields compared to observations of extrinsic *s*-enhanced stars for different values of $^{13}\text{C}_{\text{eff}}$. The grey scale is a normalised logarithmic distribution of [hs/l_s] for a population of stars as a function of metallicity. The symbols indicate observed data from different stellar types and references as follows: + MS/S stars; x Ba II giants; diamond CH sub-giants; square CH giants; solid square C giant; solid triangle halo CH giant; solid circle halo yellow symbiotic; open triangle halo C-rich giant; solid triangle halo C-rich sub-giant; open inverted triangle halo N-rich dwarf, all previous gathered by Busso et al. (2001); open circle C stars from Abia et al. (2002); diamond lead stars gathered by Bisterzo et al. (2006). The observed data have an average error given by the size of the upper right cross in each plot.

We focus first on the galactic disk ($[\text{Fe}/\text{H}] \gtrsim -1$) stars. Fig. 2.10 shows that no single choice of $^{13}\text{C}_{\text{eff}}$ value can make our results fit all the observational data, but almost all observations can be fitted with a range of values $2/3 \lesssim ^{13}\text{C}_{\text{eff}} \lesssim 4/3$. This is consistent with what we found for the intrinsic *s*-enhanced stars (see §2.4.1).

For $[\text{Fe}/\text{H}] \lesssim -1$, our synthetic [hs/l_s] ratios are relatively insensitive to changes in $^{13}\text{C}_{\text{eff}}$ because the hs-element synthesis saturates, opening the way to the synthesis of lead. There is some indication that a smaller value of $^{13}\text{C}_{\text{eff}}$ is needed to reproduce objects with $[\text{Fe}/\text{H}]$

$\lesssim -2$ which have a high [hs/ls], but even when using small $^{13}\text{C}_{\text{eff}}$ values [hs/ls] does not exceed about 1 dex. Thus we are unable to explain the extreme low-metallicity objects with $[\text{hs}/\text{ls}] \gtrsim 1.2$. Our synthetic calculations do not extend below $[\text{Fe}/\text{H}] < -2.3$ because of the lack of detailed models with metallicity below this value.

Lead stars

Lead stars have an enhanced lead abundance and are found at low metallicities. As discussed above, the [hs/ls] ratio remains roughly constant at low metallicities due to the saturation of the ls- and hs-element synthesis, which indicates that lead is being synthesised (Gallino et al. 1998). Consequently, the ratio of Pb to hs-elements is sensitive to the choice of $^{13}\text{C}_{\text{eff}}$. We use [Pb/hs] data gathered by Bisterzo et al. (2006) to compare with our synthesis results. In

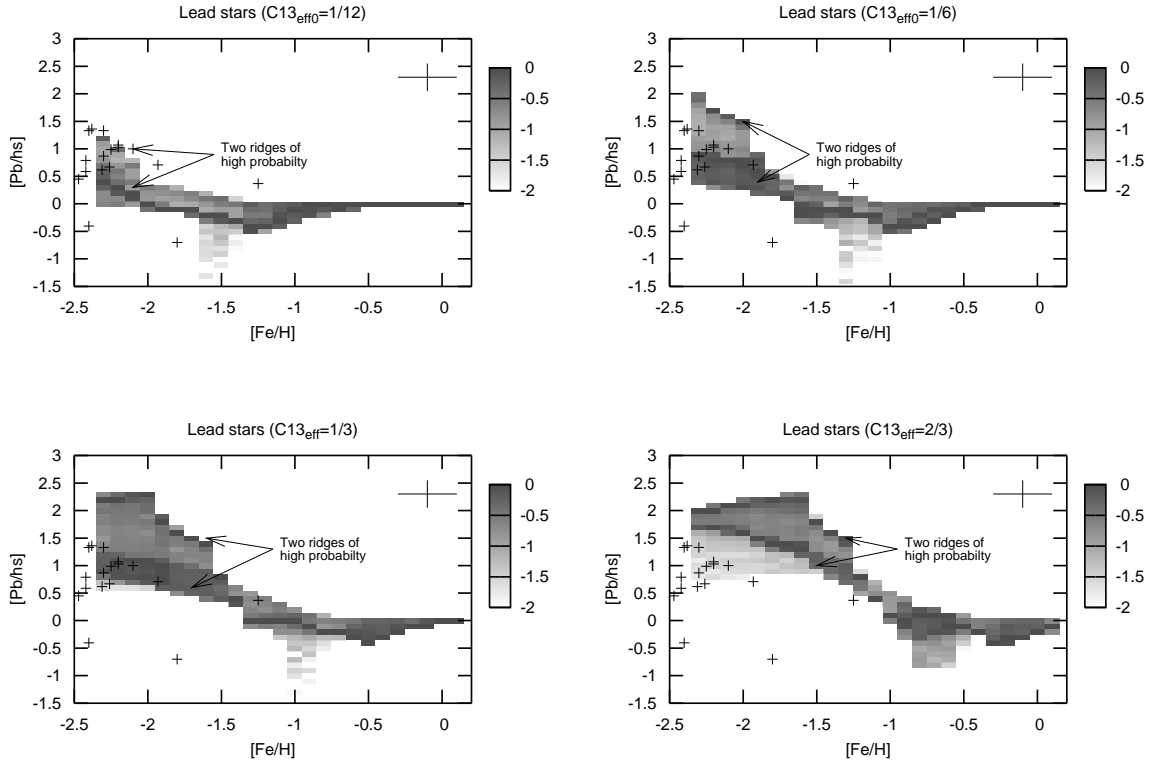


Figure 2.11: [Pb/hs] results from our population synthesis of lead stars, shown in the same way as in fig. 2.10 and compared to the data gathered by Bisterzo et al. (2006). The upper right cross shows the average error of the data points.

the [Pb/hs] vs. [Fe/H] plane (Fig. 2.11) we see that our results show a pattern that shifts in metallicity if $^{13}\text{C}_{\text{eff}}$ is varied, similar to the shift in [hs/ls] pattern at higher metallicities. The reason for this behaviour is the change in ratio of the number of free neutrons to the number of seed nuclei, as explained in §2.4.1. We find that also for [Pb/hs] a spread naturally arises

in our population synthesis results. This spread is mostly due to the fact that, as discussed by Gallino et al. (1998) (see their Fig. 6), the neutron exposure in the ^{13}C pocket decreases with pulse number. This effect is even more pronounced at lower metallicities, causing the $[\text{Pb}/\text{hs}]$ ratio to shift to much lower values as the evolution proceeds. This is illustrated by the models computed by Busso et al. (2001), shown in Fig. 2.12. As a consequence, there

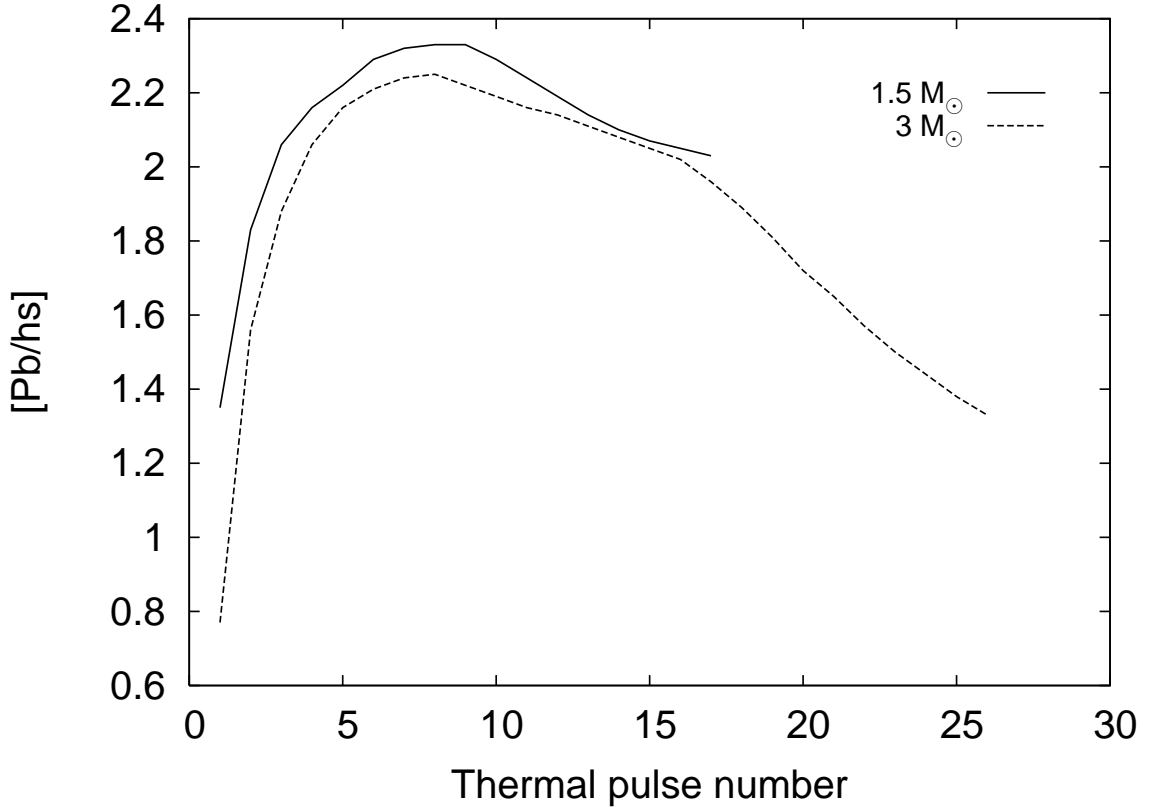


Figure 2.12: $[\text{Pb}/\text{hs}]$ during the evolution of $1.5 M_{\odot}$ and $3 M_{\odot}$ models of $[\text{Fe}/\text{H}] = -2.3$ with $^{13}\text{C}_{\text{eff}} = 1/3$.

are two ridges of high probability in the model results shown in Fig. 2.11. One follows the higher $[\text{Pb}/\text{hs}]$ values and corresponds to the contribution of low-mass stars (about $1 M_{\odot}$), which is high due to their large IMF weight. The other ridge, which follows intermediate values, is the contribution of stars with masses around $2.5 M_{\odot}$. Despite their smaller IMF weight, the ejecta of these stars are massive enough to make their contribution comparable to that of the low-mass stars. This effect is also visible in our synthetic $[\text{hs}/\text{ls}]$ results, e.g., in the top panels of Fig. 2.10. Most observations are fitted by the contribution of $\sim 2.5 M_{\odot}$ stars when choosing $^{13}\text{C}_{\text{eff}} \approx 1/3$ (lower left panel in Fig. 2.11), except for two outliers which have $[\text{Pb}/\text{hs}] < 0$. These outliers, however, have large error bars which extend to $[\text{Pb}/\text{hs}] \approx 0$ (van Eck et al. 2003). The upper left panel in Fig. 2.11 shows that a value of $^{13}\text{C}_{\text{eff}}$ as small as $1/12$ still marginally fits the low-metallicity stars ($[\text{Fe}/\text{H}] \lesssim -2$). On the other hand, a choice of $^{13}\text{C}_{\text{eff}} \approx 2/3$ results in too large $[\text{Pb}/\text{hs}]$ values (lower right panel in Fig. 2.11). This result

reaffirms our results for the extrinsic-star [hs/ls] values which suggest that a somewhat smaller value of $^{13}\text{C}_{\text{eff}}$ is needed to fit low-metallicity halo stars compared to those in the galactic disk. This is also consistent with what we found in §2.4.1, regarding the object IRAS07134+1005.

As stated above our calculations do not extend below $[\text{Fe}/\text{H}] < -2.3$, but we notice that lead stars with lower metallicity could also be explained if the trend shown by our models continues at lower metallicities. This seems likely because [Pb/hs] does depend mostly on $^{13}\text{C}_{\text{eff}}$ and not on other uncertain parameters in our models, however, explaining those stars at $[\text{Fe}/\text{H}] < -2$ which show $[\text{hs}/\text{ls}] \gtrsim 1.2$ is still a problem.

Finally, we note that Cui & Zhang (2006) also presented a possible solution to explain the spread of [Pb/hs] observed in low-metallicity stars. These authors obtained a spread of neutron exposures (and hence [Pb/hs]) in low-metallicity AGB stars due to variations of the inter-pulse period in stars of different masses. Their results are based on the assumption that the neutron irradiation time is proportional to the inter-pulse period. However, this assumption is incorrect since the neutron irradiation time depends instead on the timescale at which the $^{13}\text{C}(\alpha, n)^{16}\text{O}$ reactions occur. At the temperature of 10^8 K that Cui & Zhang (2006) use in their models, the timescale for α captures is of the order of 300 yr (see Fig. 2 of Gallino et al. 1998), and this is independent of the inter-pulse period. In our models, instead, the spread in [Pb/hs] derives naturally from the fact that the neutron exposure changes with time, especially at low metallicities.

2.5 Conclusions and discussion

Based on the results of our population synthesis study, we find that it is not possible to reproduce the observed heavy-element abundances of *s*-enhanced stars with the standard set of values for the free parameters in our AGB models. The minimum core mass for TDU has to be reduced by at least 10 per cent with respect to what theoretical models predict; low-mass stars must have a significant TDU efficiency and the ^{13}C pocket mass must be somewhat lower than what is usually considered standard. We also find that the observations can be matched with a narrow range of $^{13}\text{C}_{\text{eff}}$ values and that the mean $^{13}\text{C}_{\text{eff}}$ value in this range apparently decreases with metallicity.

The observations in the metallicity range $[\text{Fe}/\text{H}] \gtrsim -1$ are fitted well by $2/3 \lesssim ^{13}\text{C}_{\text{eff}} \lesssim 4/3$, i.e., a spread of a factor of 2, while Busso et al. (2001) needed a factor of ~ 20 . This is a consequence of the natural spread that we find in the *s*-process element ratios caused mainly by the truncation of AGB evolution due to the total loss of the stellar envelope. Stars with initial mass $M \lesssim 1.5 M_{\odot}$ start the TP-AGB phase with a relatively similar core mass, but different envelope mass. Consequently, a star with a certain low mass will experience fewer thermal pulses than one with a slightly higher mass, which affects its yields and composition during its life as a TP-AGB star. A different choice of mass loss in our models, either during the red giant branch or the AGB phase, would move the mass range in which this effect takes place, but not eliminate it.

At $[\text{Fe}/\text{H}] \lesssim -1$ a spread in $[\text{Pb}/\text{hs}]$ arises because of the shift in the neutron exposure. Observations at these lower metallicities need a somewhat lower value $^{13}\text{C}_{\text{eff}} \approx 1/3$, perhaps down to $\approx 1/12$. This result may be due to the increasingly important effect of α -enhanced light neutron poisons at low metallicities (Busso et al. 1999), which needs to be investigated in more detail.

It is reassuring that our conclusion of a small spread in $^{13}\text{C}_{\text{eff}}$ is reached independently by the study of isotopic s -process signatures in pre-solar silicon carbide (SiC) grains from carbon stars. While Lugaro et al. (2003) needed a spread of ~ 24 in the values of $^{13}\text{C}_{\text{eff}}$ to cover the SiC data, by eliminating the effect of contamination of solar material, more recent laboratory studies (Barzyk et al. 2007; Marhas et al. 2007) have also reduced the spread of the $^{13}\text{C}_{\text{eff}}$ values needed to cover the grain data to exactly the same range we found here. Although pre-solar grains can only give us information on the s -process taking place in stars with $[\text{Fe}/\text{H}] \gtrsim -1$, such an independent check also gives us confidence in our results at lower metallicities.

Now the question arises as to whether the small spread that we find is compatible with the possible mechanisms currently proposed for the proton diffusion leading to the formation of the ^{13}C pocket. We note that semi-convection (Hollowell & Iben 1988), hydrodynamical overshooting (Herwig et al. 1997), and gravity waves (Denissenkov & Tout 2003), which are three out of the four proposed mechanisms, produce a proton profile with the number of protons varying continuously from the envelope value to zero. The possible shapes of the proton profile were discussed by Goriely & Mowlavi (2000, see their Fig. 10), who concluded that “the s -process predictions are only weakly dependent on the shape of the H-profile”. Hence we would not expect a wide range of neutron exposures to occur in the current scenario. Future work should quantitatively link the shape of the proton profile to the range of $^{13}\text{C}_{\text{eff}}$ we found in this study. The fourth process proposed for the formation of the ^{13}C neutron source is rotation (Langer et al. 1999; Herwig et al. 2003). Also in this case the formation of the ^{13}C pocket starts from a continuous proton profile; however, current models find that further mixing during the inter-pulse period completely inhibits the s -process (Herwig et al. 2003; Siess et al. 2004). Future work is needed to ascertain this point.

To explain the existence of Galactic post-AGB stars that are s -process enhanced at $[\text{Fe}/\text{H}] \sim -1$, we find that the minimum core mass for TDU must be $0.055\text{--}0.075 M_{\odot}$ smaller than that found in the models of Karakas et al. (2002) and Stancliffe et al. (2004). This is consistent with the findings of several authors who studied the carbon-star luminosity functions of the SMC and LMC (e.g., Groenewegen & de Jong 1993; Marigo et al. 1999; Izzard et al. 2004; Stancliffe et al. 2005) and sets a strong constraint on future detailed evolutionary model results.

We find that to account for the fact that all 11 Zr-enhanced post-AGB stars observed so far are also C enhanced, $\lambda_{\text{min}} \gtrsim 0.2$ in stars of mass $M \lesssim 1.5 M_{\odot}$. The precise value of this lower limit may depend somewhat on our adopted choices for mass loss, the AMR, and the minimum core mass for TDU. We leave a detailed analysis of this dependence for future study. However, it is clear from our results that a value of $\lambda = 0$ cannot reproduce the observations, and we are therefore confident in concluding that stars of mass $M \lesssim 1.5 M_{\odot}$ must experience

a significant amount of TDU.

The amount of Zr enhancement in post-AGB stars is determined by the amount of third dredge-up and the size of the ^{13}C pocket. Assuming $\lambda_{\text{min}} = 0.2$ indicates that in our models the ^{13}C pocket must have a mass of 1/40 of that of the intershell to fit the observed data from Zr-enhanced post-AGB stars. This is somewhat smaller than the size of the ^{13}C pocket assumed in the models of Gallino et al. (1998), which is about 1/20 of the mass of the intershell.

Future detailed modelling of AGB stars will need to address the constraints we have set here. We are currently extending our analysis of extrinsic *s*-enhanced stars by means of *binary* population synthesis, i.e., by explicitly following the evolution and interaction processes of populations of binary stars.

acknowledgements The authors are deeply indebted to Roberto Gallino for providing the data from his detailed nucleosynthesis models and for insightful discussions and comments on this work. ABM thanks Maarten Reyniers and Hans van Winckel for useful discussions and for providing data on post-AGB stars. ABM also thanks Selma de Mink for refreshing his knowledge of statistical analysis. RGI is supported by NWO. ML is supported by NWO (VENI fellow).

Chapter 3

Stellar population synthesis of post-AGB stars: the *s*-process in MACHO 47.2496.8

A. Bonačić Marinović, M. Lugaro, M. Reyniers, H. Van Winckel,
Astronomy & Astrophysics, v. 472, p. L1-L4 (2007)

Abstract The low-metallicity RV Tauri star MACHO 47.2496.8, recently discovered in the Large Magellanic Cloud, is highly enriched in carbon and heavy elements produced by the *slow* neutron capture process (*s*-process), and is most probably a genuine post-C(N-type) asymptotic giant branch (AGB) star. The intrinsic interpretation of the enrichment is further strengthened by detection of a significant infrared excess. The circumstellar dust is the relic of a recent episode of heavy mass loss. We use the analysis of the abundances of MACHO 47.2496.8 to constrain free parameters in AGB models. We test which values of the free parameters describing uncertain physical mechanisms in AGB stars, namely the third dredge-up and the features of the ^{13}C neutron source, produce models that better match the abundances observed in MACHO 47.2496.8. We carry out stellar population synthesis coupled with *s*-process nucleosynthesis using a synthetic stellar evolution code. The *s*-process ratios observed in MACHO 47.2496.8 can be matched by the same models that explain the *s*-process ratios of Galactic AGB and post-AGB stars of metallicity $> Z_{\odot}/10$, except for the choice of the effectiveness of ^{13}C as a neutron source, which has to be lower by roughly a factor of 3 to 6. The less effective neutron source for lower metallicities is also required when comparing population synthesis results to observations of Galactic halo *s*-enhanced stars, such as Pb stars. The $^{12}\text{C}/^{13}\text{C}$ ratio in MACHO 47.2496.8 cannot be matched simultaneously and requires the occurrence of extra-mixing processes. The confirmed trend of the decreased efficiency of the ^{13}C neutron source with metallicity requires an explanation from AGB *s*-process models. The present work is to date the first comparison between theoretical models and the detailed abundances of an extragalactic post-AGB star.

3.1 Introduction

Slow neutron capture (*s*-process) elements are synthesised in the intershell region between the C–O core and the convective H-rich envelope of asymptotic giant branch (AGB) stars. The main neutron source is believed to be ^{13}C nuclei, releasing neutrons via the $^{13}\text{C}(\alpha, n)^{16}\text{O}$ reaction in a thin layer of the intershell (the ^{13}C *pocket*, see e.g. Gallino et al. 1998 for details). The *s*-process elements are mixed to the stellar surface by recurrent episodes of third dredge-up (TDU), where they are observed. A high abundance of ^{13}C in the pocket can be produced by $^{12}\text{C}+p$ reactions if protons are mixed from the convective envelope into the radiative ^{12}C -rich intershell. This mixing would likely occur at the end of each TDU episode, when a sharp discontinuity is left between the convective and the radiative regions. However, it is not yet clear what mechanism produces this mixing. The extent of the mixing, which makes the effectiveness of the ^{13}C neutron source, is the most uncertain parameter in *s*-process models (see e.g. Busso et al. 1999; Lugaro et al. 2003; Herwig 2005, for discussion).

Post-AGB stars are in the fast evolutionary phase between the AGB and white dwarf tracks. The strong mass loss at the end of the AGB has stopped, but they are not yet hot enough to ionise their circumstellar medium and to produce a planetary nebula. Their elemental abundances are the result of their evolutionary history, thus they can be used to probe and constrain the nucleosynthesis that takes place in AGB stars, in particular the *s*-process.

A peculiar post-AGB object, MACHO 47.2496.8, was found in the Large Magellanic Cloud (LMC) by Pollard & Lloyd Evans (2000) and analysed in detail by Reyniers et al. (2007). Its main features are a very low metallicity ($[\text{Fe}/\text{H}]=-1.4$), excess of carbon over oxygen ($\text{C}/\text{O}>2$ with $^{12}\text{C}/^{13}\text{C}=200\pm 25$), an enhancement of 1.2 dex of light *s*-process elements (ls) compared to iron, a strong enhancement of heavy *s*-process elements (hs) compared to iron of 2.1 dex, and a similar enhancement of lead over iron. In Reyniers et al. (2007), it was argued that the luminosity ($\sim 5000 L_{\odot}$) and the specific pulsational behaviour (RV Tauri like) of MACHO 47.2496.8 favour an *intrinsic* origin of the *s*-process enrichment, although an extrinsic scenario in which the enrichment is caused by a former AGB companion, now on the white dwarf track, could not be excluded.

We have updated the Spectral Energy Distribution (SED) of MACHO 47.2496.8 presented in Reyniers et al. (2007) by adding the newly released Spitzer SAGE data (Meixner et al. 2006) of the source. The new data reveal a small but clear infrared excess starting around $5\mu\text{m}$ (Fig. 3.1). In the Galaxy, the RV Tauri pulsators with a dust excess are dominated by binaries, consisting of a post-AGB primary and an unevolved companion. In these systems, the dust is trapped in a stable circumbinary disc (de Ruyter et al. 2006). The LMC RV Tauri stars detected by the Macho experiment are also dominated by disc sources (Reyniers & van Winckel 2007) and the SAGE data reveal that the typical colours yield a $\text{K}-[5.8\mu\text{m}] > 2.5$ and $[8\mu\text{m}]-[24\mu\text{m}]$ indicative of a dust excess with a hot dust component.

The colours of MACHO 47.2496.8 ($\text{K}-[5.8]=0.8$ and $[8]-[24]=2.4$) are significantly different, showing that the excess is much colder than in the suspected disc sources. We conclude that the dust excess of MACHO 47.2496.8 corroborates the post-AGB status of the object in

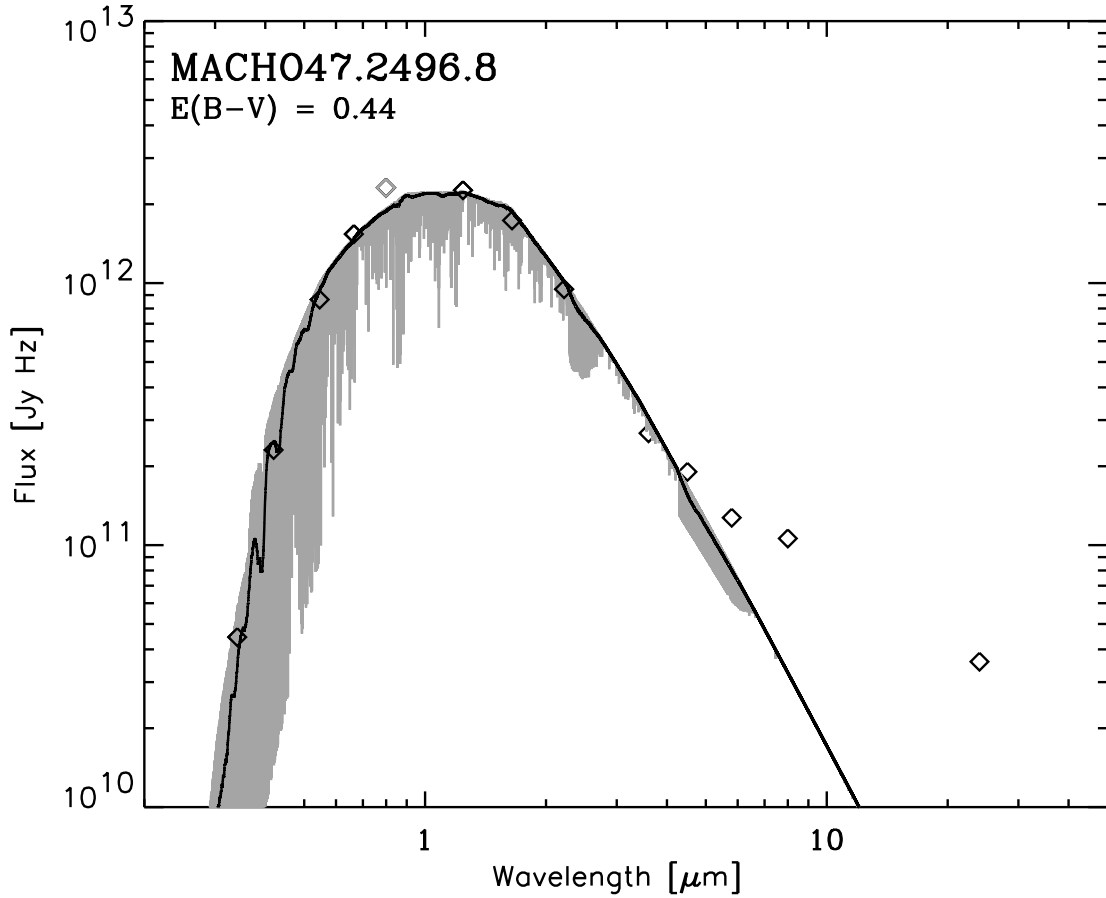


Figure 3.1: The spectral energy distribution of MACHO 47.2496.8 as in Reyniers et al. (2007), but updated with Spitzer SAGE fluxes, revealing the presence of circumstellar dust. Diamonds are the measured magnitudes (from blue to red): Geneva U, B, V and Cousins R taken with C2+Euler; I from DENIS (in gray), SAAO J, H, K, and the Spitzer SAGE fluxes (3.6, 4.5, 5.8, 8.0, and 24 μm). The MARCS model is shown in gray, while a smoothed version is shown with a full black line. The I magnitude could not be fitted, possibly due to a phase difference.

which the excess is a relic of a recent phase of dusty mass loss. The object is an ideal source to study the dust formation in metal poor conditions. In principle, it could still represent the post-AGB phase of a former, extrinsically enriched, CH star (about 5% of the carbon stars in the Stephenson 1989, catalog are extrinsically *s*-process and carbon enriched CH-stars) but we consider that it is much more likely that the object is a genuine intrinsically enriched post-AGB star.

In this contribution, we focus on the modelling of the chemical content assuming that the object is indeed intrinsically enriched. By comparing recent stellar population calculations including nucleosynthesis of *s*-process elements to observations of Galactic stars, Bonačić Marinović et al. (2007a, hereafter Paper I) have set constraints on several free parameters

included in their models: the minimum core mass for TDU, the TDU efficiency (λ), the effectiveness of the ^{13}C neutron source ($^{13}\text{C}_{\text{eff}}$), and the size in mass of the ^{13}C pocket. In this paper we use those models to interpret the abundances of MACHO 47.2496.8 and determine whether they can be reproduced using the same set of values of the free parameters found in Paper I.

We calculated populations of post-AGB stars with our rapid synthetic stellar evolution code, which includes *s*-process nucleosynthesis based on the models of Gallino et al. (1998). This code is described in detail in Paper I and the population synthesis procedure is done in the same fashion as in Paper I.

We run our models on a grid of 50 metallicity values, $[\text{Fe}/\text{H}]$, linearly separated, in the range $-2.0 < [\text{Fe}/\text{H}] < -0.5$ and 500 initial masses, M_i , logarithmically separated, in the range $0.7 M_{\odot} < M_i < 1.2 M_{\odot}$, weighed by the initial mass function of Kroupa et al. (1993). In contrast to Paper I, we do not consider an age-metallicity relation to calculate the range of masses given that MACHO 47.2496.8 belongs to the LMC and age-metallicity relations for the LMC are uncertain due to the low precision of age estimates (see e.g. Cole et al. 2005). In addition, if we apply the age-metallicity relation from Cole et al. (2005) the most massive AGB objects obtained with the metallicity of MACHO 47.2496.8 are not massive enough to experience dredge-up (about $0.85 M_{\odot}$ in their zero age main sequence).

The synthetic models are carried out applying the prescription of Vassiliadis & Wood (1993) to account for the mass loss. We employ the free-parameter values found in Paper I, which provide the best match for the overall properties of Galactic *s*-enhanced AGB and post-AGB stars: a shift of the minimum core mass for TDU $\Delta M_c^{\text{min}} = -0.065 M_{\odot}$ with respect to the models of Karakas et al. (2002), a minimum asymptotic TDU efficiency $\lambda_{\text{min}} = 0.2$, and a ^{13}C -pocket size, given as a fraction of the intershell mass $f_{^{13}\text{C},\text{IS}} = 1/40$. In particular, the relatively high λ_{min} is needed in order to match the number of *s*-process enhanced Galactic post-AGB star that are also carbon rich (see Paper I). Once the TDU parameters are fixed, observed *s*-process enhancements such as the $[\text{Zr}/\text{Fe}]$ ratio in Galactic post-AGB stars, can be matched by adjusting $f_{^{13}\text{C},\text{IS}}$ to a somewhat smaller value than that usually employed in single star models with less efficient TDU (Gallino et al. 1998; Goriely & Mowlavi 2000). With these choices of the free parameters the abundances observed in all the other types of intrinsic AGB *s*-enhanced stars (namely MS, S, SC and C stars) are also reproduced (see Paper I).

The parameters described above affect the overall enhancement of *s*-process elements with respect to Fe at the stellar surface, i.e., $[\text{ls}/\text{Fe}]$ and $[\text{hs}/\text{Fe}]$. However, they do not affect the relative distribution of *s*-process abundances, represented by the $[\text{hs}/\text{ls}]$ and $[\text{Pb}/\text{hs}]$ ratios, which is mainly a function of $^{13}\text{C}_{\text{eff}}$. In Paper I we found that, for Galactic objects with $[\text{Fe}/\text{H}] \gtrsim -1$, $^{13}\text{C}_{\text{eff}}$ ranges between approximately 2/3 and 4/3 of the standard value introduced by Gallino et al. (1998, see details in Paper I), while a value reduced by roughly a factor of 6 to 12 is needed to fit Pb stars, which are lower metallicity, extrinsically enriched halo objects. Here we compare our results with a range of values for this parameter to the observational data of MACHO 47.2496.8.

3.2 Results

We select *s*-process enhanced post-AGB stars from our models by choosing those TP-AGB objects that have $[\text{ls}/\text{Fe}] \geq 0.25$ or $[\text{hs}/\text{Fe}] \geq 0.25$ and an envelope mass $\leq 0.03 M_{\odot}$. Figure 3.2 shows stellar population results computed with different $^{13}\text{C}_{\text{eff}}$ values and compared to the observed *s*-process element ratios of MACHO 47.2496.8 measured by Reyniers et al. (2007). The grey scale measures the distribution of stars over the plotted *s*-process ratio in terms of metallicity. The darker area represents the contribution of stars with initial mass $M_i \approx M_{\odot}$, which are the most numerous according to the initial mass function that we consider. A good match to the observations for both $[\text{hs}/\text{ls}]$ and $[\text{Pb}/\text{hs}]$ ratios is obtained with $^{13}\text{C}_{\text{eff}}$ 1/3 to 1/6 of the standard value. Any smaller $^{13}\text{C}_{\text{eff}}$ value is inconsistent given that the pattern of $[\text{hs}/\text{ls}]$ as a function of metallicity would shift towards lower metallicities (for a detailed description see Paper I).

3.3 Stellar population synthesis models

The models reported in Fig. 3.2 can also be employed to interpret the composition of the Galactic post-AGB star IRAS07134+1005. This object has metallicity $[\text{Fe}/\text{H}] \sim -1$ and a very high heliocentric velocity (Van Winckel & Reyniers 2000), suggesting that it belongs to the Galactic halo rather than the disc. In Paper I it was discussed that this object “apparently needs a somewhat smaller $^{13}\text{C}_{\text{eff}}$ ” than Galactic post-AGBs of higher metallicity; however, because of the age-metallicity relation employed in Paper I it was not possible to model post-AGB stars of such low metallicity. With the models presented here, we can now confirm that the $[\text{hs}/\text{ls}]$ ratios approximately equal to zero observed in IRAS07134+1005 can be well matched by $^{13}\text{C}_{\text{eff}}=1/3$. The same conclusion holds for the intrinsic halo C star HD 189711 with $[\text{Fe}/\text{H}]=-1.14$ and $[\text{hs}/\text{ls}]=0.7$ shown in Fig. 4 of Paper I. We also note that this value of $^{13}\text{C}_{\text{eff}}$ is not in disagreement with observations of different types of extrinsic *s*-process stars (such as halo CH giant, halo yellow symbiotic, and Pb stars) in the same metallicity range (see Fig. 10 of Paper I).

The $[\text{hs}/\text{Fe}]$ and $[\text{ls}/\text{Fe}]$ ratios of MACHO 47.2496.8 are well reproduced by our results for intrinsically *s*-process enhanced post-AGB stars with the choice of $^{13}\text{C}_{\text{eff}} = 1/3$ to $1/6$ (the choice of $1/3$ is represented in Fig. 3.3) and without the need for any modification of the remaining free parameters, which, as described above, were already set according to the properties of Galactic post-AGB stars.

A problem arises when considering the C/O and, in particular, the $^{12}\text{C}/^{13}\text{C}$ ratio in MACHO 47.2496.8. With the high TDU assumed in our model we obtain $\text{C}/\text{O} > 10$ and $^{12}\text{C}/^{13}\text{C}$ ratios at least an order of magnitude higher than those observed. A better solution is possible by decreasing λ_{min} . For example, using $\lambda_{\text{min}}=0.1$ we obtain $\text{C}/\text{O} > 4$ and $^{12}\text{C}/^{13}\text{C} > 300$. Then, we need to increase $f_{^{13}\text{C},\text{IS}}$ to $1/20$ to match the $[\text{ls}/\text{Fe}]$ and $[\text{hs}/\text{Fe}]$ ratios. The problem is that, with this choice, we do not match the number of *s*-process enhanced Galactic post-AGB star that are also carbon rich (see Paper I) and it is difficult to find a consistent solution for these

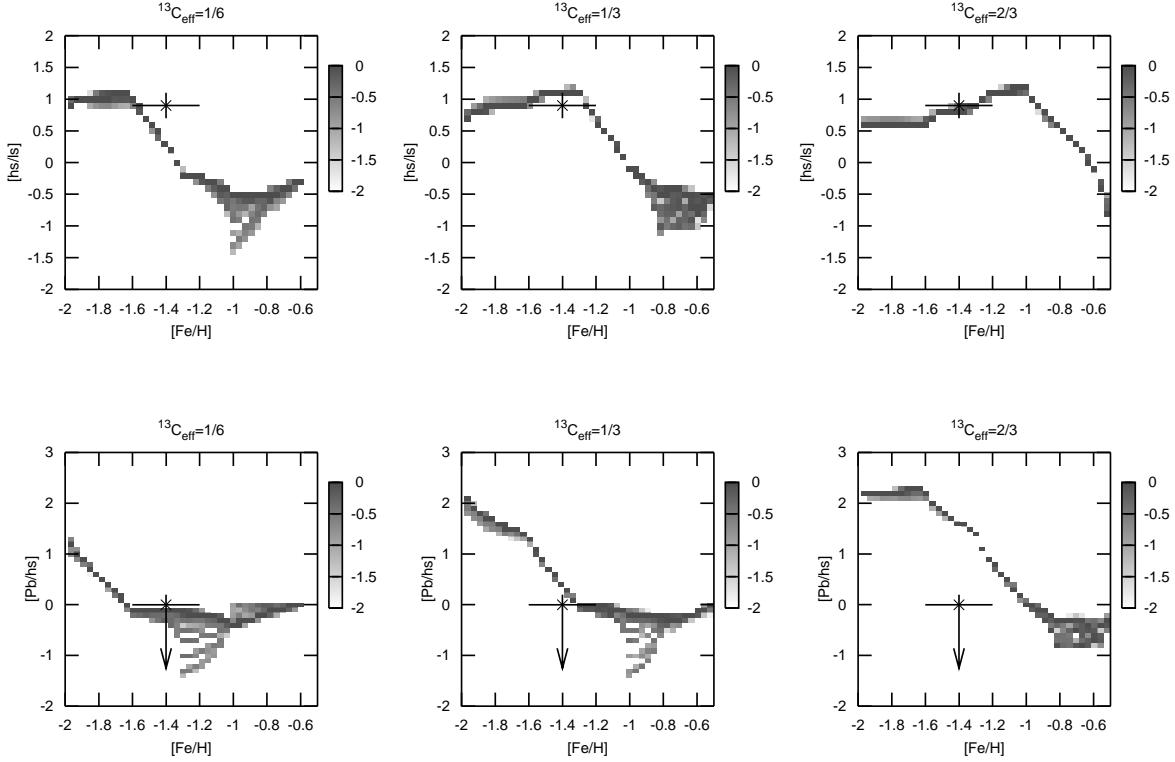


Figure 3.2: Distribution of [hs/ls] (upper panels) and [Pb/hs] (lower panels) ratios in synthesised populations of intrinsically s -process enhanced post-AGB stars, calculated with different values of $^{13}\text{C}_{\text{eff}}$, as indicated over each panel. The grey scale is a logarithmic measure of the number distribution of stars over the plotted s -process index. The number density is weighed by the initial mass function and by the time each star spends in an abundance bin, and then normalised for each metallicity. The results are compared to the s -process element ratios observed in MACHO 47.2496.8, indicated by the crosses. The size of the vertical and horizontal lines indicate the observational errors of the data and the arrow indicates that the observed [Pb/hs] ratio is an upper limit.

two different constraints. A more promising explanation can be found by remembering that model predictions always produce too high $^{12}\text{C}/^{13}\text{C}$ ratios with respect to observations, both for red giant and AGB stars. Extra-mixing processes, also sometimes called “deep mixing” or cool bottom processing, that would enable envelope material to suffer proton captures, thus transforming ^{12}C into ^{13}C , have been invoked to explain, e.g., the low $^{12}\text{C}/^{13}\text{C}$ ratios observed in giant stars (Gilroy 1989) and in carbon stars (Abia et al. 2001), as well as in meteoritic silicon carbide grains from AGB stars (e.g. Zinner et al. 2006). We cannot rule out that such processes could also have affected the C composition of MACHO 47.2496.8. Recently, mixing instabilities have been found to occur in first giant branch stars because of a small inversion in the molecular gradient, just above the H-burning shell, where the $^3\text{He}(^3\text{He},2p)^4\text{He}$ reaction is activated (Eggleton et al. 2006; Charbonnel & Zahn 2007). This physical mechanism likely

leads to modifications of the CNO abundances, as observed, and also would be at work during the AGB phase (M. Cantiello, personal communication). Note that extra mixing on the red giant branch would not be enough to explain the $^{12}\text{C}/^{13}\text{C}$ ratio observed in MACHO 47.2496.8.

3.4 Conclusion

We have compared spectroscopic observations of the post-AGB star MACHO 47.2496.8 in the LMC to results obtained by carrying out stellar population synthesis coupled with s -process nucleosynthesis in order to obtain constraints on the physics of AGB stars. The result is that the values of the free parameters needed to match MACHO 47.2496.8 are consistent with the values we found in Paper I for Galactic s -process enhanced stars:

1. $\Delta M_c^{\text{min}} = -0.065M_\odot$,
2. $\lambda_{\text{min}} = 0.2$, and
3. $f_{^{13}\text{C,IS}} = 1/40$.
4. Objects with metallicity $[\text{Fe}/\text{H}] \lesssim -1$ are generally well reproduced by a lower value of $^{13}\text{C}_{\text{eff}}$ than objects with metallicity $[\text{Fe}/\text{H}] \gtrsim -1$.

The strong agreement among results for different populations and for stars in different galaxies reinforces our confidence in the findings of Paper I. Regarding point (4) above, for IRAS07134+1005 ($[\text{Fe}/\text{H}]=-1$) and HD 189711 ($[\text{Fe}/\text{H}]=-1.15$) we have to lower $^{13}\text{C}_{\text{eff}}$ by roughly a factor of 3, with respect to higher-metallicity objects, for MACHO 47.2496.8 ($[\text{Fe}/\text{H}]=-1.4$) we have to lower $^{13}\text{C}_{\text{eff}}$ by roughly a factor of 3 to 6, while for Pb stars ($[\text{Fe}/\text{H}]\lesssim -2$) we have to lower $^{13}\text{C}_{\text{eff}}$ by roughly a factor of 6 to 12. This trend requires for an explanation within AGB s -process models. We conclude that the heavy element chemical composition of the metal-poor LMC star MACHO 47.2496.8 is consistent with model predictions of an intrinsic s -process enhanced star, but that an extra-mixing process is needed to account for the carbon isotopic and C/O ratios. Future work will have to address the question of whether data from the still small but expanding set of observed extragalactic AGB stars (see e.g. de Laverny et al. 2006) can be fitted with our current choice of model parameters.

acknowledgements ML gratefully acknowledges the support of NWO through the VENI grant; MR acknowledges financial support from the Fund for Scientific Research - Flanders (Belgium).

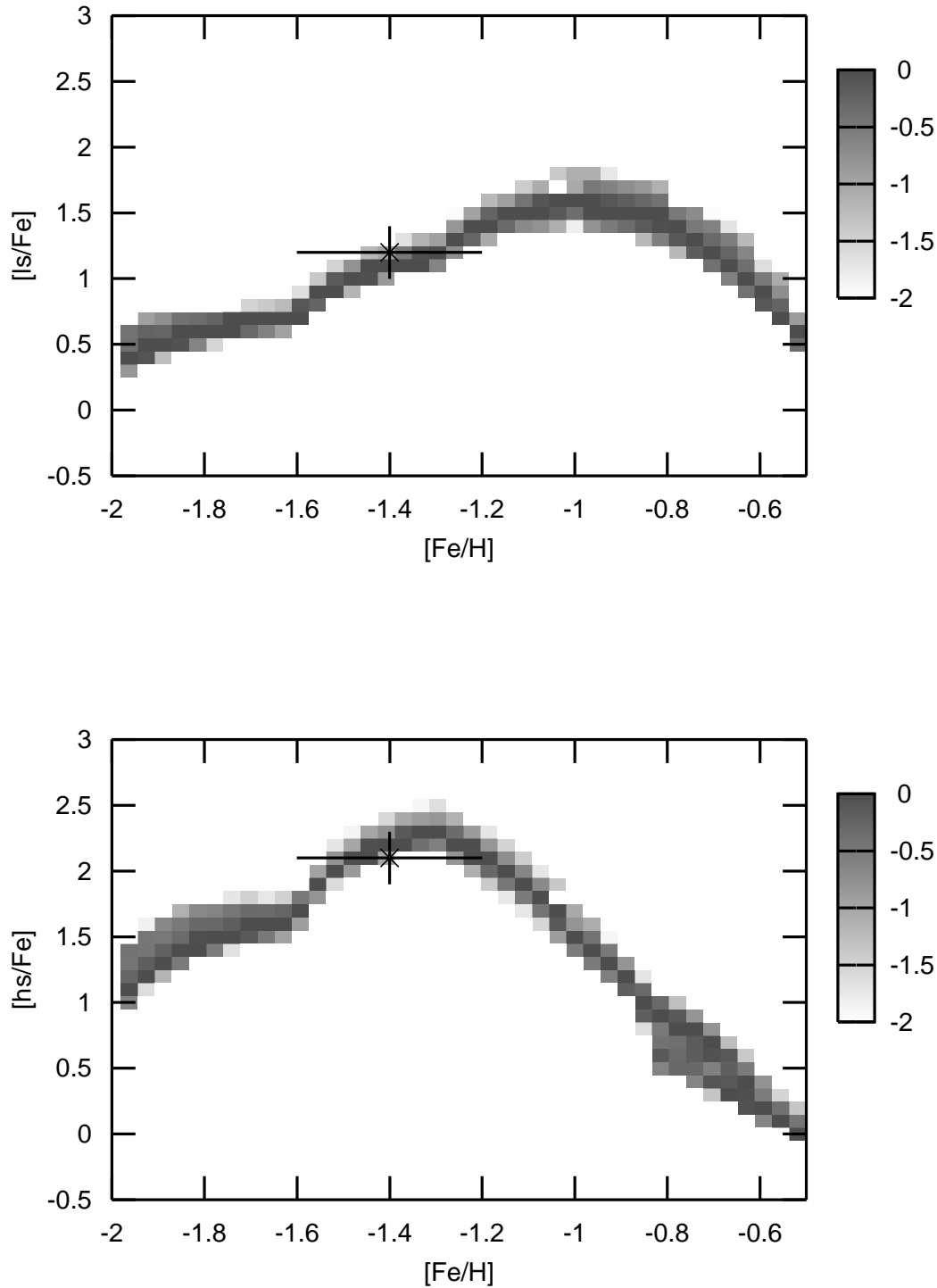


Figure 3.3: Distribution of $[ls/Fe]$ (upper panel) and $[hs/Fe]$ (lower panel) ratios in a synthetic population of intrinsically s -process enhanced post-AGB stars, calculated by assuming $^{13}C_{\text{eff}} = 1/3$. The grey scale is a logarithmic measure of the number distribution of stars over the plotted s -process index. The number density is weighed as described in the caption of Fig. 3.2. The results are compared to $[ls/Fe]$ and $[hs/Fe]$ ratios measured in MACHO 47.2496.8, indicated by the crosses. The size of the vertical and horizontal lines indicate the errors on the data measurements.

Part II

Eccentric binary systems with AGB stars

Chapter 4

Orbital eccentricities of binary systems with a former AGB star

A.A. Bonačić Marinović, E. Glebbeek, O.R. Pols,
Submitted on July 17, 2007, to Astronomy & Astrophysics

Abstract Many binary stellar systems in which the primary star is beyond the AGB evolutionary phase show significant orbital eccentricities whereas current binary interaction models predict their orbits to be circularised. In the search for a mechanism to counteract the circularising effect of tidal interaction we analyse how the orbital parameters in a system are modified under mass loss and mass exchange among its binary components. We propose a model for enhanced mass-loss from the AGB star due to tidal interaction with its companion, which allows a smooth transition between the wind and Roche-lobe overflow mass-loss regimes. We explicitly follow its effect along the orbit on the change of eccentricity and orbital semi-major axis, as well as the effect of accretion by the companion. We calculate timescales for the variation of these orbital parameters and compare them to the tidal circularisation timescale. We find that in many cases, due to the enhanced mass loss of the AGB component at orbital phases closer to the periastron, the net eccentricity growth rate in one orbit is comparable to the rate of tidal circularisation. We show that with this eccentricity enhancing mechanism it is possible to reproduce the orbital period and eccentricity of Sirius system, which under the standard assumptions of binary interaction is expected to be completely circularised. We also show that this mechanism may provide an explanation for the eccentricities of most barium star systems, which are expected to be circularised due to tidal By proposing a tidally enhanced model of mass loss from AGB stars we find a mechanism which efficiently works against the tidal circularisation of the orbit. This mechanism can explain the significant eccentricities observed in binary systems containing a white dwarf and a less evolved companion, which are predicted to be circularised due to their proximity, such as Sirius and systems with barium stars.

4.1 Introduction

Detached binary systems containing a white dwarf and a relatively unevolved companion, i.e., a main-sequence star or a (sub)giant, are a useful tool to understand the binary evolution of systems with an asymptotic giant branch (AGB) star, given that their orbital and chemical properties do not change significantly from the moment that the primary finished its AGB evolution and became the current white dwarf. An example of such a system is Sirius, a $2.1 M_{\odot}$ main sequence star with a $1.05 M_{\odot}$ white dwarf companion in a 50-year orbit. Under the standard picture of binary evolution with tidal interaction this system should have circularised when the primary became an AGB star, as we show in §4.4.1 of this paper. However, this system has an eccentricity $e = 0.59$ and is not an exception. A similar problem is faced when considering the barium-star systems, which are red giants with over-abundances of s -process elements (prominently barium) with white dwarf companions. These stars obtained their s -process enhancement by accreting mass from their companion when it was an AGB star. Due to the large size of AGB stars these systems are expected to be circularised by tidal interaction for periods smaller than about 3500-4000 days (Pols et al. 2003). However, barium-star systems with period as short as 600 days are observed to be significantly eccentric (Jorissen et al. 1998). The problems stated above are indications that a mechanism must exist that counteracts the circularising effect of the tides by the time primary star is on the AGB. Van Winckel et al. (1995) propose that enhanced mass loss at periastron could enhance the eccentricity and Soker (2000) shows that this works when the AGB star fills its Roche lobe during periastron passages. It has also been proposed that the tidal interaction between a binary system and a circumbinary disk could account for an eccentricity enhancing mechanism (Waelkens et al. 1996; Waters et al. 1998). However, Soker (2000) argues that the masses of observed circumbinary disks are too small to counteract the circularisation.

Mass loss of stars in binary systems is commonly treated as single-star wind mass-loss as long as the stars are inside their Roche lobes, while when one star fills its Roche lobe the mass-loss rate increases abruptly to the high values that correspond to Roche-lobe overflow. This approximation is fairly accurate for stars with a steep density gradient in their atmospheres, but it is not appropriate for the case of AGB stars, given their large atmospheric pressure scale height and their weakly bound envelope. The fact that AGB stars undergo dynamical pulsations further reduces density gradient in the layers above the photosphere Bowen (e.g., 1988). We propose a prescription for enhanced mass loss which smoothly grows from the single star wind mass loss rate to the Roche lobe overflow mass loss rate as the radius of the star approaches its Roche lobe radius. This gives a variable mass loss rate along eccentric orbits which is higher at orbital phases closer to the periastron, even if the star does not fill its Roche lobe. This effect works in the same way as discussed above, but no filling of the Roche lobe is needed, so that this effect is permanently competing against tidal circularisation.

Boffin & Jorissen (1988) carried out calculations of the variation of orbital parameters considering instantaneous mass transfer and only linear momentum conservation. Angular momentum conservation was not taken into account in this exploratory study. An extension including angular momentum conservation was made by Liu et al. (2000), but they make use

of the orbital average of the distance between the components and orbital angular velocity to carry out their calculations, which in the case of a variable mass-loss along the orbit does not give the correct results.

In §4.2 we revise the variation of orbital parameters due to stellar mass loss and mass transfer by taking into account the conservation laws of linear and angular momentum with respect to the centre of mass of the actual binary system. We do not make use of the orbital averages a priori, but give the variations as a function of the orbital phase, allowing different rates of mass loss and mass transfer along the orbit. In §4.3 we calculate the rate of change of the eccentricity according to different assumptions of mass loss and accretion. In §4.4 we evaluate the competition between the tidal circularisation and the eccentricity pumping due to our proposed mass loss, and show that the latter can prove effective in counteracting the former for systems such as Sirius and barium stars in which their AGB component did not fill its Roche lobe. A summary is presented in §4.5.

4.2 Variational analysis of orbital parameters due to wind mass transfer or mass loss

The dynamics of a binary orbit are well described by the two masses, M_1 and M_2 , its energy, E_{orb} , and its angular momentum, J_{orb} (e.g., Goldstein 1980). The fractional variation of the semi-major axis (also called the separation), a , and of the eccentricity, e , are expressed as

$$\frac{\delta a}{a} = \frac{\delta M}{M} + \frac{\delta m}{m} - \frac{\delta E_{\text{orb}}}{E_{\text{orb}}} \quad (4.1)$$

and

$$\frac{\delta(1-e^2)}{(1-e^2)} = 2\frac{\delta J_{\text{orb}}}{J_{\text{orb}}} + \frac{\delta E_{\text{orb}}}{E_{\text{orb}}} - 2\frac{\delta M}{M} - 3\frac{\delta m}{m}, \quad (4.2)$$

where we use the notation for the reduced mass problem, such that the total mass $M \equiv M_1 + M_2$ and the reduced mass $m \equiv \frac{M_1 M_2}{M_1 + M_2}$. For a detailed derivation of these expressions and those that follow in this section see Appendix B.

4.2.1 Angular momentum and energy

In a system where r is the instantaneous distance between the stars and ω is the instantaneous angular velocity of the components with respect to a co-moving inertial frame with its origin in the centre of mass (from here on the CM frame), the fractional variations of orbital angular momentum and energy are given by

$$\begin{aligned} \frac{\delta J_{\text{orb}}}{J_{\text{orb}}} &= \frac{\delta m}{m} + 2\frac{\delta r}{r} + \frac{\delta \omega}{\omega} \\ &= \frac{\delta m}{m} + \frac{\delta r}{r} + \frac{\delta v_{\theta}}{v_{\theta}} \end{aligned} \quad (4.3)$$

and

$$\frac{\delta E_{\text{orb}}}{E_{\text{orb}}} = \frac{\delta m}{m} + \frac{2a}{r} \frac{\delta M}{M} - \frac{2a}{r} \frac{\delta r}{r} - \frac{a}{GM} [2v_r \delta v_r + 2v_\theta \delta v_\theta] \quad (4.4)$$

respectively. We denote the velocity of one star relative to its companion by $\vec{v} = \vec{v}_1 - \vec{v}_2$, where \vec{v}_i is the velocity of star i with respect to the CM. \vec{v} also corresponds to the orbital velocity in the reduced mass problem. We also use the subscripts r and θ to indicate the radial and transverse velocity components respectively.

We consider a system in which both stars may lose mass in isotropic winds, part of which may be accreted by the companion such that during a time interval δt an amount of mass $\delta M_{1,W}$ is lost by star 1 and an amount $\delta M_{2,ACC}$ is accreted by star 2. In this way an amount of mass $\delta M_{1,LOST} = \delta M_{1,W} - \delta M_{2,ACC}$ is effectively lost by star 2 from the system. To determine how the orbital velocity components vary we assume that star 2 receives an impulse when it accretes an amount of mass $\delta M_{2,ACC}$ coming from the wind of star 1, which at the moment it is accreted has a velocity w_{12} in the CM frame. The corresponding expressions for mass lost from star 2 are obtained by interchanging the indices 1 and 2. This yields the variations

$$\delta v_r = [w_{r,12} - v_{r,2}] \frac{\delta M_{2,ACC}}{M_2} + (1 \Leftrightarrow 2), \quad (4.5)$$

and

$$\delta v_\theta = [w_{\theta,21} - r_2 \omega] \frac{\delta M_{2,ACC}}{M_2} + (1 \Leftrightarrow 2) \quad (4.6)$$

where r_i corresponds to the distances of star i to the CM. The notation $+(1 \Leftrightarrow 2)$ used here and below means: add terms to the left again with indices 1 and 2 interchanged. For quantities defined with an index in the left-hand side of the equation it is implicit that the corresponding expression for the other star is obtained by exchanging the indices in the right-hand side. By means of Eqs. (4.3), (4.4), (4.5) and (4.6) we can now write the orbital angular momentum and energy variations as

$$\begin{aligned} \frac{\delta J_{\text{orb}}}{J_{\text{orb}}} = & - \frac{\delta M_{1,LOST}}{M_1} \left(\frac{M_2}{M} \right) \\ & + \frac{\delta M_{2,ACC}}{M_2} \left(1 - \frac{M_2}{M_1} + \frac{w_{\theta\text{rel},2}}{r\omega} \right) + (1 \Leftrightarrow 2) \end{aligned} \quad (4.7)$$

and

$$\begin{aligned} \frac{\delta E_{\text{orb}}}{E_{\text{orb}}} = & - \frac{\delta M_{1,LOST}}{M_1} \left[1 + \left(\frac{2a}{r} - 1 \right) \frac{M_1}{M} \right] \\ & + \frac{\delta M_{2,ACC}}{M_2} \left[1 - \frac{M_2}{M_1} - \frac{2a}{GM} \vec{v} \cdot w_{\text{rel},2} \right] + (1 \Leftrightarrow 2). \end{aligned} \quad (4.8)$$

In these equations $w_{\text{rel},2} \equiv (w_{12} - v_2)$ is the relative velocity of the wind with respect to star 2 when accreted. We have also used the fact that there must be no displacements δr_i , which implies that $\delta r/r = 0$ (see Appendix B for details).

4.2.2 Behaviour of the wind

To apply these expressions in calculations of orbital evolution, the detailed behaviour of the wind as it travels through the system must be followed from its point of origin until it is accreted or escapes the binary potential well. In general this requires either ballistic calculations (e.g., Brookshaw & Tavani 1993) or full-scale hydrodynamical calculations (e.g., Theuns et al. 1996; Nagae et al. 2004). For the purpose of this paper we assume the simple model described below.

The velocity of the wind from star j when it is accreted by star i has a radial component, $w_{r,ji}$, that we will assume to be the velocity of the wind emanating isotropically from star j as if it were a single star, w_j . For the transverse component, $w_{\theta,ji}$, we assume that the specific angular momentum of the wind with respect to the CM is conserved and we express it as $h_{W,j} \equiv \chi_j r_j^2 \omega$. Note that the wind carries both the orbital and spin angular momentum of the mass-losing star. With the above definition $\chi_j = 1$ represents a point mass star, given that such an idealised object can only carry orbital angular momentum and no intrinsic spin. Once the wind is accreted by the companion star i a fraction μ_i of $h_{W,j}$ is transferred to the spin angular momentum of the accretor and the rest is transferred to the orbit. Thus $w_{\theta,ji} = \xi_j \frac{M_i^2}{M^2} \frac{h_{\text{orb}}}{r_i}$, where h_{orb} is the orbital specific angular momentum given by $h_{\text{orb}}^2 = r^4 \omega^2 = GMa(1 - e^2)$ and $\xi_1 \equiv \chi_1(1 - \mu_2)$, which yields

$$(w_{\theta,12} - r_2 \omega) = r \omega \left(\frac{\xi_1 M_2^2 - M_1^2}{M_1 M} \right), \quad (4.9)$$

and similar for $w_{\theta,21} - r_1 \omega$.

4.3 Rate of eccentricity change

More useful than arbitrary variations of the physical parameters are their rates of change in time, thus from this point on we will transform $\delta \rightarrow d/dt$. The distance and orbital velocity components are

$$\begin{aligned} \frac{a}{r} &= \frac{1 + e \cos \theta}{1 - e^2}, \\ v_r &= \sqrt{\frac{G(M_1 + M_2)}{a(1 - e^2)}} e \sin \theta \quad \text{and} \\ v_t &= \sqrt{\frac{G(M_1 + M_2)}{a(1 - e^2)}} (1 + e \cos \theta), \end{aligned} \quad (4.10)$$

where θ is the orbital phase angle measured from the periastron. It is clear from its dependence on the orbital phase-angle that \dot{e} is not constant along the orbit. This is true for constant mass

loss and accretion rates, but especially if mass loss and accretion rates also depend on the orbital phase-angle. Employing the results we have derived so far we calculate using Eq. (4.2)

$$\begin{aligned} \dot{e} = & \frac{\dot{M}_{1,\text{LOST}}(\theta)}{M} \left\{ e + \cos \theta \right\} \\ & + \frac{\dot{M}_{2,\text{ACC}}(\theta)}{M_2} \left\{ \frac{M_1}{M} \left[\left(\frac{\xi_1 M_2^2}{M_1^2} - 1 \right) (2 \cos \theta + e + e \cos^2 \theta) \right. \right. \\ & \left. \left. - e \sin^2 \theta \right] + w_1 \sqrt{\frac{a(1-e^2)}{GM}} \sin \theta \right\} + (1 \Leftrightarrow 2). \end{aligned} \quad (4.11)$$

We note that the first term only depends on the assumption of isotropic mass loss and it is the same as given by Soker (2000) (see also Eggleton 2006). It shows that the eccentricity can increase if the mass-loss rate is higher near periastron than near apastron. The second term also depends on the additional assumptions about the wind behaviour (see §4.2.2). These are complicated expressions that must be followed along the orbit if they are to have a useful meaning. The orbital period is given by $P = 2\pi \sqrt{\frac{a^3}{G(M_1+M_2)}}$ and by defining the orbital average of a parameter A as $\langle A \rangle \equiv \frac{1}{P} \int_0^P A dt = \frac{1}{P} \int_0^{2\pi} A \frac{dt}{d\theta} d\theta$ we compute the net rate of change of a and e in one orbital period. When an orbital average is applied to Eq. (4.11) we obtain an expression which depends on $\langle \dot{M}_{i,\text{LOST}} \rangle$, $\langle \dot{M}_{i,\text{LOST}} \cos \theta \rangle$, $\langle \dot{M}_{i,\text{ACC}} \rangle$, $\langle \dot{M}_{i,\text{ACC}} \cos \theta \rangle$, $\langle \dot{M}_{i,\text{ACC}} \sin \theta \rangle$, $\langle \dot{M}_{i,\text{ACC}} \cos^2 \theta \rangle$ and $\langle \dot{M}_{i,\text{ACC}} \sin^2 \theta \rangle$ for $i = 1, 2$. These averages can be calculated only after $\dot{M}_{i,\text{LOST}}(\theta)$ and $\dot{M}_{i,\text{ACC}}(\theta)$ are known.

4.3.1 Constant wind and constant mass accretion

Usually the simplest case is assumed which corresponds to when $\dot{M}_{i,\text{ACC}} = \langle \dot{M}_{i,\text{ACC}}(\theta) \rangle$ and $\dot{M}_{i,\text{LOST}} = \langle \dot{M}_{i,\text{LOST}}(\theta) \rangle$ are constant along the orbit (e.g., Hurley et al. 2002). This yields

$$\frac{\langle \dot{e} \rangle}{e} = - \frac{\dot{M}_{2,\text{ACC}}}{M_2} \left(\frac{(1 - \sqrt{1-e^2})(1-e^2)\xi_1 M_2^2}{e^2 M_1 M} \right) + (1 \Leftrightarrow 2). \quad (4.12)$$

Clearly with the assumptions about the wind made here the eccentricity can only decrease, therefore if this effect is comparable to that of tidal friction it will only help to circularise the orbit on a faster timescale, otherwise it can be neglected (Hurley et al. 2002¹).

4.3.2 Accretion from a fast isotropic wind

We model the mass accretion with the Bondi & Hoyle (1944) mechanism, in which

$$\dot{M}_{2,\text{ACC}}(\theta) = \alpha \frac{(GM_2)^2 \dot{M}_{1,W}}{r_A^2 w_{\text{rel},2}^3 w_1}, \quad (4.13)$$

¹Hurley et al. (2002) have a different expression for \dot{e}/e due to different assumptions made in their calculations, however, their expression and ours are of the same order of magnitude.

where $\dot{M}_{1,W}$ is the wind mass loss rate from star 1, r_A the distance to the source of the wind at the moment it was emitted and α is a numerical factor which parameterises the efficiency of the accretion mechanism. In the case of a steady isotropic wind much faster than the orbital motion the transverse component of the wind velocity can be neglected, therefore one can safely assume that $w_{\text{rel},2} = w_1$ and $r_A = r$. Then the accretion rate $\dot{M}_{2,\text{ACC}}(\theta) = \dot{M}_{2,0 \text{ ACC}}(1 + e \cos \theta)^2$, where $\dot{M}_{2,0 \text{ ACC}} = \frac{\langle \dot{M}_{2,\text{ACC}}(\theta) \rangle}{\langle (1 + e \cos \theta)^2 \rangle}$. The mass from star 1 which is lost from the system is given by $\dot{M}_{1,\text{LOST}} = \dot{M}_{1,W} - \dot{M}_{2,\text{ACC}}$. With this assumption the averaged rate of change of e is

$$\frac{\langle \dot{e} \rangle}{e} = \frac{\dot{M}_{2,0 \text{ ACC}}}{M_2} \times \frac{(1 - e^2)^{3/2}}{2M_1(M_1 + M_2)} \left(3\xi_j M_2^2 - 2M_1(M_2 + 2M_1) \right) + (1 \Leftrightarrow 2). \quad (4.14)$$

In contrast to Eq.(4.12), where e always decreases with time, Eq.(4.14) shows that the eccentricity will increase if $M_2/M_1 > (1 + \sqrt{1 + 12\xi_1})/3\xi_1$ (e.g., $M_1 \lesssim 0.65M_2$ for the case of point masses, where $\xi_1 = 1$).

4.3.3 Accretion from the slow wind of an AGB star

The case of an AGB star with an accreting companion is somewhat different from the two cases we have already reviewed. The velocity of the wind from an AGB star is of the order of the stellar escape velocity, which is also of the order of the orbital velocity, if the size of the AGB star is a significant fraction of its Roche lobe. This implies that $w_1 \sim \sqrt{\frac{GM}{a(1-e^2)}}$, so the transverse velocity of the wind cannot be neglected as in the fast-wind case. Thus, making use of Eqs. (4.9) and (4.10) we write

$$w_{\text{rel},2}^2(\theta) = \left(\frac{GM}{a(1-e^2)} \right) \times \left[\left(\frac{w_1}{\sqrt{\frac{GM}{a(1-e^2)}}} - \frac{M_1 e \sin \theta}{M} \right)^2 + \left(\frac{[\xi_1 M_2^2 - M_1^2](1 + e \cos \theta)}{M_1 M} \right)^2 \right] \quad (4.15)$$

and by means of Eq. (4.13) we express the accretion rate as

$$\dot{M}_{2,\text{ACC}}(\theta) = \frac{\dot{M}_{2,0 \text{ ACC}}(1 + e \cos \theta)^2}{\left[\left(\frac{w_1}{\sqrt{\frac{GM}{a(1-e^2)}}} - \frac{M_1 e \sin \theta}{M} \right)^2 + \left(\frac{[\xi_1 M_2^2 - M_1^2](1 + e \cos \theta)}{M_1 M} \right)^2 \right]^{3/2}}, \quad (4.16)$$

where $\dot{M}_{2,0 \text{ ACC}} = \left(\frac{GM}{a(1-e^2)} \right)^{3/2} \langle \dot{M}_{2,\text{ACC}}(\theta) \rangle \left\langle \frac{w_{\text{rel},2}^3(\theta)}{(1 + e \cos \theta)^2} \right\rangle$ in this case. The orbital average can be only calculated numerically, but we find that when $w_1 \gtrsim 3 \sqrt{\frac{GM}{a(1-e^2)}}$ the result of the integration

is well approximated by the fast-wind assumption. The fact that the orbital phase can change significantly between the moment the wind was emitted and when it is accreted also introduces a phase angle shift in the relation between $\dot{M}_{2,\text{ACC}}$ and $\dot{M}_{1,\text{W}}$. However, we performed numerical calculations of $\langle \dot{e} \rangle / e$ by applying different phase angle shifts in Eq. (4.13) and the results do not differ by more than 15% from the zero phase-angle case.

4.3.4 Mass loss from an AGB star

A non-AGB star has a steep density gradient in its photospheric layers, i.e., it has a well defined radius. When the star is smaller than its Roche lobe it loses mass in the form of a wind which may be enhanced by the presence of the companion (e.g., Tout & Eggleton 1988). If such a star becomes larger than its Roche lobe then the mass loss rate is abruptly enhanced by orders of magnitude, governed by the Roche lobe overflow mechanism. Thus there is an almost discontinuous transition from one regime to the other and they can be treated as separate cases. AGB stars, on the other hand, have a shallow surface density gradient (e.g., Bowen 1988; Pastetter & Ritter 1989) and therefore the transition between the wind and the Roche lobe overflow mass-loss regimes is smooth. Karovska et al. (2005) made observations in X-rays of the symbiotic binary system Mira which show the AGB star is surrounded by material in the shape of a lobe as predicted by the Roche model, suggesting that the star is undergoing a transitional form of mass loss that can be described as wind Roche-lobe overflow. This provides support to the idea that the extended and weakly-bound atmosphere of an AGB star can be highly influenced by the tidal force exerted by the companion. Frankowski & Tylenda (2001) computed the enhancement of the wind mass-loss rate of giant stars in binary systems through the effect of the Roche potential on the local surface temperature and gravity. They find that the mass-loss enhancement depends on $(R_\star/R_L)^3$, where R_\star and R_L are radius of the AGB star and its Roche-lobe radius, respectively. However, the overall effect is modest, less than a factor of 2, unless R_\star is very close to R_L . Their model does not account for the wind Roche-lobe overflow transition expected for AGB stars and suggested by the observations of Mira. Tout & Eggleton (1988) propose that the mass-loss rate of cool giants is enhanced by the presence of a companion, driven by the tidal friction torque. Thus, in their heuristic model the mass-loss enhancement depends on the sixth power of the R_\star/R_L ratio. Building on this idea, we propose the following AGB star mass-loss model, which provides a smooth transition between the single-star wind mass-loss rate, $\dot{M}_{\star,\text{w}}$, and the Roche-lobe overflow mass-loss rate, \dot{M}_{RLOF} :

$$\dot{M}_\star = \dot{M}_{\star,\text{w}} \left[1 + \left(\frac{\dot{M}_{\text{RLOF}}}{\dot{M}_{\star,\text{w}}} - 1 \right) \left(\frac{R_\star}{R_L} \right)^6 \right]. \quad (4.17)$$

For eccentric orbits the Roche geometry does not apply so we utilise an *instantaneous* Roche-lobe which depends on the actual distance between the stars, r , as

$$R_L(\theta) = \frac{a(1-e^2)}{(1+e\cos\theta)} f(q_\star), \quad (4.18)$$

where q_\star is the mass ratio of the AGB star to its companion and $f(q) = \frac{0.49q^{2/3}}{0.6q^{2/3} + \ln(1+q^{1/3})}$, following the approximation of Eggleton (1983). With this prescription the mass loss rate along the orbit is not constant, but enhanced when the system is at orbital phases close to the periastron. Thus, if the AGB star does not fill its Roche lobe in the periastron and there is no mass transfer ($\dot{M}_{i,0 \text{ ACC}} = 0$), the net contribution in one orbital period to the eccentricity variation rate is

$$\frac{\langle \dot{e} \rangle}{e} = \frac{\dot{M}_{\text{RLOF}} - \dot{M}_{\star, \text{W}}}{M} \left(\frac{R_\star}{af(q_\star)} \right)^6 \frac{3(8 + 12e^2 + e^4)}{8(1 - e^2)^{9/2}}. \quad (4.19)$$

Eq. (4.19) will always contribute to enhance the eccentricity, given that \dot{M}_{RLOF} is larger than $\dot{M}_{\text{AGB,W}}$. The effect of mass transfer to the companion will in many cases act against the eccentricity enhancement, but its contribution to Eq. (4.19) cannot be expressed analytically and it has to be calculated numerically (see §4.3.2 and §4.3.3). However, it becomes significant only when a considerable amount of mass lost from the AGB star is transferred.

4.4 Comparison of timescales

In this section we calculate and compare the timescales on which the effects of circularisation and eccentricity enhancement will take place, τ_{circ} and τ_e respectively. Hurley et al. (2002) give the following expression for the tidal evolution of e due to convective damping by combining the results of Zahn (1977, see also Zahn & Bouchet 1989) and Hut (1981):

$$\frac{1}{\tau_{\text{circ}}} \equiv -\frac{\dot{e}}{e} = \frac{18}{7} \frac{f_{\text{conv}}}{\tau_{\text{conv}}} \frac{M_{\text{env}}}{M_\star} \frac{(1 + q_\star)}{q_\star^2 (1 - e^2)^{13/2}} \left(\frac{R_\star}{a} \right)^8 \times \left[f_3(e^2) - \frac{11}{18} (1 - e^2)^{3/2} f_4(e^2) \frac{\Omega_{\star, s}}{n} \right], \quad (4.20)$$

where M_{env} is the envelope mass of the AGB star and τ_{conv} is the convective turnover timescale. A good approximation to the depth of the convective zone in an AGB star is its radius, thus by employing Eq. (31) from Hurley et al. (2002) we obtain $\tau_{\text{conv}} = 0.2351 (M_{\text{env}} R_\star^2 / L_\star)^{1/3} \text{yr}$, with L_\star the luminosity of the star and the parameters expressed in solar units. $\Omega_{\star, s}/n$ is the ratio of spin angular rotation rate of the AGB star, $\Omega_{\star, s}$, to the average orbital angular velocity, n . The functions $f_x(e^2)$ are those derived by Hut (1981) and the numerical factor $f_{\text{conv}} = f' \min(1, (P_{\text{tid}}/2\tau_{\text{conv}})^2)$ is from Rasio et al. (1996), where $P_{\text{tid}}^{-1} = |n - \Omega_{\star, s}|/2\pi$. Verbunt & Phinney (1995) found from an analysis of observed red-giant binaries that $f' \approx 1$, however, this value may be different for the case of AGB stars. It is important to note that this calculation of τ_{circ} gives a stronger circularising effect for orbits with finite eccentricity values than the usually employed prescription by Zahn (1977) which assumes an almost circular orbit (e.g., Rasio et al. 1996; Soker 2000).

We estimate the Roche-lobe overflow mass-loss rate \dot{M}_{RLOF} following the prescription of

Ritter (1988, see also Meyer & Meyer-Hofmeister 1983; Pastetter & Ritter 1989), where

$$\dot{M}_{\text{RLOF}} = \frac{2\pi}{\sqrt{e}} \left(\frac{k_{\text{B}}}{m_{\text{H}}\mu_{\star}} T_{\star} \right)^{3/2} \frac{R_{\star}^3}{GM_{\star}} \rho_{\star,\text{ph}} F(q_{\star}^{-1}), \quad (4.21)$$

with $F(x) = 1.23 + 0.5 \log x$. The photospheric density of the AGB star is given by (Kippenhahn & Weigert 1990; Soker 2006)

$$\rho_{\star,\text{ph}} = \frac{2}{3} \frac{m_{\text{H}}\mu_{\star}}{k_{\text{B}}} \frac{GM_{\star}}{R_{\star}^2 \kappa_{\star} T_{\star}}, \quad (4.22)$$

where κ_{\star} is the opacity of the envelope of the AGB star, T_{\star} is the effective temperature and m_{H} and k_{B} are the mass of the hydrogen atom and the Boltzmann constant respectively. A typical 1.5-2.5 M_{\odot} AGB star has a surface temperature of about 3300K, a radius of about 300 R_{\odot} and a luminosity of about 10000 L_{\odot} . According to the envelope opacity calculations of Marigo (2002), the corresponding opacity at this temperature is approximately $\kappa_{\star} = 2.5 \times 10^{-4} \text{ cm}^2 \text{ g}^{-1}$ for densities of the order of $10^{-13} - 10^{-11} \text{ g cm}^{-3}$, which is the expected range of AGB surface densities. Employing this value of κ_{\star} and the luminosity, radius and mass mentioned above, the prescription of Eq. (4.21) yields $\dot{M}_{\text{RLOF}} \sim 10^{-3} M_{\odot} \text{ yr}^{-1}$. This is about 10000-30000 times larger than the single-star wind mass-loss rate of our typical star at the beginning of the AGB lifetime, calculated with the prescription of Vassiliadis & Wood (1993). By the end of the AGB phase, at the onset of the superwind phase, \dot{M}_{RLOF} is still 50-200 times larger than the wind mass-loss rate.

4.4.1 Eccentricity of the Sirius system

Sirius A, a main sequence star of 2.1 M_{\odot} , and Sirius B, a white dwarf of 1.05 M_{\odot} (Gatewood & Gatewood 1978), form a binary system with period $P = 50.1$ yr and eccentricity $e = 0.59$ (van den Bos 1960). Given the semi-major axis of the orbit, $a = 20$ AU, and the high eccentricity of this system, the distance between its components at periastron is about 1700 R_{\odot} . By the time the primary star (initially a star of about 5.5-6 M_{\odot}) was in the AGB phase its radius was so large ($R \approx 750 R_{\odot}$) that it could have filled its Roche lobe during periastron passages. Whether or not the Roche lobe was filled, a strong tidal interaction must have occurred due to the proximity of the system components. We have tracked the evolution of binary systems which evolve into a main sequence star with the mass of Sirius A and a white dwarf with the mass of Sirius B, which from here on we will call Sirius-like systems. To compute the binary evolution models we employed a version of the rapid synthetic code of binary evolution of Izzard et al. (2006), which makes use of modifications described in Chapter 2. The code employs Eq. 4.20 to model the effect of circularisation. The set of initial conditions for the models consists of the following:

- A primary with initial mass of 5.7 M_{\odot} , which ends its life as a white dwarf similar to Sirius B, independently of the choice of mass loss.

- 2 initial secondary masses (2.00 and $2.05 M_{\odot}$) which yield a star similar to Sirius A.
- 25 initial separations, a_i , logarithmically separated between 10 AU and 500 AU.
- 25 initial eccentricities, separated linearly between 0.5 and 0.99.
- Solar metallicity, $Z = 0.02$.

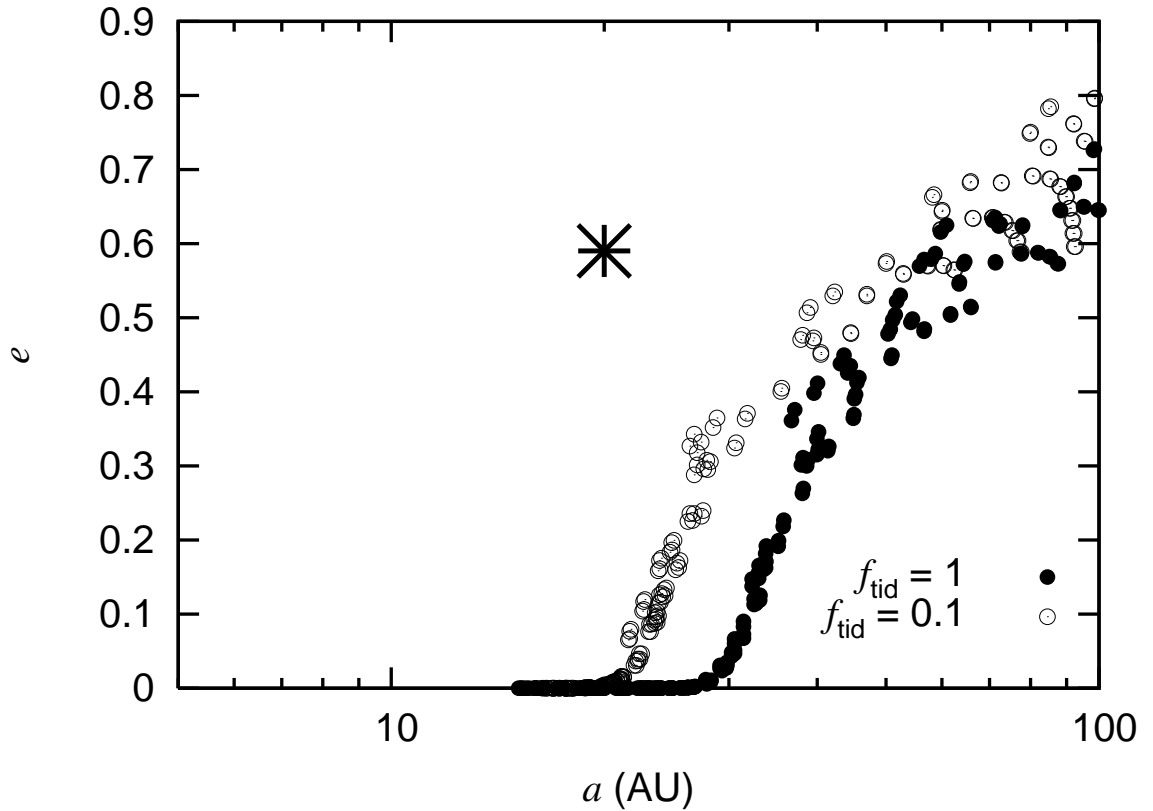


Figure 4.1: Computed eccentricity of Sirius-like binary models without any eccentricity-enhancing mechanism as function of their separation, assuming the standard binary interaction. The filled circles indicate the orbital parameters of Sirius-like systems computed by assuming a tidal dissipation factor $f' = 1$. The open circles are similar, but assuming that the tidal dissipation is ten times weaker. The star indicates the observed orbital parameters of the Sirius system, which has a notably higher eccentricity than what standard models predict for its separation, even with substantially reduced tidal friction.

In the standard scenario of tidal dissipation with constant mass loss along the orbit the eccentricity will always decrease. Fig. 4.1 shows the distribution of the synthetic Sirius-like systems in the e - P plane compared to the observed position of the Sirius system in this plane. The solid circles indicate the orbital properties of Sirius-like systems when assuming $f' = 1$, which show that the standard scenario of tidal interaction in binary evolution predicts complete circularisation for systems separated up to about 30 AU. The closest system with

an eccentricity of 0.59 has a separation of about 55 AU. The open circles show the orbital parameters predicted for Sirius-like systems when the strength of tidal dissipation is reduced to $f' = 0.1$. The results are still far from reproducing the observed Sirius system. A separation of at least about 40 AU is required to obtain the observed eccentricity of 0.59. To reproduce the eccentricity and separation of Sirius within this scenario a tidal dissipation factor $f' < 10^{-3}$ is needed, which is too strong a reduction to be acceptable. This demonstrates that the standard scenario of binary evolution cannot explain the observed eccentricity of the Sirius system, because it predicts that the system should be circularised.

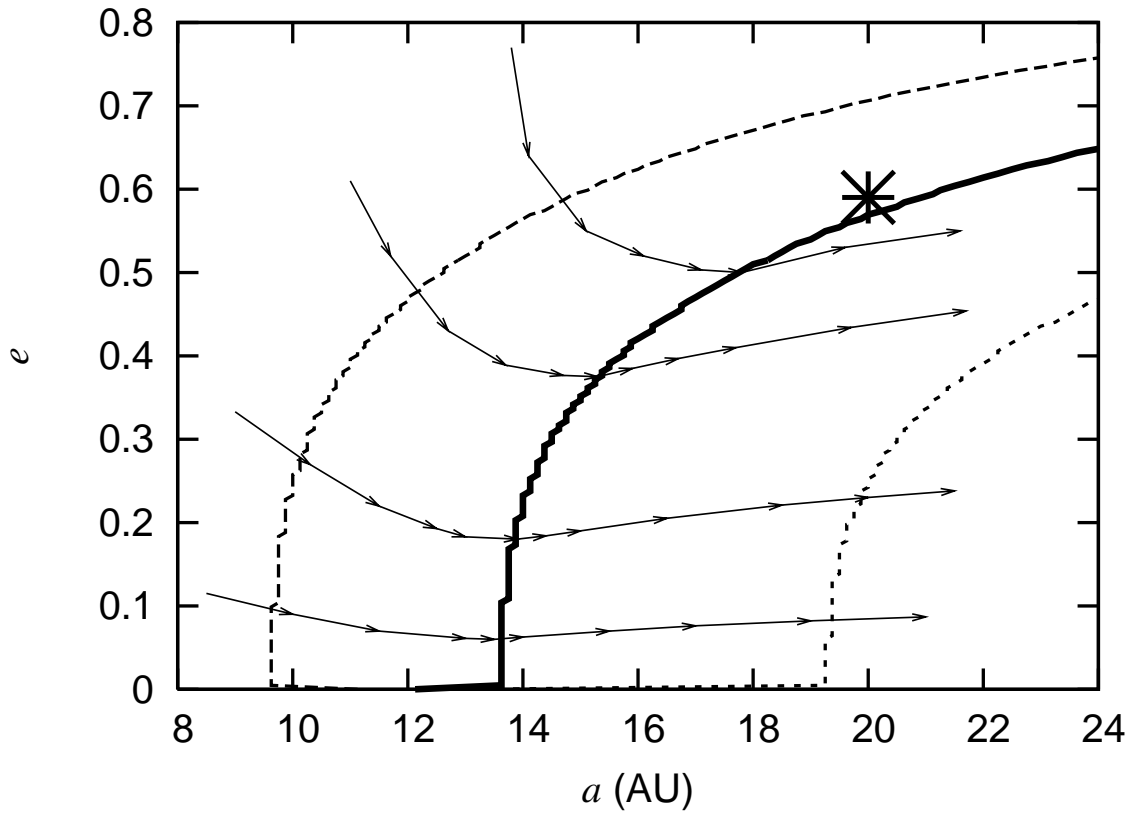


Figure 4.2: Behaviour of eccentricity of a binary system with a $4.5M_{\odot}$ AGB primary (initially a $5.5M_{\odot}$ star) and a $2.1M_{\odot}$ MS secondary as the system widens due to mass loss. The thick solid line indicates $\tau_e = \tau_{\text{circ}}$ when f' is assumed to be 0.5 and 5% of the mass lost via the enhanced mass-loss mechanism is accreted by the companion. The arrows indicate instantaneous directions in the diagram which a binary system will follow as it evolves. The star represents the current position in the $e - a$ plane of the Sirius system. The thin dashed and dotted lines also indicate $\tau_e = \tau_{\text{circ}}$, but considering $f' = 0.25$ and $f' = 1$, respectively.

However, this is not the case if the tidally enhanced mass-loss we propose in Eq. (4.17) is considered. Due to its variable mass loss along the orbit an eccentricity enhancing effect counteracts the tidal circularisation. We compare τ_e and τ_{circ} to see which effect is dominant. We estimate their values at the moment of evolution when the tidal dissipation effects are

strongest, which is the bottleneck for ending up with an eccentric orbit. This occurs when the AGB star reaches its maximum radius, $700 R_{\odot}$, at which point it has a luminosity of $38000 L_{\odot}$ and a core and envelope mass of $1.0 M_{\odot}$ and $3.5 M_{\odot}$ respectively. For the calculation of the Roche-lobe overflow mass-loss rate we assume $\kappa_{\star} = 10^{-4}$, which approximates the values calculated by Marigo (2002) for the envelope opacity of high-metallicity stars with a temperature of about 3000 K. This gives $\dot{M}_{\text{RLOF}} = 1.944 \times 10^{-3} M_{\odot} \text{ yr}^{-1}$ according to Eq. 4.21, while the wind mass-loss rate at this point is $\dot{M}_{\star, \text{W}} = 5.168 \times 10^{-5} M_{\odot} \text{ yr}^{-1}$. Fig. 4.2 shows how the $e - a$ plane is divided into a region where the eccentricity decreases (upper-left area) and a region where the eccentricity is enhanced (lower-right area). As mass is lost from the system, the separation increases. Thus, if we adopt a modest reduction of the tidal dissipation strength ($f' = 0.5$), any system with a separation larger than about 14 AU will eventually cross to the eccentricity-enhancing region, avoiding a circular orbit by the end of the AGB phase. In particular, the orbit of a system with orbital parameters similar to Sirius will remain eccentric. The thin dotted and dashed lines in Fig. 4.2 show that the location of the

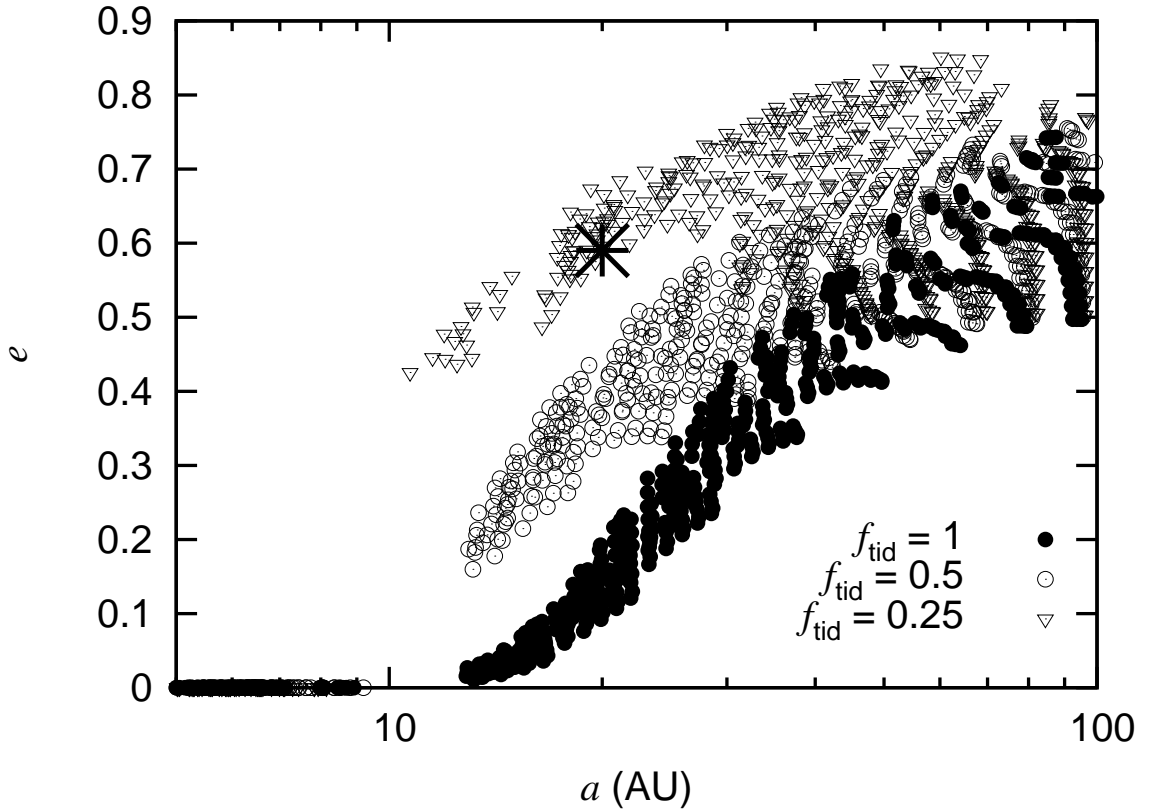


Figure 4.3: Computed eccentricity of Sirius-like binary models which take into account our proposed eccentricity enhancing mechanism plotted as function of their separation. The filled circles indicate the orbital parameters of Sirius-like systems computed by assuming a tidal dissipation factor $f' = 1$. The open circles and triangles indicate the results for similar calculations, but assuming that the tidal dissipation factor f' is 0.5 and 0.25, respectively. The star indicates the observed orbital parameters of the Sirius system, which are well reproduced if $f' = 0.25$ is assumed.

dividing line between decreasing and increasing eccentricity is sensitive to the tidal strength factor f' . This is because the ratio of timescales $\tau_e/\tau_{\text{circ}}$ only varies as $(R_\star/a)^2$, i.e., a much weaker dependence than either of the individual timescales. There is a similar sensitivity to the adopted average opacity κ_\star through \dot{M}_{RLOF} , which is also not certain, given that Eq. 4.21 is only approximate. Given these uncertainties, the results are not definitive. However, we have shown that by adopting reasonable values for the uncertain parameters the orbit of Sirius can be kept significantly eccentric. Finally we note that the results are insensitive to the amount of mass accreted by the companion, as long as this is less than about 10-15% of the mass lost by the AGB star.

So far we have shown how our eccentricity-enhancing mechanism works by employing values of single-star models for the AGB primary at a given moment of evolution. However, the overall effect on the orbit of a given binary depends on how the relevant parameters change as a function of time as the binary evolves from zero age to its current state. We have therefore implemented the orbital evolution formulae derived in Sect. 4.3 into the synthetic binary evolution code of Izzard et al. (2006), including our enhanced mass-loss prescription. Full details of this implementation are given in Chapter 5. We calculate models for the same set of initial conditions as described above, assuming that 5% of the enhanced mass loss $(\dot{M}_\star - \dot{M}_{\star,w})$ is accreted by the companion. Fig. 4.3 shows a comparison of the synthetic Sirius-like systems resulting from these models to the observed orbital properties of Sirius. The filled circles show the eccentricity and separation predicted by models which assume the standard tidal dissipation, $f' = 1$. Compared to the case when only tidal dissipation is considered (Fig. 4.1), the resulting binaries are significantly more eccentric in the separation range 15-40 AU, and the effect is comparable to reducing the tidal strength to $f' = 0.1$ in Fig. 4.1. The triangles in Fig. 4.3 show that to reproduce the orbital properties of Sirius the tidal dissipation has to be weakened by only a factor of 4, which is still within a range of reasonable values, as opposed to a reduction by more than a factor 1000 needed when only tidal circularisation is include.

4.4.2 Eccentricities of the barium stars

Barium stars show over-abundances of s -process elements, most prominently of barium, and are found in binary systems with white dwarf companions. This constitutes evidence for mass accretion from their companions when the latter were asymptotic giant branch (AGB) stars, given that s -process elements are synthesised in the AGB phase of evolution. Barium star binary systems are observed to have periods between 80 and 10000 days and most of the systems with periods larger than about 600 days are significantly eccentric (see Fig. 4.4). These systems pose a problem to the standard binary evolution scenario which predicts that orbits with periods shorter than about 3500-4000 days should have been circularised due to the tidal dissipation that must have taken place when the primary was an AGB star (e.g., Pols et al. 2003). The eccentricity enhancement resulting from our proposed AGB mass loss provides a mechanism which can effectively compete with tidal circularisation. We calculate the relevant timescales for a binary system with a $1.5 M_\odot$ AGB primary and a $1.1 M_\odot$ secondary, with

metallicity $Z = 0.008$, and assume that 10% of the mass lost by the AGB star is accreted by the companion. The calculations are made at the AGB stage of evolution where the tidal dissipation is strongest (the circularisation bottleneck), where the radius of the AGB star is $280 R_{\odot}$, its luminosity is $7500 L_{\odot}$ and its core and envelope masses are $0.64 M_{\odot}$ and $0.6 M_{\odot}$ respectively. Applying these values to Eq. 4.21 we obtain that $\dot{M}_{\text{RLOF}} = 1.75 \times 10^{-3} M_{\odot} \text{ yr}^{-1}$ according to Eq. 4.21, while the wind mass-loss rate at this point is $\dot{M}_{\star, \text{W}} = 1.02 \times 10^{-5} M_{\odot} \text{ yr}^{-1}$.

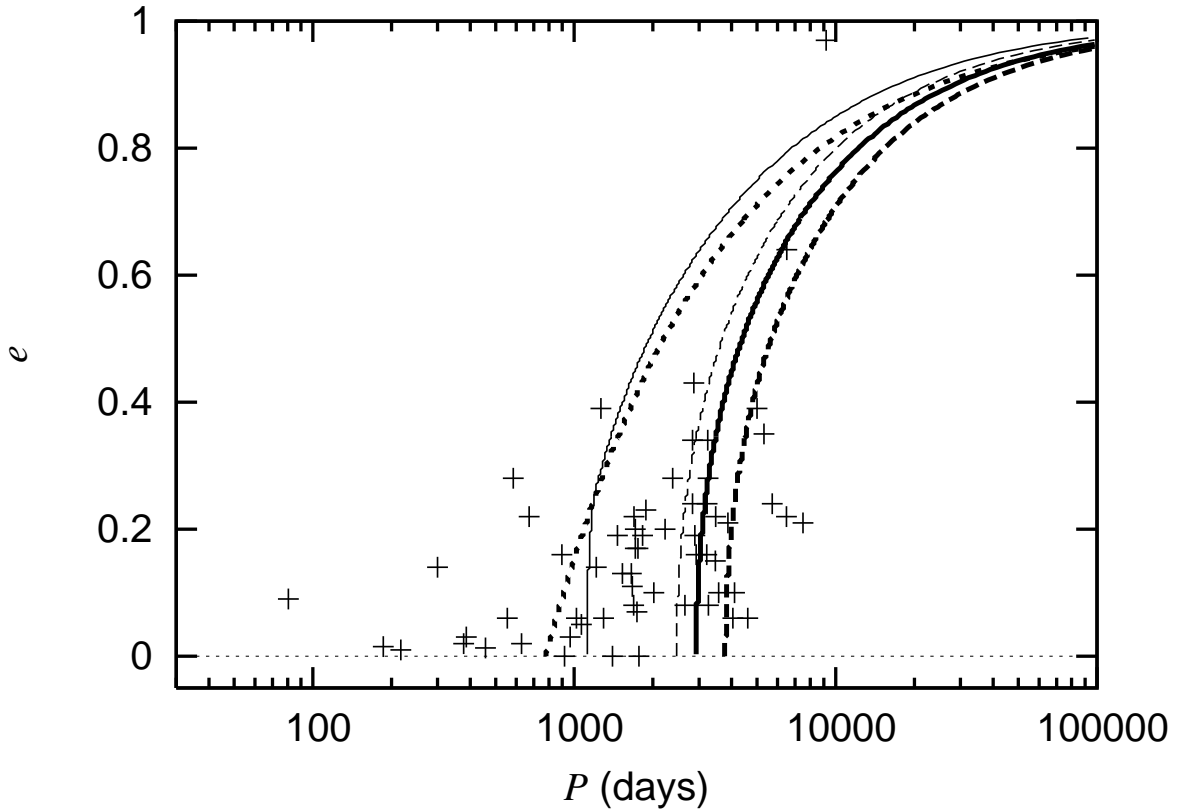


Figure 4.4: Distribution in the $e - P$ plane of barium star and the limits for circularisation set by different models. The crosses indicate the observational data of barium stars from Jorissen et al. (1998). The thick lines delimit the regions where eccentric and circularised orbits are expected and are calculated for a system as described in the text, by assuming a tidal dissipation factor $f' = 1$. The thin lines show the same limits as the thick lines, but this time calculated by assuming $f' = 0.1$. Solid lines indicate the circularisation limit when the eccentricity pumping mechanism we propose is considered. The dashed lines show the circularisation limit in the standard scenario. The dotted line indicates the limit for which Roche lobe overflow occurs at the periastron and the horizontal thin dotted line indicates $e = 0$.

Our results are shown in Fig. 4.4 and are compared to the observed data from Jorissen et al. (1998) in the $e - P$ plane. The thick dashed line separates the region where the orbits will be circularised (to the left of the line) from the region where eccentric orbits are possible (to the right of the line) in the standard binary scenario, where only the tidal circularisation is

acting. This limit is calculated by assuming $\tau_{\text{circ}}^{-1} = M/\dot{M}$ and a tidal dissipation factor $f' = 1$, and reasonably well reproduces the limit resulting from binary population synthesis calculations (e.g., Pols et al. 2003). The majority of the systems cannot be explained in this picture. The thick solid line indicates the same limit, but with the eccentricity pumping mechanism included, i.e., when $|\tau_e^{-1} - \tau_{\text{circ}}^{-1}| = M/\dot{M}$. The evolution of binary systems in the $e - P$ plane is similar to that in the $e - a$ plane (shown in Fig. 4.2), thus the eccentricities of the systems to the right of the thick line can be explained. This means that with the default tidal strength the eccentricity-enhancement mechanism cannot compete effectively with the tidal circularisation, except for a very limited period range around 3000 days. However, the tidal dissipation factor f' is not very certain for AGB stars, given that it has been measured to be approximately unity mostly using observations of red giants (Verbunt & Phinney 1995). Hence it is reasonable to calculate the circularisation limits for smaller values of f' , as our calculations for the Sirius system suggest. Fig. 4.4 shows in thin lines the same limits that we have already described above, but assuming $f' = 0.1$. In this case the eccentricity of almost all systems which do not fill their Roche-lobes can be explained. Karakas et al. (2000) found that with a similar choice of f' they could reproduce the eccentricities of all observed barium stars, including those with periods less than 1000 days. In their simulations they included a tidally enhanced AGB mass loss rate as well, but without any eccentricity-enhancing mechanism to compete against tidal circularisation. However, the results they report are difficult to understand in the light of our findings, especially because they excluded all systems in which the AGB star filled its Roche lobe. The systems to the left of the thick dotted line in Fig. 4.4 fill their Roche lobes during the AGB and in most cases enter a common envelope (CE) phase. The evolution of the orbit during this phase is not a well understood problem and is also beyond the scope of this study. However, it seems more likely that an already eccentric system which enters a CE phase may remain eccentric than that a circular system becomes eccentric during the CE phase. Thus a mechanism which at least allows orbits to remain eccentric until the point when Roche-lobe overflow occurs may be necessary to explain the eccentric systems which are to the left of the Roche-lobe limit. As shown in Fig. 4.4, assuming weak tidal friction with $f' = 0.1$ makes it possible that systems with an AGB primary fill their Roche lobe with a significant eccentricity.

In order to test whether the eccentricity-enhancing mechanism explains the properties of the barium stars, the full evolutionary history has to be followed (as in the case of Sirius) in a binary population synthesis study. Furthermore, not only the orbital parameters have to be reproduced, but also their abundance distributions. Such an analysis is beyond the scope of this work and we will present it in a subsequent paper.

4.5 Conclusions

We have revised the description of the evolution of orbital parameters due to mass loss and mass transfer in a binary system where the primary is an AGB star. We also propose a tidally enhanced mass-loss rate for AGB stars in binary systems which allows a smooth transition between wind mass loss and mass loss due to Roche lobe overflow. With our revised pre-

scription for the evolution of the orbital eccentricity and the fact that our proposed mass loss is not constant along an eccentric orbit, we find an eccentricity enhancing mechanism which counteracts the circularising effect of tidal dissipation. We have shown that the standard scenario of binary interaction cannot explain the observed orbital parameters of the eccentric binary system Sirius unless the strength of tidal dissipation in AGB stars is at least 3 orders of magnitude smaller than in normal red giants. On the other hand, our models with the eccentricity-enhancing mechanism can reproduce the orbital properties of the Sirius system with a reasonable choice of the tidal dissipation parameter ($f' = 0.25$). Our eccentricity enhancing mechanism also allows binary systems containing barium stars to remain eccentric with periods as short as about 1000 days under reasonable parameter assumptions, while under the same assumptions in the standard scenario of tidal circularisation only systems with periods longer than about 2500 days are expected to show a significant eccentricity. We also show that we can explain the eccentricities of almost all barium star systems which do not fill their Roche lobes if the uncertain convective tidal dissipation strength in AGB stars is reduced by a factor of 10, compared to what is measured for red giant stars. Moreover, this assumption allows Roche-lobe overflow to occur in significantly eccentric systems, which may be the key to explain shorter-period barium-star systems which are still eccentric.

Whether our eccentricity-enhancing mechanism is a viable solution to the problem of explaining short-period eccentric binaries with (former) AGB stars, in particular barium stars, needs to be tested with a binary population synthesis model. Results of such a test are given in Chapter 5.

Chapter 5

Population synthesis of eccentric barium stars

A.A. Bonačić Marinović, O.R. Pols,
To be submitted to Astronomy & Astrophysics

Abstract Barium stars are the secondary stars in binary stellar systems where the primary has already evolved through the asymptotic giant branch (AGB) phase to the white dwarf track. Most of barium-star systems show significant orbital eccentricities, while the current binary interaction models predict their orbits to be circularised. One of the mechanisms proposed to counteract the tidal circularisation is based on the influence of the companion on the AGB primary. This influence may produce an enhanced variable mass-loss along the eccentric orbit, which consequently enhances the eccentricity. We test whether this mechanism is a viable solution to explain the eccentric orbits of barium-star systems by following the full evolutionary history of barium star binary progenitors. We include the mass-loss and eccentricity enhancing mechanism prescription in a rapid synthetic binary evolution code. We produce synthetic populations of barium stars and compare them to the observational data. We find that, by assuming the eccentricity enhancing mechanism under the standard assumption of tidal dissipation strength, most of the observed barium-star systems which did not fill their Roche lobes are reproduced and almost all of these are reproduced if the tidal strength is reduced in a factor 4. This somewhat weaker tidal dissipation may also allow systems to enter a common envelope phase while still eccentric. Our description of common envelope evolution prevents binaries filling their Roche lobes to remain eccentric, so we cannot explain those observed eccentric systems with periods shorter than about 1000 days. We find an overproduction of systems with larger periods than 10000 days compared to the observations, which may indicate that the accretion at long periods is less efficient than assumed.

5.1 Introduction

Barium stars are typically G- or K-type giants, which were first singled out as chemically peculiar stars by Bidelman & Keenan (1951), and they account for about 1% of the total number of giants. They present enhanced abundances of elements synthesised via *slow* neutron capture process (*s*-process), most prominently of barium, which range from about 2 to 25 times higher than in normal giants (e.g., Malaney & Lambert 1988 and more recently Liang et al. 2003; Allen & Barbuy 2006; Smiljanic et al. 2007). After about a decade of observations it was discovered that all barium stars are in spectroscopic binary systems (e.g., McClure et al. 1980; McClure 1984; Jorissen & Mayor 1988; McClure & Woodsworth 1990) and many of them exhibit significant eccentricities, but their average eccentricity is smaller than the eccentricity of their normal giant counterpart. The nucleosynthesis of *s*-process elements from Sr to Pb takes place in thermally pulsating (TP-) asymptotic giant branch (AGB) stars (e.g., Smith & Lambert 1990) and these elements are mixed into the giant envelope of the TP-AGB star by recurrent dredge-up episodes. All of the above, in addition with strong evidence that the companions of barium star are white dwarfs (e.g., McClure & Woodsworth 1990) constitutes clear evidence that the *s*-process enhancements in barium stars are due to accretion of mass from their former AGB companion, now a white dwarf.

Mass transfer may occur via two channels. The first is Roche-lobe overflow (from here on RLOF), in which the AGB star radius grows large enough to fill its Roche lobe, transferring mass through the first Lagrangian point. Unless the AGB star is less massive than its companion, RLOF leads to dynamically unstable mass transfer and the system enters into a common envelope (hereafter CE) phase. Given that RLOF is basically the extreme case of tidal deformation, the interaction between the tides and the convective envelope is very strong when the AGB star is close to fill its Roche lobe. This produces a strong dissipation of energy due to convective damping, which is expected to efficiently circularise the orbit. Since this is inconsistent with the observed non-zero eccentricities of barium stars, RLOF mass transfer has been ruled out as the process responsible for the *s*-process enrichment of the barium stars. The second channel of mass transfer is via wind accretion, which allows the secondary star to accrete some of the mass that has been lost in the form of wind from the AGB primary, allowing systems which are significantly separated to exchange mass. Boffin & Jorissen (1988) show that a barium star can be formed under this scenario.

Since barium stars present material which formerly belonged to their companion, they are a useful tool for probing mass transfer and nucleosynthesis in binary systems. Moreover, the chemical and orbital properties of these systems do not change significantly after the primary became a white dwarf, thus the currently observed *s*-process enhancements, periods and eccentricities are representative of the values of these parameters when the primary finished its AGB phase.

Barium-star systems are observed to have periods in the range 80–10000 days. Most of them have orbital eccentricities from circular to about 0.4 (Jorissen et al. 1998), with a couple of exceptions with $e = 0.64$ and $e = 0.97$. Han et al. (1995) investigated the formation of barium stars with different mechanisms of mass accretion employing binary population synthesis

calculations. They examined the period and mass distribution of barium-star systems, together with their formation rate. However, they did not study their eccentricity distribution.

Due to the large size of AGB stars, systems with periods shorter than about 3000 days should have experienced strong tidal dissipation. This implies that all these systems are expected to have circular orbits, which is falsified by the observations. Concerning this problem, another population synthesis study of barium stars was carried out by Karakas et al. (2000), with an improved estimate of the barium enhancement of the TP-AGB star and dilution into the atmosphere of the accreting star. They reproduced the observed eccentricities of all observed barium stars. However, this result is debated.

Two main mechanisms which may counteract the circularising effects of tidal interaction have been proposed: mass-loss enhancement due to filling of the Roche lobe at periastron (Van Winckel et al. 1995; Soker 2000) and tidal interaction between the binary system and a circumbinary disk (Waelkens et al. 1996; Waters et al. 1998). However, the first mechanism works only if the systems are close enough so the Roche lobe is filled at periastron passages, and the second mechanism works only if the mass of the circumbinary disk is large enough: Soker (2000) argues that the observed masses of these disks are too small to significantly counteract the circularisation. In Chapter 4 we propose an enhanced AGB mass-loss rate which depends on the instantaneous distance to the companion. This represents a form of mass loss which can be called “wind RLOF”, where the wind mass loss rate from the AGB star becomes larger when the star is closer to fill its Roche lobe. As a consequence, mass loss along eccentric orbits is variable, with higher rates at orbital phases closer to the periastron. This provides a mechanism that permanently competes against tidal circularisation.

In Chapter 4 we estimate that the eccentricities of barium-star systems could be explained by considering the eccentricity-enhancing wind-ROLF mechanism. This was done by comparing the timescale in which this mechanism acts to the timescale of circularisation due to tidal interaction. However, these timescales were evaluated only for a binary system of given initial masses, at the moment when the tidal interaction was the strongest due to the large radius of the AGB primary. In order to test if the eccentricity-enhancing effect we propose can explain the properties of barium-star systems, the full evolutionary history of binary system with initial masses and periods in the range capable of producing barium stars has to be followed in a binary population synthesis study. For this purpose we have implemented the AGB mass-loss prescription and the description of the orbital evolution that we derive in Chapter 4 into a rapid synthetic binary evolution code based on that of Hurley et al. (2002), Izzard et al. (2004) and Izzard et al. (2006). We compare the observational data of Jorissen et al. (1998) to the distributions of the orbital parameters and *s*-process enhancements of our synthetic barium stars to verify if our models can satisfactorily reproduce the observations.

In § 5.2 we indicate our assumptions of free parameter values to carry out model calculations and explain those relevant to the binary evolution. In § 5.3 we describe the population synthesis method. In § 5.4 we explain our results and compare them to the observations. The results are discussed in § 5.5, where we also draw our conclusions.

5.2 The binary evolution models

We follow the binary stellar evolution and nucleosynthesis by employing a modified version of the rapid evolutionary code by Hurley et al. (2002), Izzard et al. (2004) and Izzard et al. (2006). The modifications to the treatment of AGB evolution and nucleosynthesis are described in detail in Chapter 2. The single stellar evolution is based on fits to the detailed stellar models of Pols et al. (1998), Karakas et al. (2002) and Stancliffe et al. (2004). The nucleosynthesis of *s*-process elements is modelled by interpolating results from the detailed models of Gallino et al. (1998, see Izzard et al. 2006). In Chapter 2 we constrain the values of free parameters that affect model nucleosynthesis results from single stars by comparing to data of observed AGB stars. These values are the shift in the minimum core mass for TDU to occur with respect to the models of Karakas et al. (2002), $\Delta M_c^{\min} = -0.065 M_\odot$, the minimum asymptotic value of the dredge-up efficiency, $\lambda_{\min} = 0.2$, the mass of the ^{13}C pocket as fraction of the intershell mass, $f_{^{13}\text{C,IS}} = 1/40$, and the ^{13}C efficiency, $^{13}\text{C}_{\text{eff}} = 1$. Refer to Chapter 2 for more details on the meaning of these free parameters. We assume that the same values apply to AGB stars in binary systems, i.e., there are no intrinsic differences in AGB nucleosynthesis in single and binary stars. However, differences occur due to mass loss or mass gain in binary systems.

We have modified the description of the evolution of the masses and orbital parameters in the presence of wind mass-loss and wind accretion according to the methodology presented in Chapter 4. In the following subsections we describe in more details the modifications that we have implemented and we discuss the free parameters that are the most relevant for the orbital evolution.

5.2.1 Enhanced mass loss from AGB stars in binary systems

AGB stars have shallow surface density gradients which suggests that in binary systems, as the radii of these stars approach their Roche-lobe radii, their mass loss experiences a smooth transition between the stellar wind to the Roche-lobe overflow mass-loss regime (see detailed discussion in Chapter 4). We model this transitional form of wind Roche-lobe overflow mass-loss from an AGB star as

$$\dot{M}_\star = \dot{M}_{\star,w} \left[1 + \left(\frac{\dot{M}_{\text{RLOF}}}{\dot{M}_{\star,w}} - 1 \right) \left(\frac{R_\star}{R_L} \right)^6 \right], \quad (5.1)$$

where $\dot{M}_{\star,w}$ is the single-star wind mass-loss rate, for which we employ the law of Vassiliadis & Wood (1993). R_\star and R_L are the radius and Roche-lobe radius of the AGB star, respectively. \dot{M}_{RLOF} is the Roche-lobe overflow mass-loss rate of the star evaluated as if its Roche-lobe radius were equal to R_\star (see Chapter 4 for details) and is evaluated with the prescription of Ritter (1988, see also Meyer & Meyer-Hofmeister 1983; Pastetter & Ritter 1989) as

$$\dot{M}_{\text{RLOF}} = \frac{2\pi}{\sqrt{e}} \left(\frac{k_B}{m_H \mu_\star} T_\star \right)^{3/2} \frac{R_\star^3}{GM_\star} \rho_{\star,\text{ph}} F(q_\star^{-1}), \quad (5.2)$$

with $F(x) = 1.23 + 0.5 \log x$. $q_\star = M_\star/M_A$, where M_\star is the mass of the AGB star and M_A is the mass of the accreting companion, and T_\star and μ_\star are the temperature and molecular weight of the AGB star, respectively. We consider the photospheric density of the AGB star to be (Kippenhahn & Weigert 1990; Soker 2006)

$$\rho_{\star, \text{ph}} = \frac{2}{3} \frac{m_{\text{H}} \mu_\star}{k_{\text{B}}} \frac{GM_\star}{R_\star^2 \kappa_\star T_\star}, \quad (5.3)$$

where κ_\star is the opacity in the photosphere of the AGB star and m_{H} and k_{B} are the mass of the hydrogen atom and the Boltzmann constant respectively. AGB barium-star progenitors have initial masses in the range 1.5–3.5 M_\odot and surface temperature of about 3300K. According to the envelope opacity calculations of Marigo (2002), the corresponding opacity at this temperature is approximately $\kappa_\star = 2.5 \times 10^{-4} \text{ cm}^2 \text{ g}^{-1}$ for densities of the order of $10^{-13} - 10^{-11} \text{ g cm}^{-3}$, which is the expected range of AGB surface densities. Evaluating Eq. (5.2) for one of these stars yields $\dot{M}_{\text{RLOF}} \sim 10^{-3} M_\odot \text{ yr}^{-1}$. This is approximately four orders of magnitude larger than the single-star wind mass-loss rate of our typical star at the beginning of the AGB lifetime, calculated with the prescription of Vassiliadis & Wood (1993). By the end of the AGB phase, at the onset of the superwind phase, \dot{M}_{RLOF} is still 50-200 times larger than the wind mass-loss rate.

5.2.2 Mass accretion on the companion

The standard model used for mass accretion from a stellar wind on a companion star is the prescription of Bondi & Hoyle (1944) under the assumption of a wind with constant velocity and emanating from a star which has a constant mass-loss rate (e.g., Hurley et al. 2002). However, following our assumption of an enhanced mass-loss from AGB stars in the presence of a companion, we assume that a fraction β_{WRL} of the extra mass lost is accreted by the companion. Hence, we employ the prescription

$$\dot{M}_{\text{ACC}} = \dot{M}_{\text{BH}} + \beta_{\text{WRL}} (\dot{M}_{\text{RLOF}} - \dot{M}_{\star, \text{w}}) \left(\frac{R_\star}{R_{\text{L}}} \right)^6, \quad (5.4)$$

in which \dot{M}_{BH} stands for the standard Bondi & Hoyle accretion rate, given in this context by

$$\dot{M}_{\text{BH}} = \alpha_{\text{BH}} \frac{(GM_A)^2 \dot{M}_{\star, \text{w}}}{r_A^2 w_{\text{rel}, A}^3 w_\star}, \quad (5.5)$$

where r_A is the distance from the companion to the AGB star at the moment the wind was emitted and $w_{\text{rel}, A}$ is the wind velocity relative to the companion at the moment it is accreted. The velocity of the wind as seen from the AGB star $w_\star = \beta_w \sqrt{2GM_\star/R_\star}$ is assumed proportional to the escape velocity of the AGB star by the factor $\beta_w = 0.125$ (Hurley et al. 2002). The parameter α_{BH} accounts for the uncertainties related to this prescription for mass accretion and is generally assumed to be 1.5 (e.g., Boffin & Jorissen 1988; Han et al. 1995). However, hydrodynamical simulations of wind accretion from an AGB star obtain rather small values of $\alpha_{\text{BH}} \sim 0.1-0.2$ (see, e.g., Theuns et al. 1996; Nagae et al. 2004).

The accreted material has a higher mean molecular weight than the envelope of the companion star. Under these conditions thermohaline mixing occurs (see, e.g., Stancliffe et al. 2007). Therefore, the accreted material is assumed to be mixed deep into the companion star, even if the star has a radiative envelope. This kind of mixing occurs on a thermal timescale, which is much shorter than the main-sequence lifetime, so in our models we assume that the mixing is instantaneous and occurs throughout the envelope of the star.

5.2.3 Strength of the tidal convective dissipation

To model the evolution of the eccentricity, e , due to tidal interactions on the convective envelope of an AGB star Hurley et al. (2002) combine the results of Zahn (1977, see also Zahn & Bouchet 1989) and Hut (1981) and give the expression

$$\begin{aligned} \left(\frac{\dot{e}}{e}\right)_{\text{tides}} = & -\frac{18}{7} \frac{f_{\text{conv}}}{\tau_{\text{conv}}} \frac{M_{\text{env}}}{M_{\star}} \frac{(1+q_{\star})}{q_{\star}^2(1-e^2)^{13/2}} \left(\frac{R_{\star}}{a}\right)^8 \\ & \times \left[f_3(e^2) - \frac{11}{18}(1-e^2)^{3/2} f_4(e^2) \frac{\Omega_{\star,s}}{n} \right], \end{aligned} \quad (5.6)$$

where q_{\star} is the mass ratio of the AGB star to its companion, and M_{env} , $\Omega_{\star,s}$ and n are the envelope mass of the AGB star, the spin angular velocity of the AGB star and the average orbital angular velocity, respectively. The convective timescale $\tau_{\text{conv}} = 0.2351(M_{\text{env}}R_{\star}^2/L_{\star})^{1/3}\text{yr}$, where L_{\star} is the luminosity of the AGB star and the parameters are expressed in solar units (see Hurley et al. 2002). The functions $f_x(e^2)$ are from Hut (1981) and the numerical factor $f_{\text{conv}} = f_{\text{tid}} \min(1, (P_{\text{tid}}/2\tau_{\text{conv}})^2)$ from Rasio et al. (1996), where $P_{\text{tid}}^{-1} = |n - \Omega_{\star,s}|/2\pi$. The free parameter f_{tid} accounts for the uncertainty in the convective damping due to the tides. Verbunt & Phinney (1995) found that $f_{\text{tid}} \approx 1$ from an analysis of observed red-giant binaries, however, this value may differ in the case of AGB stars.

In almost all of the cases that we are interested in, the term inside the bracket in Eq.(5.6) is positive, thus the overall effect is the circularisation of the orbit, which occurs on a timescale $\tau_{\text{circ}}^{-1} \equiv |(\dot{e}/e)_{\text{tides}}|$.

5.2.4 Variation of orbital elements due to mass loss and mass accretion

In addition to the circularising effect of the tides, the eccentricity of a binary system is affected by the mass lost by the system and the mass transferred from the primary to the secondary star. Moreover, the eccentricity is affected in a different way depending on the orbital phase, θ , at which the mass loss and mass transfer take place. We employ the expression given by Eq. (11)

of Chapter 4 to model the eccentricity change due to variations in the masses:

$$\begin{aligned} \dot{e} = & \frac{\dot{M}_{\star, \text{LOST}}(\theta)}{M_{\star} + M_{\text{A}}} \left\{ e + \cos \theta \right\} \\ & + \frac{\dot{M}_{\text{ACC}}(\theta)}{M_{\text{A}}} \left\{ \frac{M_{\star}}{M_{\star} + M_{\text{A}}} \left[\left(\frac{\xi_{\star} M_{\text{A}}^2}{M_{\star}^2} - 1 \right) (2 \cos \theta + e + e \cos^2 \theta) \right. \right. \\ & \left. \left. - e \sin^2 \theta \right] + w_{\star} \sqrt{\frac{a(1-e^2)}{G(M_{\star} + M_{\text{A}})}} \sin \theta \right\}, \end{aligned} \quad (5.7)$$

where a is the semi-major axis of the orbit, $\dot{M}_{\star, \text{LOST}} = \dot{M}_{\star} - \dot{M}_{\text{ACC}}$ is the mass lost by the primary that is also lost by the system, i.e., is not accreted by the secondary, and ξ_1 is the ratio of specific angular momentum of the wind accreted by the secondary to the orbital angular momentum of the primary. We assume that the angular momentum of the wind is conserved from the moment it is emitted from the primary star, so $\xi_1 = 1 + (h_{\star, \text{spin}}/h_{\star, \text{orb}})$, where $h_{\star, \text{spin}}$ and $h_{\star, \text{orb}}$ are the specific spin angular momenta of the shell expelled as wind from the AGB star and the orbital specific angular momentum of the AGB star, respectively.

In the case of an eccentric orbit the distance between the stars, r , varies according to the orbital phase. Therefore, assuming an instantaneous Roche geometry at different θ , the Roche-lobe radius of the primary, R_L , also varies with the orbital phase. This implies that the mass-loss rate of the primary varies along the orbit (see Eq.(5.1)), being larger at periastron passages. Variable mass loss along the orbit leads to an enhancement of the eccentricity, which can compete against the circularising effect of the tidal dissipation. For a given system our evolution code advances with time steps in which the relevant stellar parameters change significantly. These time steps are substantially longer than the orbital period of the system, so for each timestep we compute an average \dot{e} by integrating Eq. (5.7) along one orbit and dividing by the orbital period. We assume that \dot{e} remains the same during the whole time-step given that none of the relevant stellar and orbital parameters change significantly.

5.2.5 Common envelope evolution

In case the AGB star fills its Roche lobe, it loses mass via Roche-lobe overflow. Given that its envelope is convective, this leads to dynamically unstable mass loss to the companion if the AGB star is more massive than its companion, which is normally the case. As mass transfer occurs on a dynamical timescale, it is too fast for the accretor to thermally adjust and the system enters a common envelope phase. The common envelope is expelled from the system within a short timescale, thus no net mass transfer is assumed to take place in this phase. The standard scenario of common envelope evolution proposes that the energy ($-E_{\text{bind}}$) required to unbind the AGB star envelope of mass $M_{\text{env}, \star}$ is transferred from the orbit with an efficiency α_{CE} , which consequently shrinks the orbit. Other energy sources may also be considered for unbinding the envelope, such as the energy released by the recombination of ions or the accretion luminosity (e.g., Iben & Livio 1993; Han et al. 1994). In particular, our models

assume that a fraction f_{ion} of the energy of the ion recombination contributes to the envelope ejection. Thus, the required energy to unbind the envelope is expressed in our models as

$$-E_{\text{bind}} \equiv -\frac{G}{\lambda_{\text{CE}}} \frac{M_{\star} M_{\text{env},\star}}{R_{\star}} - f_{\text{ion}} U_{\text{env,ion}} = \alpha_{\text{CE}} (E_{\text{orb,f}} - E_{\text{orb,i}}), \quad (5.8)$$

where $E_{\text{orb,i}}$ and $E_{\text{orb,f}}$ are the orbital energy of the binary before and after the common envelope is ejected, respectively, λ_{CE} is a factor which accounts for the density distribution inside the envelope, and $U_{\text{env,ion}}$ is the recombination energy of the AGB star envelope. In our current models, we assume $\alpha_{\text{CE}} = 1$, which means that the energy transfer from the orbit into the common envelope is 100% efficient. Since α_{CE} is fixed in our models, the amount of shrinkage of the orbit in our models during a common envelope phase is determined by the choice of f_{ion} . A larger f_{ion} value requires a smaller difference in orbital energy to release the envelope and, in turn, less shrinkage of the orbit (i.e., a larger final orbital separation).

The treatment of eccentric orbits during common envelope evolution is very simple in our models. It consists of first transferring to the envelope the orbital energy dissipated by circularisation, without loss of angular momentum. Following this, once the orbit is circularised, angular momentum is lost and the orbit shrinks. In this way a system which enters the common envelope phase with a finite eccentricity is circularised first and its separation decreased in order to balance the energy required to unbind the envelope.

5.3 Population synthesis

We employ our rapid synthetic binary evolution code to compute a grid of binary evolution models from which we assemble synthetic populations of the systems that we are interested in. The metallicities of barium stars range from approximately $[\text{Fe}/\text{H}] = -0.7$ to $[\text{Fe}/\text{H}] = 0.2$, with an error of about 0.1 dex (e.g., Zacs 1994; Allen & Barbuy 2006; Smiljanic et al. 2007), and where the notation $[\text{X}/\text{Y}] = \log_{10} [(X/Y)_{\text{observed}} / (X/Y)_{\text{solar}}]$. We will assume one fixed metallicity of $Z = 0.008$, which is an average of the observed metallicities of barium stars, in order to restrict our initial parameter set to a 4-dimensional grid of primary mass, secondary mass, period and eccentricity. The range of parameters in our set of initial conditions is as follows:

- 25 initial primary masses separated logarithmically and ranging between $1.3 M_{\odot} < M_{\star,i} < 6.0 M_{\odot}$. This is the range of masses in which substantial amounts of *s*-process elements are mixed into the envelope during the AGB phase.
- 25 initial secondary masses separated logarithmically and ranging between $0.8 M_{\odot} < M_{\text{A},i} < M_{\star,i}$. In this way we make sure that the secondary masses cover the range between the lowest mass a star can have in order to become a red giant within a Hubble time and the mass of the companion.
- 25 initial periods, P_i , separated logarithmically between 50 and 100000 days, in order to cover the range of the observations, which is between 80 and 10000 days.

Table 5.1: Model number and their corresponding assumed parameters. The cases where β_{WRL} is indicated with *N.A.* imply that the models are calculated by only considering the standard tidal circularisation. The other models are calculated including the eccentricity-enhancing prescription. The field *Fixed values* indicates the values which are common to all the models.

Model #	α_{BH}	β_{WRL}	f_{tid}	f_{ion}	Fixed values
1	1.5	N.A.	1.0	0.5	$\kappa_{\star} = 2.5 \times 10^{-4} \text{ cm}^2 \text{ g}^{-1}$
2	0.1	0.5	1.0	0.5	$\beta_w = 0.125$
3	1.5	N.A.	0.25	0.5	$\alpha_{CE} = 1.0$
4	0.1	0.5	0.25	0.5	
5	0.5	N.A.	1.0	0.5	
6	0.1	0.25	1.0	0.5	
7	1.5	0.5	1.0	0.05	
8	0.1	N.A.	1.0	0.05	

- 10 initial eccentricities, separated linearly between 0 and 0.95.

The probability of a computed system to exhibit a particular value of orbital eccentricity, period or separation, or a certain overabundance of *s*-process elements in the secondary component, is weighted by the time that the system spends showing this value and by the probability of occurrence of its initial conditions. We assume that the primary initial mass has the probability distribution, ξ , given by the initial mass function (IMF) of Kroupa et al. (1993)

$$\xi(M_i) = \begin{cases} 0.035M_i^{-1.3} & \text{if } 0.08 < M_{\star,i} < 0.5, \\ 0.019M_i^{-2.2} & \text{if } 0.5 < M_{\star,i} < 1.0, \\ 0.019M_i^{-2.7} & \text{if } 1.0 < M_{\star,i}, \end{cases} \quad (5.9)$$

where $M_{\star,i}$ is the initial stellar mass in solar units. We assume that for a given primary mass, the secondary masses have a flat q_{\star}^{-1} distribution. We employ as initial probability distribution of periods the Gaussian distribution of $\log(P)$ found by Duquennoy & Mayor (1991) for a complete nearby G-dwarf sample, which is centred at the average $(\log(P/\text{days}))_{av} = 4.8$ with a dispersion of $\sigma_{\log P} = 2.3$. We consider a flat probability distribution of initial eccentricities.

5.4 Results

In this section we present the results of our population synthesis calculations. In § 5.4.1 we show results calculated for a small sub set of initial conditions, which have different initial periods but the same initial masses and eccentricity. This has the purpose of clarifying the effect

of including the eccentricity-enhancing mechanism in the models as a function of one parameter instead of four. In § 5.4.2 we compare our synthetic barium stars to the observational data of the sample of barium stars from Jorissen et al. (1998), complemented with abundances measured by Allen & Barbuy (2006).

Due to the enhanced mass-loss rates during the AGB phase the chemical evolution of the binary systems is affected, which is reflected in the abundances of *s*-process elements in the barium stars. Two processes have to take place in order to form a barium star and both are affected by the mass loss from the AGB star. First, the *s*-process elements have to be synthesised in the interior of the AGB star and mixed into the giant envelope of the star by third dredge-up episodes following each thermal pulse. Second, the *s*-process element enriched material has to be accreted by the companion star in amounts high enough to significantly raise the abundance of these elements in the accretor. These two effects oppose each other as an enhanced mass-loss rate on the AGB leads to a higher accretion rate, but it also shortens the life time of the primary in the AGB phase.

The observations provide measurements of the surface abundances of *s*-process elements relative to that of iron. Following the convention, we calculate for each star in our grid its *heavy s*-process (hs) element abundance ratio,

$$\left[\frac{\text{hs}}{\text{Fe}} \right] = \frac{1}{5} \left(\left[\frac{\text{Ba}}{\text{Fe}} \right] + \left[\frac{\text{La}}{\text{Fe}} \right] + \left[\frac{\text{Ce}}{\text{Fe}} \right] + \left[\frac{\text{Nd}}{\text{Fe}} \right] + \left[\frac{\text{Sm}}{\text{Fe}} \right] \right), \quad (5.10)$$

and *light s*-process (ls) element abundance ratio,

$$\left[\frac{\text{ls}}{\text{Fe}} \right] = \frac{1}{2} \left(\left[\frac{\text{Y}}{\text{Fe}} \right] + \left[\frac{\text{Zr}}{\text{Fe}} \right] \right). \quad (5.11)$$

To account for the systems containing barium stars we select those in which the primary star has already become a white dwarf and the secondary is on the red giant branch. The secondary star must also present an over-abundance of *s*-process elements $[s/\text{Fe}] > 0.2$ dex, which is an approximate estimate of the error in the measurements, and where $[s/\text{Fe}] \equiv ([\text{hs}/\text{Fe}] + [\text{ls}/\text{Fe}])/2$.

The set of parameters that we employ in our models is summarised in Tab. 5.1. We divide the population synthesis models in two main groups: those calculated by considering that the eccentricity varies only due to tidal dissipation, which are labelled with odd numbers and hereafter called *standard* models; and those calculated by assuming the mass-loss and eccentricity enhancement proposed in Chapter 4, which are labelled with even numbers and hereafter called *e-enhanced* models.

5.4.1 Analysis of systems with equal initial masses and eccentricity

In order to understand more clearly the effect of including the enhanced mass-loss and eccentricity enhancement mechanism, we synthesise four sets of models of barium-star binaries, all

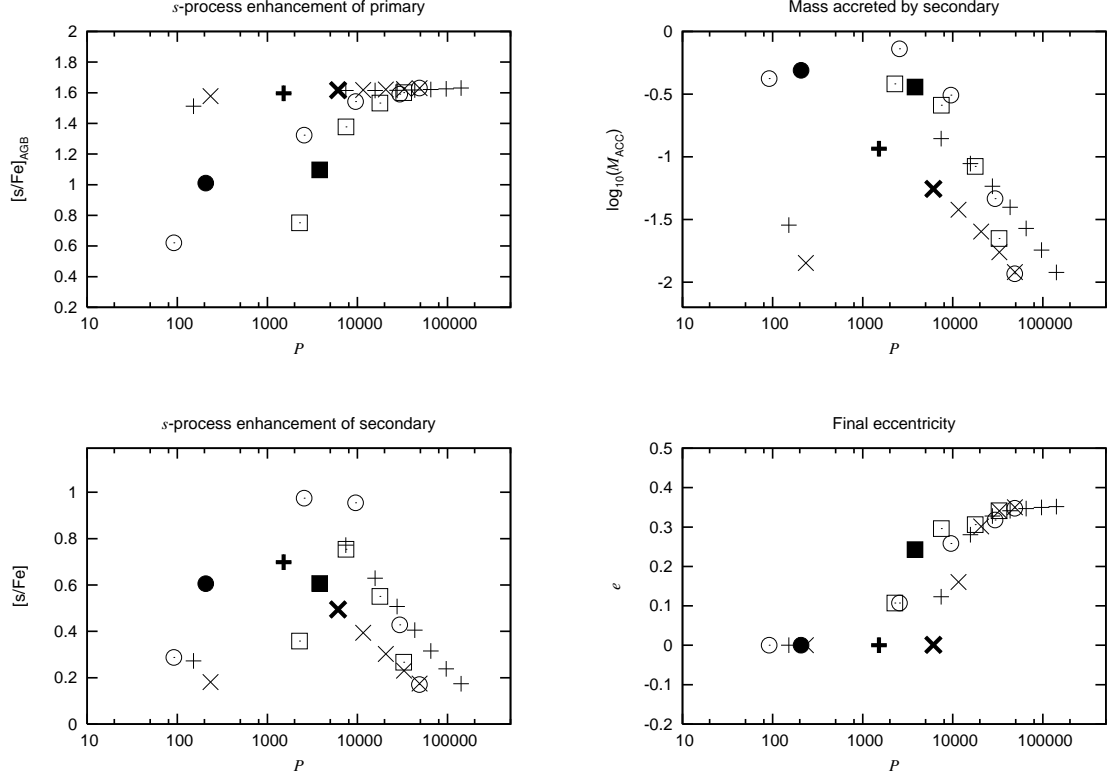


Figure 5.1: Synthetic barium-star properties are plotted as a function of the final period for binaries with initial masses of $2.22 M_{\odot}$ and $1 M_{\odot}$, initial eccentricity $e_i = 0.356$ and periods between 50 and 100000 days, as specified in the text. The horizontal and diagonal crosses show results of models 1 and 5, respectively, which are standard models. The circles indicate results of model 2 and the squares those of model 6, both of which are e -enhanced models. The thick/solid symbols show the models which started with the same initial period.

having the same initial values of the primary mass, $M_{\star,i} = 2.22 M_{\odot}$, secondary mass, $M_{A,i} = 1 M_{\odot}$ and eccentricity, $e_i = 0.356$, and the same set of 15 logarithmically spaced initial periods in the range 50-100000 days. Models 1 and 5, indicated by horizontal and diagonal crosses in Fig. 5.1) are standard models. They differ from each other in the choice of the Bondi & Hoyle accretion efficiency parameter, which is $\alpha_{BH} = 1.5$ for model 1 (horizontal crosses) and $\alpha_{BH} = 0.5$ for model 5 (diagonal crosses). Models 2 and 6 (indicated by circular and square symbols, respectively, in Fig. 5.1) are e -enhanced models, for which we assume a low value of $\alpha_{BH} = 0.1$. This low value is consistent with the results of hydrodynamical simulations of wind accretion (Theuns et al. 1996; Nagae et al. 2004). These models differ from each other in the fraction of the enhanced mass loss accreted by the companion, which is $\beta_{WRL} = 0.5$ for model 2 (circles) and $\beta_{WRL} = 0.25$ for model 6 (squares). Systems which have the same initial period, $P_i = 3500$ days, are indicated by solid and thick symbols, making it easier to make a one to one comparison between the models.

The top-left panel of Fig. 5.1 shows the overall s -process element enhancement, $[s/Fe]$, at the end of the AGB phase. The amount of s -process enhancement increases in proportion to the lifetime of the thermally-pulsing AGB phase. Hence, for the standard models 1 and 5, the final s -process enhancement is almost independent of the initial period. In these models the AGB star evolves as if it were a single star, as long as it does not fill its Roche lobe. On the other hand, for e -enhanced models 2 and 6 (circles and squares), the final s -process enhancement decreases gradually with decreasing initial period. The smaller is the period, the stronger is the mass-loss enhancement and the shorter is the AGB phase of the primary star. Note that systems in which less mass is accreted by the companion (smaller β_{WRL}) have larger final periods (compare the filled symbols in Fig. 5.1), because mass transfer tends to bring the stars closer together and thus opposes the widening of the orbit caused by mass loss from the binary system. Consequently, in model 2 with a higher β_{WRL} systems are more likely to fill their Roche lobe, leading to smaller s -process enhancements.

The amount of mass accreted by the secondary companion is shown in the top-right panel of Fig. 5.1 for the same set of models. In the standard models (1 and 5, represented by crosses) the accretion rate scales approximately with a^{-2} (see Eq. (5.5)), so the amount of mass accreted decreases with orbital period. A lower accretion efficiency (a lower value of α_{BH} , model 5) naturally leads to less accretion at the same period. On the other hand, in the e -enhanced models we assume a small value of $\alpha_{\text{BH}} = 0.1$. Therefore the accretion rate in these models is dominated by the assumed fraction β_{WRL} of the enhanced mass-loss rate that is accreted, which scales with distance as a^{-6} (see Eqs. (5.1) and (5.4)). This leads to a steeper decrease of the accreted mass with orbital period than in models 1 and 5 and accounts for the higher amount of mass accreted in systems with periods below about 10000 days. Again, a smaller value of β_{WRL} (model 6, square symbols) naturally leads to less accretion. In all models the largest mass accretion occurs for systems that were just wide enough to avoid filling their Roche lobes, at $P \sim 1000 - 2000$ days. Closer systems entered a common-envelope phase, which truncated both the AGB evolution and any further accretion.

The lower-left panel of Fig. 5.1 shows the enhancement of s -process elements in the secondary component, i.e., the resulting barium star. This is proportional to both the amount of mass accreted (Fig. 5.1, upper-right panel) and the s -process enhancement in the accreted material, which is similar to the final s -process enhancement of the primary shown in the upper-left panel. For all models there is a peak in the s -process enhancement of the secondary around periods in the range 1000–10000 days. In the standard models this mostly reflects the amount of mass accreted as a function of period. In the e -enhanced models, instead, the decrease in s -process enhancement towards smaller periods is mostly caused by the lower s -process enhancement in the AGB primary star in closer systems.

Barium stars are observed to have s -process enhancements up to about 1 dex, and models without enhanced mass loss therefore require a large value of the Bondi-Hoyle accretion efficiency to reproduce these measurements, at least $\alpha_{\text{BH}} = 1.5$. This is an order of magnitude higher than the accretion efficiencies reached in hydrodynamical simulation of wind accretion (e.g., Theuns et al. 1996; Nagae et al. 2004). Also in e -enhanced models a large amount of accretion is required to reproduce the observed abundances in barium stars. In this case we

can allow a moderate Bondi-Hoyle efficiency of $\alpha_{\text{BH}} = 0.1$, but we need to assume that 50% of the enhanced mass lost in the wind Roche-lobe overflow process is accreted by the companion ($\beta_{\text{WRL}} = 0.5$).

The final eccentricities of our four sets of models are shown in the lower-right panel of Fig. 5.1. Systems with periods shorter than 10000 days are able to remain eccentric in the set of e -enhanced models, consistently with the findings of Chapter 4. We also note that systems which accrete more mass remain closer, so they are more likely to become circularised and also more likely to enter a common envelope phase.

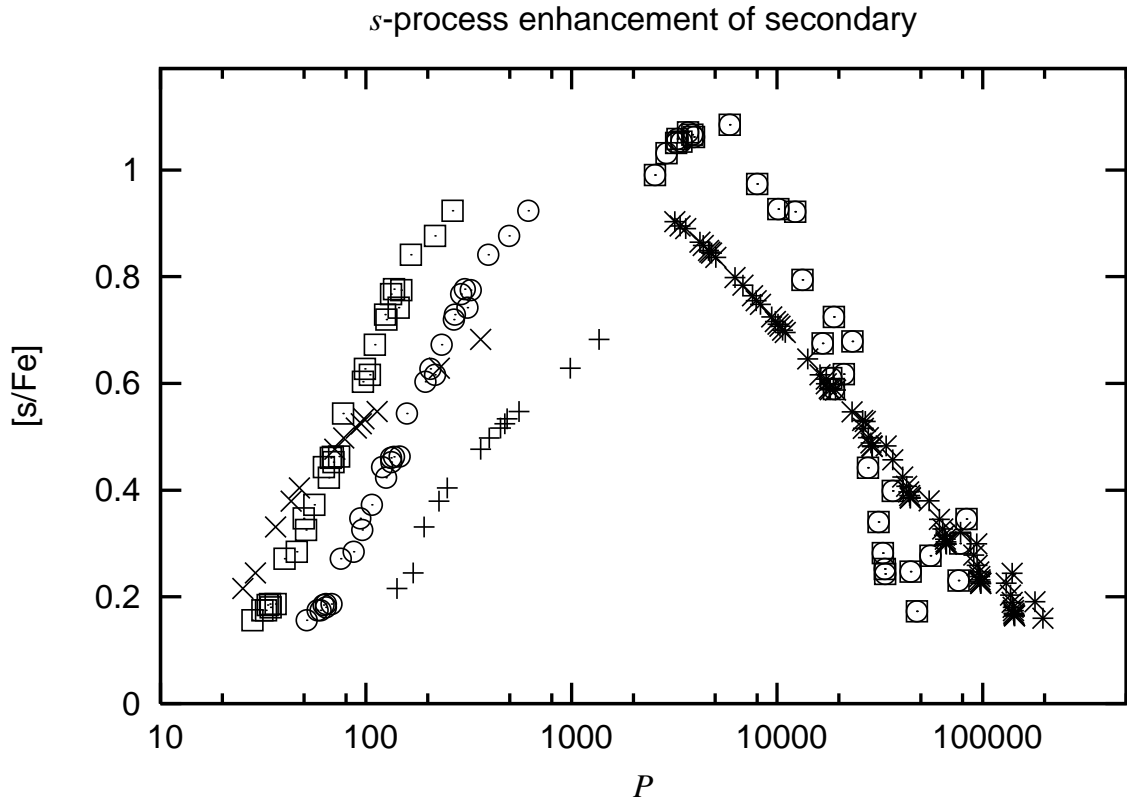


Figure 5.2: Effect of changing the parameter f_{ion} on the s -process enhancement as a function of period, for the same masses as in Fig. 5.1 but a range of eccentricities as described in the text. Models 1, 2, 7 and 8 are indicated by horizontal crosses, circles, diagonal crosses and squares, respectively. Only systems with periods less than 1000 days, which underwent a common-envelope phase, are affected. The smaller f_{ion} , the more energy is transferred from the orbit in order to eject the common envelope, which results in smaller periods after a common-envelope phase.

The effect of varying the fraction of the ionisation energy used in ejecting a common envelope, f_{ion} , is shown in Fig. 5.2. We consider the same initial primary and secondary masses and the same set of initial periods as above, but now include a set of 10 initial eccentricities ranging from 0 to 0.9. We show four sets of models in Fig. 5.2, where the open symbols indicate the e -enhanced models with $\alpha_{\text{BH}} = 0.1$ and $\beta_{\text{WRL}} = 0.5$ (models 2 and 8), and the crosses

indicate standard models with $\alpha_{\text{BH}} = 1.5$ (models 1 and 7). The circles and horizontal crosses indicate those models for which $f_{\text{ion}} = 0.5$ and the squares and diagonal crosses indicate those for which $f_{\text{ion}} = 0.05$. Systems with periods over 2000 days avoided RLOF and a common-envelope phase and are not affected by the choice of f_{ion} . Systems shorter than about 1000 days did undergo common-envelope evolution, and for these systems Fig. 5.2 shows that for smaller values of f_{ion} the orbits shrink more, given that more energy from the orbit is required to eject the common envelope. We assume a default value in our models of $f_{\text{ion}} = 0.5$ because this choice best reproduces the observed barium stars with periods less than 1000 days.

5.4.2 Comparison of results from the 4-dimensional space of initial parameters to observational data

In this section we show our synthetic barium stars calculated with the 4-dimensional initial grid described in § 5.3 and we compare them to the data gathered from observations (Jorissen et al. 1998, complemented with the data of Allen & Barbuy 2006). To carry out this comparison we have binned the eccentricity-period and s -enhancement-period probability distributions resulting from our population synthesis runs. Each system is weighed by its initial formation probability and the amount of time it spends showing the parameters of interest, as explained in § 5.3. The bins have a resolution of 0.1 in the logarithm of the period, $\log_{10}(P/\text{days})$, of 0.05 in the eccentricity and 0.075 dex in the overabundance of s -process elements, $[\text{s}/\text{Fe}]$. We calculate the s -process element overabundance by following Busso et al. (2001), where $[\text{s}/\text{Fe}] = ([\text{ls}/\text{Fe}] + [\text{hs}/\text{Fe}])/2$ and $[\text{ls}/\text{Fe}]$ and $[\text{hs}/\text{Fe}]$ are the average overabundances of light and heavy s -process elements, respectively (see, e.g., Chapter 2 for details).

Eccentricity-period distribution

First we analyse the distribution of our results in the e - P plane. The left-hand side of Fig. 5.3 shows the distribution of synthetic barium stars computed with standard models, with an accretion efficiency $\alpha_{\text{BH}} = 1.5$. The right-hand side shows the distribution of synthetic barium stars computed with e -enhanced models and accretion parameters $\alpha_{\text{BH}} = 0.1$ and $\beta_{\text{WRL}} = 0.5$. The solid line in all the plots indicates an estimate of the period at which the filling of the Roche lobe occurs at periastron for a given eccentricity. The standard scenario can only explain very few of the highest period systems when the standard tidal dissipation strength, $f_{\text{tid}} = 1$, is assumed (upper-left panel of Fig. 5.3). All systems with a period lower than about 3000 days are expected to be circularised due to the tidal dissipation, which is consistent with the previous findings of Pols et al. (2003). The upper-right panel of Fig. 5.3 shows our results for the same assumption of tidal dissipation strength, $f_{\text{tid}} = 1$, as that of the standard case above, but this time including the eccentricity enhancing mechanism driven by the varying mass-loss rate of the AGB star along the orbit (see §5.2.4). With the inclusion of this mechanism, systems with periods as short as about 1500 days are expected to remain eccentric after the primary leaves the AGB phase, so most of the observed barium-star systems which did not fill their Roche lobes can be reproduced. Some eccentric systems are observed with still shorter periods than

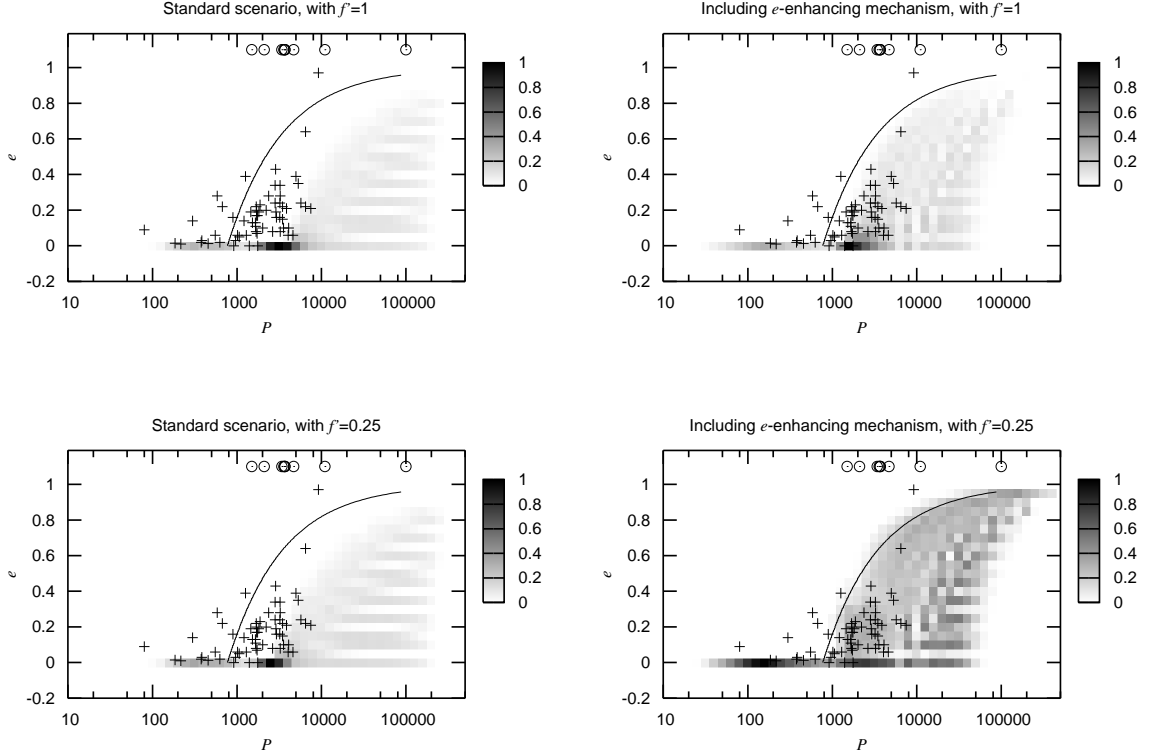


Figure 5.3: Eccentricity-period distribution of synthetic barium-star systems compared to the observations. The left-hand side panels show results calculated with the standard models and the right-hand side panels show the results of the e -enhanced models, each calculated with the indicated tidal dissipation strength f_{tid} . The grey scale is a linear measure of the normalised number distribution of the synthetic barium-star systems over the e - P plane. The crosses are the observational data from the sample of barium stars of Jorissen et al. (1998), which have an error smaller than their symbol. The circles indicate lower limits for the period of systems whose eccentricity is unknown. The solid line indicates an estimated minimum period that a system with a given eccentricity can have without under-going Roche-lobe overflow, calculated for a system with initial primary and secondary masses of $1.5 M_{\odot}$ and $1 M_{\odot}$, respectively, at the moment when the primary is an AGB star with a radius of $300 R_{\odot}$ and a luminosity of $8000 L_{\odot}$, which is representative of the low mass progenitors of barium stars.

those predicted, which suggests that if the tidal dissipation strength is weaker, then the remaining systems are to be explained. The lower-left corner of Fig. 5.3 shows that if $f_{\text{tid}} = 0.25$ is assumed in the standard scenario the situation is hardly improved. This is because of the strong dependence of the circularisation timescale on the separation (see Eq. (5.6)). Thus, to reduce the shorter period limit of eccentric orbits from about 3000 days to about 1000 days the tidal dissipation must be reduced by about a factor of $3^{16/3} = 350$. However, if the same assumption of weaker tides is applied in the e -enhanced models, almost all systems that did not fill their Roche-lobe are reproduced (lower-right panel of Fig. 5.3). In this case the minimum period for eccentric systems is more sensitive to f_{tid} . This arises from the dependence

of the mass-loss rate enhancement on the separation (Eq. (5.1)), which transmits to the eccentricity enhancement in Eq. (5.7) (see also, e.g., Eq. (18) in Chapter 4). Although this weaker choice of the tidal dissipation parameter is able to reproduce the observed properties of barium stars, it predicts many systems with long period and eccentricity larger than 0.5, which are not observed.

Note that in the case of the e -enhanced models, the minimum period expected for an orbit of given eccentricity is close to the estimated period at which a system fills its Roche-lobe. This indicates that there are systems which might have entered a common envelope phase while they were still eccentric.

Enhancement of s -process elements as a function of the period

The distributions of s -process element abundances versus period are almost identical when employing models with different tidal dissipation strength. In Fig. 5.4 we show the results calculated by assuming $f_{\text{tid}} = 1$. We compare our synthetic barium-star results to the observational data gathered by Jorissen et al. (1998), complemented with the data of Allen & Barbuy (2006). Fig. 5.4 shows the distribution of synthetic barium-stars in the $[\text{s}/\text{Fe}]-P$ plane. The

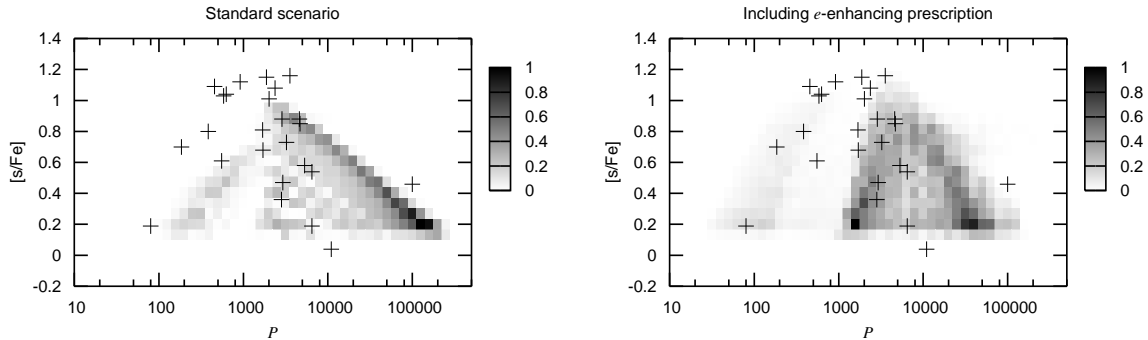


Figure 5.4: Distributions of s -process enhancement as function of period of synthetic barium-star systems compared to the observations. The left-hand side panel shows results calculated with the standard models and the right-hand side panel shows the results calculated with the e -enhanced models. The grey scale is a linear measure of the normalised number distribution of the synthetic barium-star systems over the $[\text{s}/\text{Fe}]-P$ plane. The crosses are observational data of Jorissen et al. (1998), complemented with the data of Allen & Barbuy (2006). The observations have measurement error of about 0.2 dex in the abundances and an error smaller than their symbol in the period.

left panel shows the results of calculations standard models, where the mass-loss rate of an AGB star is that for single stars, $\dot{M}_{\star,w}$, indicated in Sect .5.2.1, with the choice of $\alpha_{\text{BH}} = 1.5$ in order to approximate the maximum observed abundances of s -process elements of about 1.1 dex, as explained in § 5.4.1. The results appear divided into long-period systems, which have periods of about 1500 to 300000 days, and short-period systems, which have periods of

about 20 to 1000 days. The long-period systems have been formed by wind accretion during the whole life-time of the primary as an AGB star. As a result, the further apart are the components the less mass is accreted, which produces the shape of decreasing abundance pattern as the periods are longer. The short-period systems form when the AGB star fills its Roche lobe, which generally leads to a common envelope phase. As part of the energy required to unbind the envelope is taken from the orbit, the orbital period is shortened in an amount which satisfies the energy balance, as explained in § 5.4.1.

The right panel of Fig. 5.4 shows the distribution of synthetic barium-star systems in terms of $[s/Fe]$ and orbital period, calculated with e -enhanced models, assuming $\alpha_{BH} = 0.1$ and $\beta_{WRL} = 0.5$. The results are qualitatively similar to those of calculated with standard models, also showing a division into short-period and long-period systems. As we showed in Sect. 5.4.1, in order to reproduce the observed abundances of the barium stars we have to assume that half of the extra mass lost by the AGB star in the form of wind Roche-lobe overflow is accreted by the companion ($\beta_{WRL} = 0.5$). This makes it easier than in the standard model to explain the observed s -process abundances of barium stars with periods less than 1000 days. A problem faced by both standard and enhanced mass-loss models is the large expected number of systems with periods between 10000 and 100000 days, which are not observed. We will address this point in the next subsection.

Period distribution and overall number of barium stars

To analyse the period distribution of the barium stars and compare it with our models we have binned both our results and the observations in period bins of $\Delta \log P = 0.5$. To compare the different period distributions, we normalise each distribution in such a way that the most abundant bin has a value of 1. The normalised period distributions are shown in Fig. 5.5. When comparing the results of the models to the observations, the obvious problem that arises is the prediction of too many systems with periods larger than 10000 days. This problem could be solved if the accretion was assumed to be less efficient, however, it would not be possible in this case to reproduce the highest observed s -process enhancement in the barium stars, especially those of the short-period systems (see § 5.4.1). The distribution of synthetic systems calculated in the standard circularisation scenario does not change significantly when different values of f_{tid} are assumed (dotted lines). However, Fig. 5.5 shows that a different choice of this parameter affects more significantly the results from the calculations when the eccentricity-enhancing mechanism is assumed. As the tides are weaker, systems that are initially wide and very eccentric do not transfer a significant amount of angular momentum from the orbit to the AGB star. This keeps them from shrinking their orbits and makes them remain highly eccentric, which enhances the number of barium-star binaries expected at longer periods compared to the number expected with a higher value of f_{tid} .

Fig. 5.5 also shows that the number of barium stars with periods of about 100 days is overestimated by the e -enhanced models. On the other hand, the number of barium stars with periods in the 1000 day bin is underestimated by all models. This is related to the apparent gap in Fig. 5.4 around 1000 days between systems that underwent a common-envelope phase

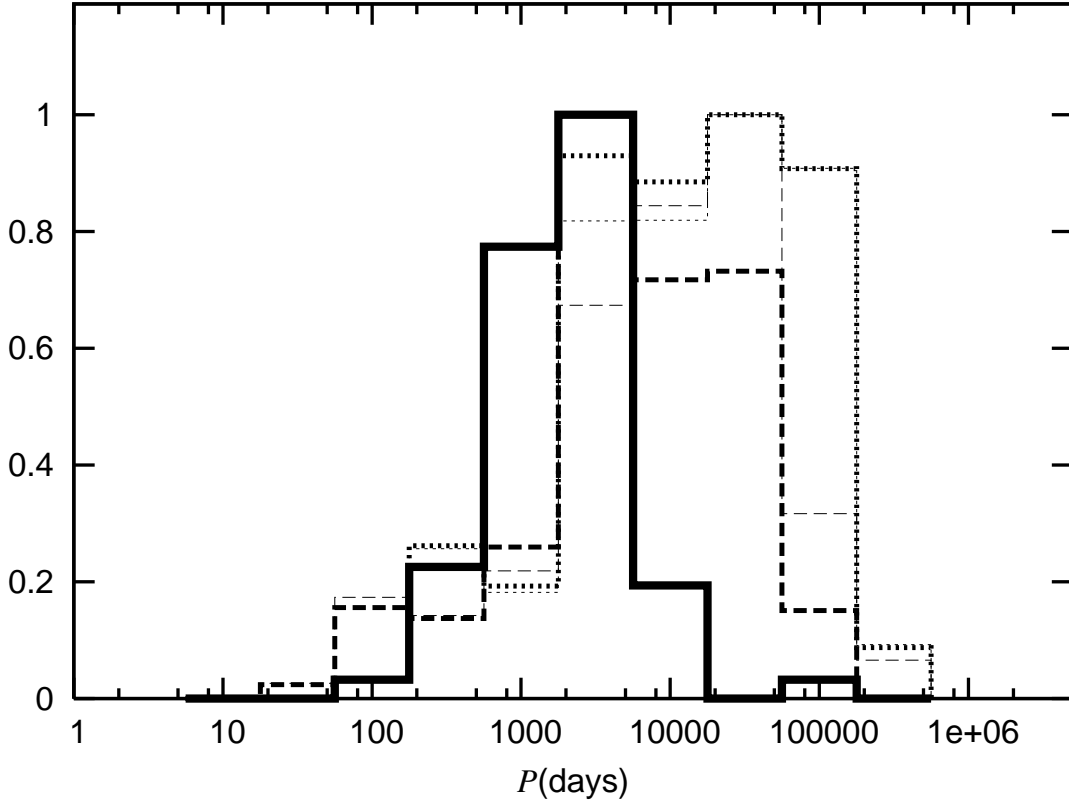


Figure 5.5: Normalised period distribution of synthetic barium-star systems compared to that of the observations. The thick solid line indicates the period distribution of the observed barium-star systems. The dashed lines show the period distribution of the e -enhanced models and the dotted lines show the distribution of the standard models. Both sets of models are calculated by assuming tidal dissipation strength of $f_{\text{tid}} = 1$ (thicker lines) and $f_{\text{tid}} = 0.25$ (thinner lines).

and systems that avoided it. This gap is not seen in the observed distributions. The small number of predicted systems with periods of about 1000 days and the overestimate of systems with shorter periods suggests that less energy loss from the orbit may be required to eject the common envelope (see Sects. 5.2.5 and 5.4.1). This may favour alternative common envelope models based on the balance of angular momentum instead of that of energy (e.g., Nelemans & Tout 2005; van der Sluys et al. 2006).

By integrating over the (non-normalised) period distributions we find that the total number of observed barium stars produced in our models. We divide these by the total number of giants produced in the models (calculated in the same way by weighting all system by their formation probability and by the time they spend on the red giant branch) to find the ratio of the number of barium giants to red giants. This ratio has been deduced from observations to be about 1 per cent. The results are shown in Tab. 5.4.2. The ratios are insensitive to the choice of f_{tid} , but they depend significantly on the assumption for the evolution of the eccentricity. The number of barium stars expected from the models which include the eccentricity-enhancing prescription

Table 5.2: Calculated ratios of number of barium stars to the number of red giants from the models ($N_{\text{Ba}}/N_{\text{RG}}$). f_{binary} indicates the binary fraction required so that 1% of the total red giants is a barium star.

Model #	$N_{\text{RG}}/N_{\text{Ba}}$
1	0.01394
2	0.00866
3	0.01392
4	0.00861

(models 2 and 4) is smaller than that of the models with standard tidal circularisation (models 1 and 3). Because of enhanced mass loss in models 2 and 4, the lower limit of the initial mass of barium-star AGB progenitors is larger. This results in a smaller number of barium stars due to the initial mass function.

These are numbers calculated for a population consisting only of binaries. The observed ratio $N_{\text{Ba}}/N_{\text{RG}}$ of 0.01 is accounted for by the standard models if the binary fraction is about 0.7 (models 1 and 3). However, the $N_{\text{Ba}}/N_{\text{RG}}$ ratio is already lower than 1% for only binaries in the case of the e -enhanced models (models 2 and 4).

5.5 Conclusions and discussion

We have carried out a population synthesis study of barium-star binaries to test if the observed distributions of periods, eccentricities and s -process enhancements of barium stars can be reproduced by binary evolution models. We reaffirm the findings of Pols et al. (2003) who show that under the standard assumptions of tidal dissipation systems with periods shorter than about 3500 days cannot remain eccentric. We also show that the situation is hardly improved by lowering the strength of tidal dissipation within a reasonable range. Bonačić Marinović et al. (2007b) In Chapter 4 we propose an eccentricity-enhancing mechanism based on an enhanced and variable mass loss rate and mass transfer rate during the AGB phase of the primary component. We test the effect of this mechanism on the formation and evolution of barium-star binaries in our population synthesis models. We find that with the inclusion of the eccentricity-enhancing prescription, the eccentricities of most of the observed barium-star systems which did not fill their Roche lobes are reproduced if we assume a standard value for the tidal dissipation strength, $f_{\text{tid}} = 1$.

Due to the strong circularisation in the standard scenario of binary evolution, it is not possible that a system fills its Roche lobe while the orbit is still eccentric. However, if the eccentricity enhancement mechanism is taken into account, some systems can remain eccentric by the time Roche-lobe overflow takes place, especially if a lower tidal strength ($f_{\text{tid}} = 0.25$)

is considered. Our treatment of common-envelope evolution prevents any barium-star binary from remaining eccentric after filling its Roche lobe and entering a common envelope phase. Therefore we cannot reproduce the eccentric barium-star systems with periods shorter than about 1000 days. However, we envisage that a similar eccentricity enhancing mechanism could take place during the common-envelope phase if a system enters the common envelope phase while its orbit is still eccentric and mass ejection of the common envelope takes place preferentially at periastron passages (e.g., Soker 2000). In this way eccentric systems with periods shorter than about 1000 days might also be accounted for.

Our model results show a gap in the period distribution of barium stars around $P \sim 1000$ days, which is not observed. This suggests that systems that entered a common-envelope phase did not experience a significant shrinkage of their orbits, and that the assumed scenario of common envelope evolution overestimates the orbital energy required to eject the envelope. Within the context of our models we may account for this to some extent by assuming a larger contribution of the ionisation energy of the envelope in the energy balance of the common-envelope phase. However, an alternative common-envelope evolution scenario that considers the balance of angular momentum instead of that of energy (e.g., Nelemans et al. 2000; Nelemans & Tout 2005; van der Sluys et al. 2006) may be better able to account for the low number of very short-period systems observed.

A common feature in all model sets that we calculated, both with and without including the eccentricity-enhancing prescription, is an overproduction of systems with periods longer than 10000 days compared to the observed sample. The observational sample is complete only for the strong barium stars, but is incomplete for the mild barium stars (Jorissen et al. 1998). It is hard to distinguish between strong and mild barium stars in our synthetic models, because there appears to be no strong correlation between this classification and the measured *s*-process enhancements. Nevertheless, the number of systems with undetermined orbits that may have periods longer than 10000 days is relatively small. Therefore, assuming that the sample of observed barium stars that we employ in this chapter is representative, we may conclude that the accretion at long periods must be less efficient than assumed.

Alternatively, the discrepancy may point towards an underestimate of the amount of angular momentum lost from the binary system during the wind mass-loss phase of the AGB star. Our models assume that the wind is isotropic and the angular momentum it carries is that of the orbit of the AGB star. However, hydrodynamical simulations by Jahanara et al. (2005) indicate that the actual amount of angular momentum loss may be substantially larger if the wind velocity is comparable to or smaller than the orbital velocity. The effect of a stronger angular momentum loss on the formation of barium stars deserves further investigation.

Appendix A

Details of the synthetic TP-AGB model

Hurley et al. (2000, hereafter H00) have developed a comprehensive synthetic evolution code for single stellar evolution, based on detailed models of Pols et al. (1998, hereafter P98). The P98 models include convective core overshooting, but do not undergo thermal pulses during the AGB phase. To model TP-AGB stars, H00 apply the same luminosity–core mass relation as in the early (E-) AGB phase. The TP-AGB section of the H00 code was improved by Izzard et al. (2004, hereafter I04) with a synthetic code based on the detailed model calculations by Karakas et al. (2002, hereafter K02) that undergo thermal pulses. The latest version (Izzard et al. 2006) also follows the nucleosynthesis of many *s*-process isotopes based on the models of Gallino et al. (1998).

However, unlike the P98 detailed models, the K02 detailed models do not include convective overshooting. This means that the transition from the E-AGB to the TP-AGB phase is not self-consistent in the I04 code, leading to discontinuities in the evolution of the stellar core mass, of the luminosity, and of the radius of the AGB star. To overcome these problems, we have made modifications to the I04 code, which are explained in detail below.

A.1 TP-AGB initial H-depleted core mass

For an AGB star to enter the TP-AGB phase, its helium intershell mass must be small enough to undergo a flash. This occurs at the end of the E-AGB phase when the helium-burning shell almost reaches the hydrogen-burning shell. In our code the H-depleted core mass at the beginning of the TP-AGB phase, $M_{c,1TP}$, is given by the mass of the H-depleted core at the base of the AGB, $M_{c,BAGB}$. However, stars with $M_{c,BAGB} \sim 0.8M_{\odot}$ and larger undergo second dredge-up by the end of the E-AGB phase, which makes $M_{c,1TP} < M_{c,BAGB}$.

When convective overshooting is taken into account, the value of $M_{c,1TP}$ for a star with a given initial mass is higher than that of a star with the same initial mass without overshooting. The effects of overshooting become important in AGB stars of $M \gtrsim 2.5M_{\odot}$ ¹, having a direct

¹The effects of overshooting are also strong in lower-mass stars on the main sequence and the horizontal

impact on the subsequent evolution.

We have improved the linear relation between $M_{c,BAGB}$ and $M_{c,1TP}$ from H00 (denoted as $M_{c,DU}$ in that paper) with a quadratic one, based on data from the P98 models (hereafter OV):

$$M_{c,1TP,OV} = 9.292 \times 10^{-2} M_{c,BAGB} \times (M_{c,BAGB} + 1.983) + 5.865 \times 10^{-1}, \quad (\text{A.1})$$

in solar units. This fit is not very good for stars with $M \lesssim 1.5M_{\odot}$, but in these the effects of

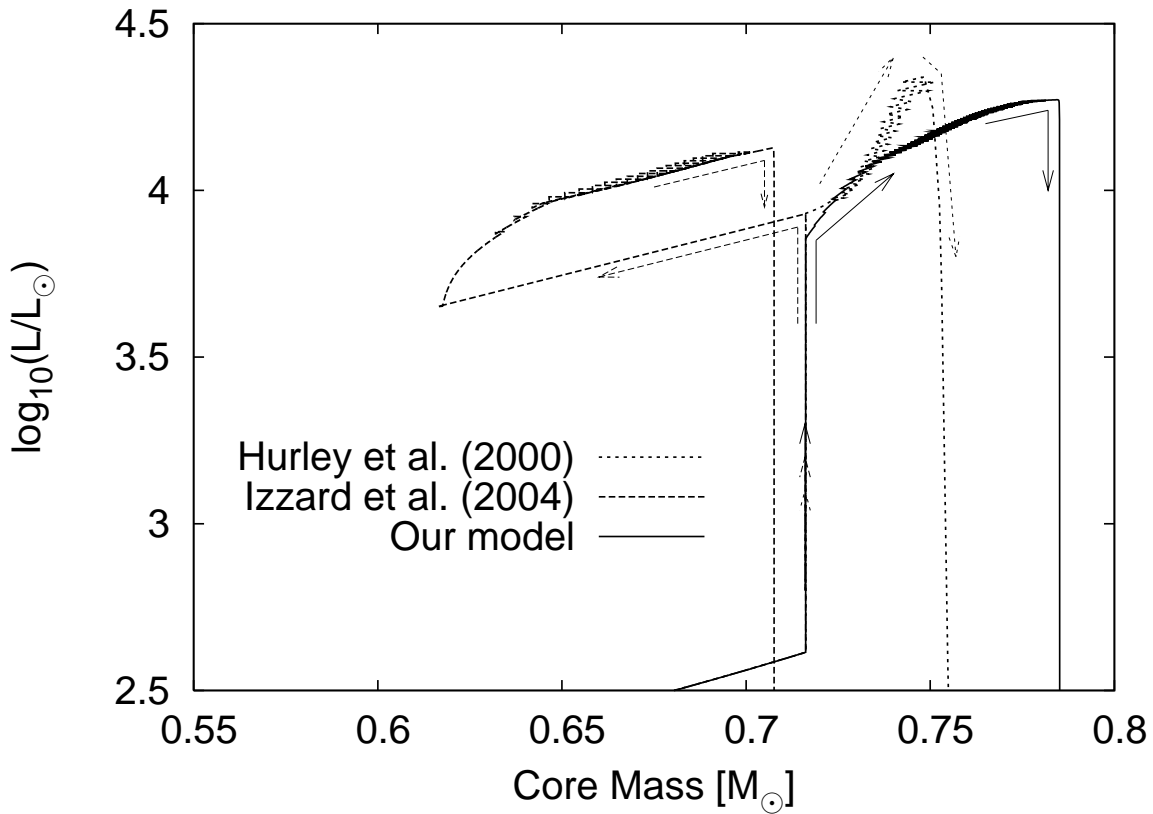


Figure A.1: Luminosity–core mass relation of a $3 M_{\odot}$ star with metallicity $Z = 0.01$. The arrows show the way in which the core evolves in time. During the E-AGB phase, the hydrogen-exhausted core mass remains constant at $0.716 M_{\odot}$. In our model the core mass at the start of the TP-AGB is the same as in the H02 model, which is greater than in the I04 model.

overshooting become negligible and the fit to the K02 models ($M_{c,1TP,K02}$) is appropriate, so we instead use

$$M_{c,1TP} = \max \left[\min(M_{c,1TP,OV}, M_{c,BAGB}), M_{c,1TP,K02} \right]. \quad (\text{A.2})$$

branch phase, but are largely wiped out during the red giant branch phase (Pols et al. 1998).

Fig. A.1 shows a luminosity–core mass plot where the core-mass prescriptions of the different synthetic models can be compared.

A.2 CO core mass and luminosity on E-AGB phase

As in H00, we model the luminosity during the E-AGB phase with a power-law relation of the form $L_{E-AGB} = l_1 M_{CO}^{l_2}$, where M_{CO} is the mass of the CO core during the E-AGB phase. The coefficients l_1 and l_2 are found from the values of L_{E-AGB} and M_{CO} at the beginning and at the end of the E-AGB phase.

For the beginning we use Eq. (56) from H00 for the luminosity at the base of the AGB and the following relation for M_{CO} at the base of the AGB

$$M_{CO,BAGB} = (a_1 M^{a_2} + a_3)^{0.25}, \quad (\text{A.3})$$

which fits the data from the P98 detailed models, expressed in solar units. The coefficients

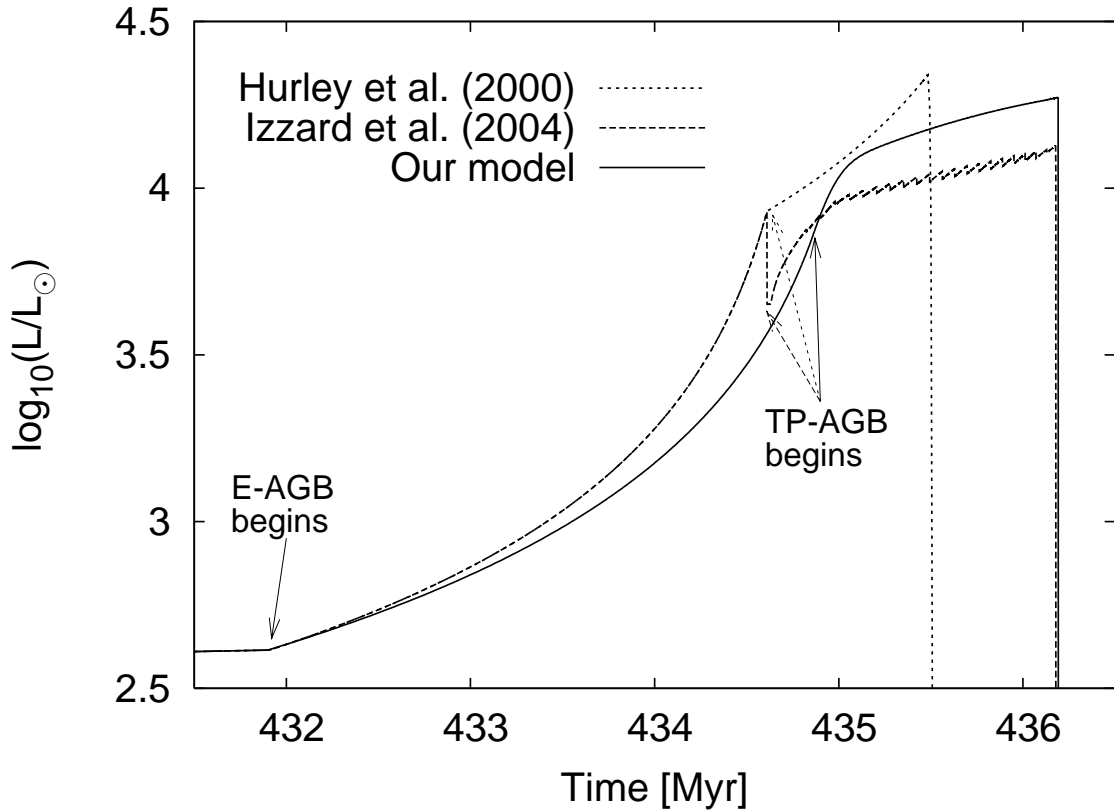


Figure A.2: Evolution of luminosity in time of the same star as in Fig. A.1. The E-AGB evolution is slightly modified in our model and the discontinuity in luminosity is fixed.

Table A.1: Coefficients $a_{i,j}$ for Eq. (A.4).

$a_{i,j}$	$j = 1$	$j = 2$	$j = 3$	$j = 4$
$i = 1$	1.287×10^{-5}	-3.709×10^{-5}	6.535×10^{-5}	1.607×10^{-5}
$i = 2$	5.881	8.617×10^{-1}	3.410×10^{-1}	6.039×10^{-2}
$i = 3$	4.878×10^{-3}	-1.764×10^{-4}	1.986×10^{-3}	6.635×10^{-4}

depend on metallicity and are calculated with the formula

$$a_i = a_{i,1} + [\text{Fe}/\text{H}](a_{i,2} + [\text{Fe}/\text{H}](a_{i,3} + [\text{Fe}/\text{H}]a_{i,4})), \quad (\text{A.4})$$

where $a_{i,j}$ are the dimensionless coefficients listed in Table A.1.

For a smooth transition to the TP-AGB phase, we require

$$M_{\text{CO, end}} = M_{\text{c, 1TP}} \quad \text{and} \quad L_{\text{E-AGB, end}} = L_{1\text{TP}}, \quad (\text{A.5})$$

where $M_{\text{CO, end}}$ and $L_{\text{E-AGB, end}}$ are the CO core mass and the luminosity at the end of the E-AGB phase, respectively. The luminosity at the beginning of the TP-AGB phase, $L_{1\text{TP}}$, is discussed in §A.3. A comparison between the time evolution of the luminosity described by the different synthetic models is shown in Fig. A.2.

A.3 Luminosity during the TP-AGB phase

Following Paczyński (1970), it has become the usual practice to apply a linear luminosity–core mass relation in synthetic AGB models. However, this relation fails in the presence of dredge-up and hot bottom burning. This becomes a problem when comparing models that include overshooting to models that do not: two TP-AGB stars with the same core mass, but different envelope mass, do not behave in the same way. To overcome this we designed a luminosity relation that depends on both the core mass and the envelope mass of the star. It successfully reproduces both the P98 models that include overshooting and models calculated with the same code used by P98, which do not include overshooting. Stancliffe et al. (2004, hereafter S04) employed a modified version of the code used by P98 and computed detailed models that do not include overshooting, but do undergo thermal pulses. In an attempt to make our rapid TP-AGB models more self-consistent, we have modified our luminosity relation to fit the S04 models, assuming that with the inclusion of overshooting the S04 models are modified in the same way as those of P98. In addition to this, we find that in the presence of third dredge-up the results of the detailed stellar evolution models are better represented by relating

the luminosity to $M_{c,\text{NODUP}}$, the core mass as it would be in the absence of dredge-up:

$$\begin{aligned} \log_{10}(L_{c,\text{NODUP}}) = & \left(\log_{10}(15300 + 9440Z) \right. \\ & \left. + \frac{3.45 \log_{10}(M_{c,\text{NODUP}} + 0.1)}{3M_{c,\text{NODUP}} - M_{c,\text{1TP}}} \right) \\ & \times \left(\frac{M_{c,\text{1TP}}}{M_{c,\text{NODUP}}} \right)^{0.045} + 0.08, \end{aligned} \quad (\text{A.6})$$

in solar units and where Z is the metallicity. In stars with a massive convective envelope ($M_{\text{env}} \gtrsim 2.5 M_{\odot}$), the temperature at the bottom of the envelope is high enough for hot bottom burning (HBB), which enhances the luminosity of the star by a factor f_{HBB} due to the enhanced hydrogen abundance in the H-burning shell. The expression

$$\begin{aligned} \log_{10}(f_{\text{HBB}}) = \max \left\{ 1.3 \log_{10} \left[\frac{M_{\text{env},\text{1TP}}(1 - 0.53 [\text{Fe}/\text{H}])}{M_{\text{env},\text{HBB}}} \right] \right. \\ \left. - 0.08, 0 \right\} \end{aligned} \quad (\text{A.7})$$

fits $f_{\text{HBB}} \times L_{c,\text{NODUP}}$ to the luminosity of the S04 models, where $M_{\text{env},\text{1TP}}$ is the mass of the envelope at the beginning of the TP-AGB, and we set the threshold mass for the onset of HBB $M_{\text{env},\text{HBB}} = 2.4 M_{\odot}$.

The S04 models have no mass loss, so we have to use a different set of models to fit the behaviour of the luminosity in terms of the loss of the envelope mass. Based on the K02 models, the contribution of the envelope to the luminosity can be modelled as

$$\begin{aligned} \log_{10}(f_{\text{env}}) = \max \left\{ \log_{10}(f_{\text{HBB}}) + \right. \\ \left. 0.46 \min \left[\log_{10} \left(\frac{M_{\text{env}}}{M_{\text{env},\text{1TP}}} \right), 0 \right], 0 \right\}. \end{aligned} \quad (\text{A.8})$$

The expression $f_{\text{env}} \times L_{c,\text{NODUP}}$ matches the asymptotic behaviour of the luminosity observed in the S04 detailed models, which is reached after several pulses. To model the first few pulses, we write the luminosity as

$$L = \left[\frac{L_{c,\text{NODUP}} \times f_{\text{env}}}{L_{\text{TP1}}} \right]^f L_{\text{TP1}}, \quad (\text{A.9})$$

where L_{TP1} is fitted to the S04 models with the expression

$$\log_{10}(L_{\text{TP1}}) = -1.8427 M_{c,\text{TP1}}^2 + 5.3861 M_{c,\text{TP1}} + 0.97823, \quad (\text{A.10})$$

and

$$f = 1 - \left[1 - \frac{M_{c,\text{NODUP}} - M_{c,\text{1TP}}}{0.075} \right]^{25/3} \quad (\text{A.11})$$

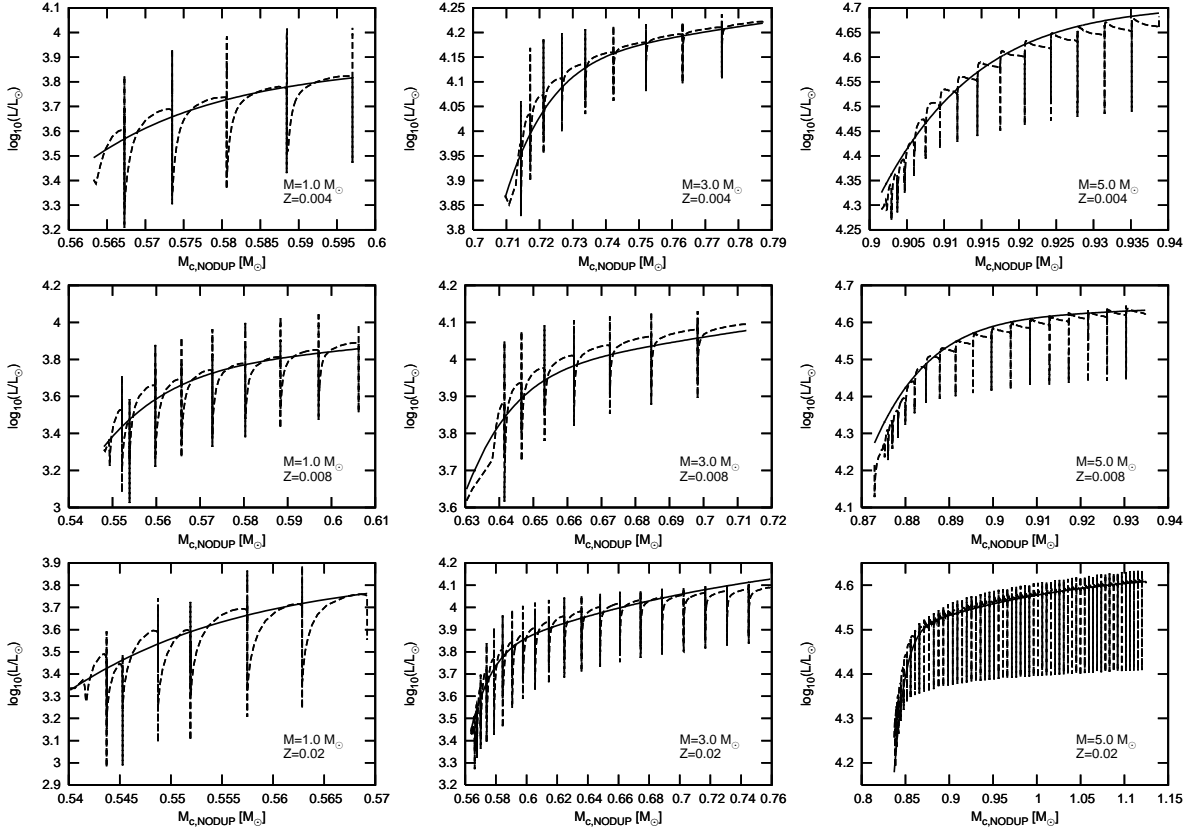


Figure A.3: Examples of our analytic fit (solid lines) compared to the data from the detailed models (dashed lines) from Stancliffe et al. (2004) for different stellar masses and metallicities, as indicated in the panels.

accounts for the luminosity growth during the early pulses to its asymptotic value $L_{c,NODUP} \times f_{env}$. In Eqs. (A.10) and (A.11), all quantities are expressed in solar units. Figure A.3 shows a comparison between our fit and the S04 detailed models. In the worst cases, our fits have an error smaller than 10% in luminosity, which is less than the difference between the S04 and K02 detailed models.

A.4 Radius during TP-AGB phase

We use the H00 radius-luminosity relation, given that it accurately fits the S04 models, but we have modified the interpolation procedure slightly. The H00 radius-luminosity relation (Eq. (74) in that paper) was designed to fit the P98 models at seven different metallicities in the following way:

$$R_{AGB} = A(L^{b_1} + b_2 L^{b_3}), \quad (\text{A.12})$$

where L is the luminosity, A depends on the mass and b_i , on the metallicity. For intermediate metallicities the radius was calculated after interpolating linearly in Z between the coefficients

that fit these seven metallicities. Some of these coefficients are exponents, and we found the results for interpolated metallicities to behave erratically. We therefore interpolate linearly in Z between the radius values calculated with Eq. A.12 for the adjacent known metallicities, which is in much better agreement with detailed models at intermediate metallicities calculated with the same code as used by P98.

Appendix B

Derivation of variation of orbital parameters

The orbit of a binary star system can be described by the eccentricity e and the semi-major axis a . The change in these orbital parameters can be related to changes in the masses $M_{1,2}$ of the two stars, either due to mass loss or mass accretion, through the conservation laws for the total orbital energy E_{orb} and the orbital angular momentum J_{orb} , given by

$$E_{\text{orb}} = -\frac{GMm}{2a}, \quad (\text{B.1})$$

and

$$J_{\text{orb}}^2 = m^2 r^4 \omega^2 = GMm^2 a(1 - e^2). \quad (\text{B.2})$$

Here ω is the instantaneous angular velocity, r is the instantaneous separation among the system components, $M = M_1 + M_2$ is the total mass and $m = M_1 M_2 / M$ is the reduced mass of the system. The variations of the orbital parameters a and e are then given by

$$\frac{\delta a}{a} = \frac{\delta M}{M} + \frac{\delta m}{m} - \frac{\delta E_{\text{orb}}}{E_{\text{orb}}} \quad (\text{B.3})$$

and

$$\frac{\delta(1 - e^2)}{1 - e^2} = 2 \frac{\delta J_{\text{orb}}}{J_{\text{orb}}} + \frac{\delta E_{\text{orb}}}{E_{\text{orb}}} - 2 \frac{\delta M}{M} - 3 \frac{\delta m}{m}. \quad (\text{B.4})$$

In the following we will derive expressions for δE_{orb} and δJ_{orb} .

B.1 Variation of the Orbital Energy

The total orbital energy is the sum of the kinetic energy and the gravitational energy,

$$E_{\text{orb}} = \frac{1}{2} m v^2 - \frac{GM_1 M_2}{r}, \quad (\text{B.5})$$

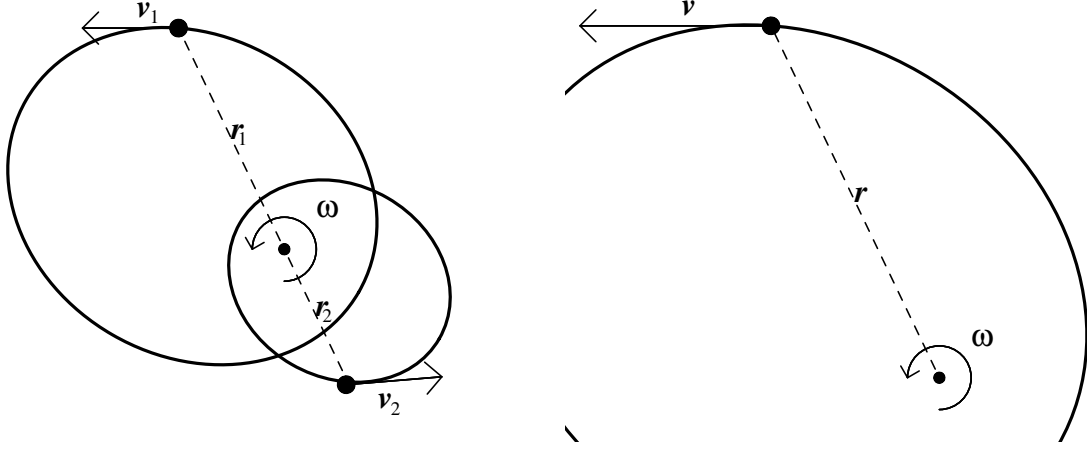


Figure B.1: The geometric relation between the positions and velocities of both components in a binary system (left) and the equivalent reduced mass problem (right).

where $r = |\vec{r}_1 - \vec{r}_2|$ is the instantaneous distance between the two stars and $\vec{v} = \vec{v}_1 - \vec{v}_2$ is their relative velocity (see Fig. B.1). The variation of (B.5) is given by

$$\delta E_{\text{orb}} = \frac{1}{2} m v^2 \left(\frac{\delta m}{m} + \frac{\delta(v^2)}{v^2} \right) - \frac{GMm}{r} \left(\frac{\delta M}{M} + \frac{\delta m}{m} - \frac{\delta r}{r} \right). \quad (\text{B.6})$$

The velocity \vec{v} has components v_r and $v_\theta = r\omega$ in polar coordinates, so that the variation of $\delta(v^2)$ can be written as

$$\delta(v^2) = 2v_r \delta v_r + 2r\omega(r\delta\omega + \omega\delta r). \quad (\text{B.7})$$

For later use, we will need to know the variation in terms of the variations for the individual components,

$$\delta(v^2) = 2v_r \delta v_{r,1} + 2r\omega(r_1 \delta\omega + \omega \delta r_1) + (1 \Leftrightarrow 2). \quad (\text{B.8})$$

The notation $+(1 \Leftrightarrow 2)$ means: add terms to the left again with indexes 1 and 2 interchanged. Note that this is an addition despite \vec{v} being defined as the difference $\vec{v}_1 - \vec{v}_2$. The reason is that contrary to a Cartesian basis the direction of basis vectors in polar coordinates is not fixed but depends on the angular coordinate θ .

We will consider two effects that change the mass of each star: Bondi-Hoyle accretion (Bondi & Hoyle 1944) and isotropic mass loss. The latter does not affect the velocity of the star relative to the centre of mass, but the former does. Let $\delta M_1 = \delta M_{1,\text{ACC}}$ denote the mass accreted by star 1 and let \vec{w}_{21} be the velocity of the wind of star 2 at the moment it is accreted by star 1 and \vec{w}_{12} vice versa. Then conservation of momentum gives

$$M_1 \delta \vec{v}_1 = (\vec{w}_{21} - \vec{v}_1) \delta M_{1,\text{ACC}} \quad (\text{B.9})$$

and similar for star 2. Inserting this in (B.8) gives the relation

$$\delta(v^2) = 2\vec{v} \cdot (\vec{w}_{21} - \vec{v}_1) \frac{\delta M_{1,\text{ACC}}}{M_1} + (1 \Leftrightarrow 2). \quad (\text{B.10})$$

It now remains to express δM and δm in terms of the variation of the individual masses δM_1 and δM_2 . For the purpose of bookkeeping we split the mass lost from star 1 (and similarly for star 2) into two parts: the amount $\delta M_{1,LOST}$ that is lost from the system and the amount $\delta M_{2,ACC}$ that is eventually accreted by star 2. Then

$$\delta M_1 = -\delta M_{1,LOST} - \delta M_{2,ACC} + \delta M_{1,ACC} \quad (\text{B.11})$$

and

$$\delta M_2 = -\delta M_{2,LOST} - \delta M_{1,ACC} + \delta M_{2,ACC}. \quad (\text{B.12})$$

The variation of the total mass δM is just $\delta M_1 + \delta M_2$ while the variation of the reduced mass is

$$\frac{\delta m}{m} = -\frac{\delta M_{1,LOST}}{M_1} \frac{M_2}{M_1 + M_2} + \frac{\delta M_{1,ACC}}{M_1} \left(1 - \frac{M_1}{M_2}\right) + (1 \Leftrightarrow 2). \quad (\text{B.13})$$

If the transfer of momentum due to the wind is instantaneous the distance r between the two stars is not changed, hence $\delta r = 0$. Inserting (B.8), (B.11), (B.12) and (B.13) into (B.6) then gives

$$\begin{aligned} \frac{\delta E_{\text{orb}}}{E_{\text{orb}}} = & \frac{\delta M_{1,ACC}}{M_1} \left[1 - \frac{M_1}{M_2} - \frac{2a}{G(M_1 + M_2)} \vec{v} \cdot (\vec{w}_{21} - \vec{v}_1) \right] \\ & - \frac{\delta M_{1,LOST}}{M_1} \left[1 + \left(\frac{2a}{r} - 1 \right) \frac{M_1}{M_1 + M_2} \right] + (1 \Leftrightarrow 2) \end{aligned} \quad (\text{B.14})$$

which is the same as (4.8).

B.2 Variation of the Orbital Angular Momentum

The variation of the orbital angular momentum (B.2) is

$$\frac{\delta J_{\text{orb}}}{J_{\text{orb}}} = \frac{\delta m}{m} + \frac{\delta r}{r} + \frac{\delta v_{\theta}}{v_{\theta}}, \quad (\text{B.15})$$

where as before $v_{\theta} = r\omega$. Using (B.9), (B.13) and the fact that r does not depend on the variation of the two masses immediately gives

$$\begin{aligned} \frac{\delta J_{\text{orb}}}{J_{\text{orb}}} = & \frac{\delta M_{1,ACC}}{M_1} \left(1 - \frac{M_1}{M_2} + \frac{w_{\theta,21} - r_1\omega}{r_1\omega} \right) \\ & - \frac{\delta M_{1,LOST}}{M_1} \frac{M_2}{M_1 + M_2} + (1 \Leftrightarrow 2) \end{aligned} \quad (\text{B.16})$$

which is the same as (4.7).

B.3 The Variation of the Semi-Major Axis

The variation of the eccentricity that results from the above considerations is given in (4.11) in the text. For completeness we here give the corresponding expression for the variation in a . Inserting (B.14) and (B.13) in (B.3) we obtain

$$\begin{aligned} \frac{\delta a}{a} = & \frac{\delta M_{1,\text{ACC}}}{M_1} \frac{2a}{G(M_1 + M_2)} \vec{v} \cdot (\vec{w}_{21} - \vec{v}_1) + \\ & + \frac{\delta M_{1,\text{LOST}}}{M_1} \frac{M_1}{M_1 + M_2} \left(\frac{2a}{r} - 1 \right) + (1 \Leftrightarrow 2). \end{aligned} \quad (\text{B.17})$$

Samenvatting

De meeste elementen op aarde die zwaarder zijn dan ijzer, zoals bijvoorbeeld barium en cesium, worden gemaakt wanneer de kern van een ijzeratoom bloot wordt gesteld aan neutronen. Wanneer de neutronen door de kern worden ingevangen, vervallen ze tot protonen, waardoor zwaardere elementen ontstaan. Als het verval van de neutronen sneller plaats vindt dan het tempo waarmee neutronen worden ingevangen dan spreekt men van langzame neutronen vangst, vaak aangeduid als s-proces, waarbij s staat voor slow. De elementen die op deze manier gemaakt worden, noemt men s-proces elementen. Dit zijn elementen zoals bijvoorbeeld strontium, dat onder andere gebruikt wordt bij stralingstherapie tegen kanker, yttrium, de stof die zorgt voor de rode kleur op televisie beeldschermen, zirkonium, verwerkt in sieraden en als warmte isolerende stof, cesium, dat in de olieindustrie toegepast wordt in boorvloeistoffen en ook in atomaire klokken, barium, dat gebruikt wordt voor Röntgenfoto's en in rattengif, lanthaan, toegepast in lampen en cerium, gebruikt in aluminium legeringen.

Al deze elementen worden gemaakt in zogenaamde AGB sterren, wat een afkorting is voor Asymptotic Giant Branch, ofwel asymptotische reuzentak. Deze sterren zijn honderden malen groter dan de zon en enkele tienduizenden malen helderder. Ze bevinden zich in het laatste stadium van hun evolutie, voordat ze hun leven zullen eindigen als een langzaam afkoelende witte dwerg. Van binnen hebben ze een uiachtige structuur: in het centrum bevindt zich een compacte kern, bestaande uit koolstof en zuurstof met daarom heen een omvangrijke mantel van waterstof. Tussen de mantel en de kern ligt een schil die bestaat uit voornamelijk helium. Men denkt dat de s-proces elementen in deze schil gevormd kunnen worden. Hiervoor zijn veel neutronen nodig. ^{13}C is een isotoop dat deze neutronen kan leveren. Het is echter niet duidelijk hoeveel ^{13}C gevormd wordt in de dunne schil tussen de kern en de mantel van AGB sterren. Ook de fysica van AGB sterren is nog grotendeels onzeker. Waarnemingen van s-proces elementen op de oppervlakte van deze sterren kunnen gebruikt worden om de theoretische modellen te testen en de vrije parameters in deze modellen te ijken.

In deel I van dit proefschrift beschrijven we hoe we het probleem van de vorming van s-proces elementen aanpakken door kunstmatige populaties van sterren te construeren uit sterevolutiemodellen. Elke populatie wordt geconstrueerd door verschillende waarden aan te nemen voor de vrije parameters in de modellen. Door de kunstmatige populaties te vergelijken met waargenomen populaties AGB sterren kunnen de waarden van de parameters bepaald worden die de werkelijkheid het beste beschrijven.

In hoofdstuk 2 vergelijken we de kunstmatige populaties met waarnemingen van sterren

met een verhoogde hoeveelheid *s*-proces elementen. Hiermee stellen we grenzen aan de waarden voor vrije parameters, die het fysische proces beschrijven dat de *s*-proces elementen van de schil naar de mantel mengt, en de vrije parameters die de eigenschappen van de neutronen bron ^{13}C beschrijven. We stellen vast dat de hoeveelheid ^{13}C die effectief bijdraagt aan de productie van *s*-proces elementen afneemt met het metaalgehalte van de ster, waarbij het metaal gehalte wordt bepaald als de verhouding van ijzer en waterstof. Bovendien kunnen we de waarden voor deze vrije parameter beperken binnen een factor vier, wat veel strikter is dan wat tot nu toe bekend was, namelijk een factor 25. Verder vinden we dat het mengen van *s*-proces elementen van de schil naar de mantel altijd efficiënt is en dat het in sterren met lagere massa's moet plaatsvinden dan wat tot nu toe door theoretische modellen voorspeld werd.

Het werk in hoofdstuk 2 is uitgevoerd door sterren in ons eigen melkwegstelsel te bestuderen. In hoofdstuk 3 analyseren we het extragalactisch object MACHO 47.2496.8 dat zich in de Grote Magelhaanse Wolk bevindt. Dit object is tot nu toe de enige ster buiten onze melkweg, waarvan gegevens bekend zijn over de *s*-proces elementen die betrouwbaar genoeg zijn voor onze studie. We concluderen dat de vrije parameters in ons model die geijkt zijn aan galactische sterren ook in overeenstemming zijn met MACHO 47.2496.8. Dit bevestigt onze eerdere conclusie dat objecten met een laag metaalgehalte, een kleinere hoeveelheid ^{13}C hebben. Ook al zijn meer gegevens van extragalactische sterren nodig om onze conclusies te versterken, het feit dat onze resultaten voor een extra-galactisch object consistent zijn met die van objecten in de Melkweg suggereert dat onze bevindingen een universeel karakter hebben.

Deel II gaat in op de baanparameters van dubbelsterren met een voormalige AGB ster. Dit soort systemen wordt waargenomen als een dubbelster bestaande uit een witte dwerg, die voorheen een AGB ster was, en een tweede ster die nog minder ver geëvolueerd is. Op het oppervlakte van de tweede ster worden *s*-proces elementen waargenomen. Hierdoor denkt men dat overdracht van massa heeft plaatsgevonden, toen de eerste ster nog een AGB ster was. Veel van dit soort systemen zijn vrij nauw: de afstand tussen de twee sterren is vergelijkbaar met de afmetingen die de eerste ster voorheen had als AGB ster. Dit betekent dat de getijdenwerking zo sterk moet zijn geweest, dat een significant deel van de energie van de baan verloren moet zijn gegaan. Een consequentie hiervan is dat als de baan voorheen elliptisch was, deze door de getijdenwerking cirkelvormig moet zijn geworden. Echter, veel van deze relatief nauwe systemen zijn ellipsvormig. Een voorbeeld van deze systemen is Sirius, een dubbelstersysteem dat te zien is als de helderste ster aan de nachtelijke hemel en waarvan de begeleider een witte dwerg is. De baan van Sirius is excentrisch: als de sterren elkaar het dichtst benaderen is de afstand tussen hen vier keer korter dan wanneer de sterren het verst uit elkaar staan. Dit is niet te verklaren in het licht van de getijdenmechanismen die energie dissiperen. Het doet vermoeden dat er een andere mechanisme bestaat dat de excentriciteit van een baan kan verhogen.

AGB sterren verliezen veel massa en ze hebben een uitgestrekte mantel, die makkelijk vervormd kan worden door de zwaartekracht van de begeleidende ster. In hoofdstuk 4 stellen we een model voor om de ellipsvormige dubbelster systemen te verklaren. In dit model nemen we aan dat het massaverlies van AGB sterren wordt versterkt door de nabijheid van de tweede ster. Op deze manier verliest een AGB ster in een systeem met een elliptische baan meer

materie wanneer de begeleider dichtbij is dan wanneer hij ver weg staat. Dit ongelijkmatige massaverlies zorgt ervoor dat de baan excentrischer wordt en gaat daarmee dus in tegen het effect van de getijdenwerking, die de baan cirkelvormiger maken. Door dit model toe te passen laten we zien dat we de excentrische baan van Sirius kunnen verklaren evenals de banen van andere systemen, die tot nu toe niet verklaard konden worden.

In hoofdstuk 5 passen we ons model toe op systemen met bariumsterren. Dit zijn sterren waarbij een verhoogde hoeveelheid s-proces elementen wordt gemeten, met name het element barium. Ze worden gevonden in dubbelsterren, waarbij de begeleidende ster een witte dwerg is. Dit geeft aan dat het barium waarschijnlijk afkomstig is van de begeleidende ster, uit de tijd dat deze nog een AGB ster was. De baanperiodes van dit soort systemen variëren van 80 tot 10.000 dagen. De huidige standaardmodellen voor de evolutie van dubbelsterren kunnen niet verklaren waarom sommige systemen met baanperiodes korter dan 3.000 dagen ellipsvormig zijn. We creëren een kunstmatige populatie van bariumsterren en we vergelijken deze met de waargenomen populatie. Als we redelijke aannames doen voor de vrije parameters kunnen we bijna alle systemen verklaren met baanperiodes tussen de 1000 en 3000 dagen. De systemen met periodes korter dan 1000 dagen, hebben tijdens hun evolutie een fase van hevige massaoverdracht ondergaan. Daarom laten we ze hier buiten beschouwing. In onze modellen produceren we echter te veel systemen met periodes groter dan 10000 dagen in vergelijking met de waarnemingen. Dit zou er op kunnen wijzen dat massaoverdracht in wijde systemen minder efficiënt is dan wordt aangenomen.

Resumen

La mayoría de los elementos en la Tierra más pesados que el hierro se forman cuando núcleos de hierro son expuestos a neutrones. Los neutrones son atrapados por los núcleos de hierro y decaen en protones, transformándose el hierro en elementos más pesados. Si el decaimiento ocurre más rápido que la tasa de captura de neutrones, entonces se llama proceso de captura lenta de neutrones (*s*-process, del inglés “slow process”, que significa proceso lento) y los elementos formados mediante este mecanismo se llaman elementos *s*-process. Éstos se utilizan en la Tierra en forma diaria, como el estroncio (e.g., terapia de radiación contra el cáncer), el ytrio (e.g., el color rojo en la TV), el zirconio (e.g., la circonita cúbica en joyería, protector en barreras térmicas), el cesio (e.g., lubricante para taladros en la industria del petróleo, relojes atómicos), el bario (e.g., imágenes de rayos X, veneno para ratas), el lantano (e.g., aplicaciones de iluminación), el cerio (e.g., aleaciones de aluminio), entre otros. La principal fábrica de estos elementos en el Universo son las estrellas AGB, acrónimo del inglés “Asymptotic Giant Branch” y que se traduce como rama gigante asintótica. Estas estrellas son cientos de veces más grandes que el Sol en diámetro y decenas de miles de veces más luminosas que nuestra estrella materna. Tienen una estructura como cebolla, compuesta por un núcleo compacto de carbono y oxígeno, un envoltorio de hidrógeno muy grande, y entre medio un delgado cascarón de material rico en helio y carente de hidrógeno llamado “intershell”. Estrellas AGB son objetos de masa intermedia (i.e., entre aproximadamente 1 a 8 masas solares) en sus últimas etapas de evolución, poco antes de morir como una enana blanca que se enfría eternamente. Existen muchas dudas e incertezas asociadas con la formación del isótopo ^{13}C en el intershell, que constituye la principal fuente de neutrones para la producción de elementos *s*-process, y con la física detrás de las estrellas AGB en general. Las observaciones de la cantidad de elementos *s*-process en estrellas pueden ser utilizadas para constreñir los modelos teóricos.

En la parte I de esta tesis hemos aplicado por primera vez síntesis de población de estrellas para tratar el problema de la nucleosíntesis de elementos *s*-process en estrellas AGB. Esto consiste en usar modelos sintéticos de evolución estelar para generar poblaciones de estrellas. Cada población estelar es generada con diferentes valores para los parámetros libres de los modelos, lo que permite determinar los valores que mejor reproducen lo que se observa en la naturaleza.

En el capítulo 2, mediante la comparación de nuestros resultados de síntesis de población con observaciones de estrellas con sobreabundancia de elementos *s*-process, encontramos restricciones para los parámetros libres que describen la física detrás de los procesos de mezcla

de elementos *s*-process en la superficie de las estrellas y las propiedades de la fuente de neutrones ^{13}C . Encontramos que la cantidad de ^{13}C que en forma efectiva contribuye a la síntesis de elementos *s*-process tiende a decrecer junto con la metalicidad (i.e., con la proporción de hierro con respecto al hidrógeno) y que esta restringida a un rango menor (aproximadamente un factor 4) que lo que se pensaba hasta ahora (aproximadamente un factor 25 o más). También encontramos que la mezcla de elementos *s*-process hacia la superficie estelar es siempre significativa y que debe ocurrir en estrellas de menor masa inicial que los modelos teóricos predicen.

El estudio del capítulo 2 está hecho con estrellas que pertenecen a nuestra galaxia, sin embargo, en el capítulo 3 analizamos el objeto MACHO 47.2496.8, que no es de nuestra galaxia, sino que de la Nube Grande de Magallanes. Este es hasta ahora la única estrella extra-galáctica disponible con datos de elementos *s*-process suficientemente confiables para realizar nuestro estudio. Encontramos que el mismo set de parámetros libres que funciona para las estrellas de nuestra galaxia en el capítulo 2 también funciona para MACHO 47.2496.8. También vemos reforzado nuestro descubrimiento de una tendencia de los objetos con metalicidad más baja a tener una más baja cantidad de ^{13}C que efectivamente contribuye como fuente de neutrones para la síntesis de elementos *s*-process. A pesar de que para considerar nuestros descubrimientos más concluyentes necesitamos datos de elementos *s*-process de más objetos extra-galácticos, el hecho de que nuestros resultados para objetos galácticos son consistentes con aquellos extra-galácticos sugiere que la validez de nuestros descubrimientos son de carácter universal.

La parte II está enfocada en los parámetros orbitales de sistemas que contuvieron una estrella AGB. Estos sistemas son hoy observados como una enana blanca (la primaria), que fue anteriormente una estrella AGB, y una estrella secundaria, que se encuentra en alguna etapa evolutiva anterior a la fase AGB. La estrella secundaria en estos sistemas muestra elementos *s*-process en su superficie, lo que constituye evidencia de que se ha transferido masa desde la primaria, cuando esta última era una estrella AGB. Muchos de estos sistemas son relativamente cercanos, i.e., tienen una separación orbital comparable al gran tamaño que la primaria tenía cuando era una estrella AGB. Esto implica que la fuerte interacción de fuerzas de marea que debe haber ocurrido disipó cantidades significativas de energía. En consecuencia, una órbita circular se mantiene circular y una elíptica se torna circular. Sin embargo, muchos de estos sistemas relativamente cercanos muestran una excentricidad significativa, que es inexplicable bajo el contexto de sólo considerar mecanismos de disipación de energía. Esto indica que para explicar las observaciones debe existir un mecanismo que aumenta la excentricidad de la órbita. Ejemplos de estos sistemas son las estrellas de bario, que muestran altas abundancias de elementos *s*-process, más prominentemente de bario, y se encuentran en sistemas binarios con enanas blancas. Otro ejemplo, más cercano a nosotros, es el del sistema de Sirio, la estrella más brillante del cielo nocturno, que tiene una órbita en que la distancia más cercana entre los componentes es 4 veces más pequeña que cuando están en la fase más lejana.

Las estrellas AGB pierden mucha masa y tienen un envoltorio extenso y mullido, que puede ser fácilmente influenciado por la fuerza gravitacional de la estrella compañera. En el capítulo 4 proponemos un modelo para sistemas binarios relativamente cercanos donde la pérdida de masa de la estrella AGB se ve aumentada debido a la proximidad de la compañera.

De esta forma, en un sistema con una órbita excéntrica (elíptica), la estrella AGB pierda más masa cuando la secundaria está cerca que cuando la secundaria se encuentra más alejada. Esta pérdida de masa no constante provee de un mecanismo que aumenta la excentricidad orbital de tal forma que compite con la acción circularizante de la disipación de energía por fuerzas de marea. Nosotros mostramos que aplicando este mecanismo es posible explicar la órbita de sistemas como Sirio y muchas estrellas de bario, lo que hasta ahora era muy difícil.

En el capítulo 5 enfocamos nuestra atención en las estrellas de bario con órbitas excéntricas para verificar si nuestro mecanismo que aumenta la excentricidad puede explicar la distribución de período y excentricidad observada en éstas. Los sistemas de estrellas de bario tienen períodos entre aproximadamente 80 a 10000 días y los sistemas excéntricos que tienen períodos más cortos que 3000 días no se pueden explicar bajo las asunciones standard de disipación de mareas. Los sistemas con períodos más cortos que 1000 días deben haber experimentado episodios violentos de transferencia y pérdida de masa, por lo que no tratamos de explicarlos. Realizamos una síntesis de población de estrellas de bario y comparamos nuestros resultados con las observaciones. Encontramos que dentro de asunciones razonables podemos reproducir casi todos los sistemas que están en el rango de 1000–3000 días. Sin embargo, encontramos que comparado con las observaciones hay una sobre-producción de sistemas con períodos más largos que 10000 días, lo que puede ser indicio de que la acreción de masa en sistemas con períodos largos es menos eficiente de lo que se piensa.

Summary

Most elements on Earth which are heavier than iron are synthesised when iron nuclei are exposed to neutrons. Then neutrons are captured by the iron nuclei and decay into protons, transforming the iron into heavier elements. If this decay occurs faster than the neutron capture rate it is called the slow neutron capture process (*s*-process) and the elements synthesised in this way are called *s*-process elements. These elements are used on Earth on a daily basis, such as strontium (e.g., in radiation therapy for cancer), yttrium (e.g., giving the red colour on television screens), zirconium (e.g., cubic zirconia in jewelry, thermal barrier coating), cesium (e.g., drilling fluids for the oil industry, atomic clocks), barium (e.g., X-ray imaging, rat poison), lanthanum (e.g., lighting applications), cerium (e.g., aluminium alloys), among others. The main factory in the Universe of these elements are the Asymptotic Giant Branch (AGB) stars. These stars have a diameter hundreds of times larger than that of the sun and are several tens of thousand times more luminous than our parent star. They have an onion-like structure composed of a compact carbon and oxygen core, an extended hydrogen-rich envelope and a thin shell of hydrogen-exhausted helium-rich material, called intershell, laying in between. AGB stars are intermediate-mass stars (i.e., between about 1 to 8 solar masses) in their last stages of evolution, just before they die as a cooling compact white dwarf. There are still large uncertainties associated with the formation of the ^{13}C isotope in the intershell, which is the main neutron source needed for the synthesis of *s*-process elements, and with the physics of AGB stars in general. Observations of *s*-process element enhancements in stars can be used as constraints on theoretical models.

In part I of this thesis we have applied for the first time a stellar population synthesis technique to address the problem of *s*-process nucleosynthesis in AGB stars. This consists of employing synthetic stellar evolution models to generate populations of stars. Each population is generated with a different set of values for the free parameters of the models, allowing to determine the values with which the models best reproduce the observations of AGB stars.

In chapter 2, by comparing our synthetic population results to observed *s*-process enhanced stars we have found constraints on free parameters describing the physics behind the mixing process of the *s*-process elements into the stellar envelope and properties of the ^{13}C neutron source. We found that the amount of ^{13}C which effectively contributes the *s*-process element synthesis tends to decrease along with the metallicity of the star (i.e., with the stellar ratio of iron to hydrogen) and that it is constrained to a narrower range of values (a factor of about 4) than that believed so far (a factor of more than about 25). We also found that the mixing of

s-process elements into the stellar envelope is always significant and that it should occur in stars of lower initial mass than those predicted by theoretical models.

The study in chapter 2 is carried out by analysing stars that belong to our galaxy. In chapter 3 we analyse the object MACHO 47.2496.8, which is not in our galaxy, but in the Large Magellanic Cloud. This is so far the only extra-galactic star available with reliable *s*-process element data to carry out our study. We found that the same set of free parameters which work for the galactic stars in chapter 2 works also for MACHO 47.2496.8. We also reinforced our findings of a tendency of lower metallicity objects to have a lower amount of ^{13}C which effectively contributes as a neutron source for *s*-process element nucleosynthesis. Although *s*-process element data from more extra-galactic objects is needed to regard our findings as conclusive, the fact that our results for an extra-galactic object are consistent with those for the galactic objects suggests that the validity of our findings has a universal character.

Part II is focused on the orbital parameters of binary systems which contained an AGB star. These systems are today observed to be composed of a white dwarf (the primary), which was formerly the AGB star, and a secondary star, which is in stages of evolution prior to the AGB phase. The secondary star in these systems shows *s*-process elements on its surface, which constitutes evidence of mass transfer from the primary when it was an AGB star. Many of these systems are relatively close, i.e., they have an orbital separation which is comparable to the large size that the primary had when it was an AGB star. This implies that strong tidal interaction must have dissipated significant amounts of orbital energy. As a consequence, an elliptical (called also eccentric) orbit should become circularised. However, many of these relatively close systems show a significant orbital eccentricity, inexplicable when considering only tidal dissipation mechanisms. This indicates that an additional mechanism which enhances the orbital eccentricity must exist in order to explain the observations. Examples of these systems are barium stars, which show overabundances of *s*-process elements, most prominently barium, and they have white dwarf companions. Another example which is closer to us is Sirius, the brightest star in the night-sky, which has such an elliptic orbit that the closest distance between its components is 4 times shorter than when they are the furthest away.

AGB stars lose mass at a high rate and they have an extended and fluffy envelope, which could be easily influenced by the gravitational pull of the companion star. In chapter 4 we propose a model for relatively close binary systems in which the mass loss of the AGB star is enhanced due to the proximity of the secondary star. In this way, in a system with an eccentric orbit, the AGB star loses more mass when the companion is closer by than when it is more distant. This uneven mass-loss along the orbit provides a mechanism which enhances the orbital eccentricity in such a way that it competes with the circularising action of the tidal energy dissipation. We show that by applying this mechanism it is possible to explain the eccentric orbit of systems such as Sirius and of many barium stars, which so far was very difficult.

In chapter 5 we focus the attention on the eccentric orbits of the barium stars to check if our eccentricity pumping mechanism can explain their observed distribution of period and eccentricities. Barium star systems have periods ranging between about 80 and 10000 days and

the significantly eccentric orbits of systems which have a period shorter than 3000 days cannot be explained under the standard assumptions of tidal dissipation. We carry out population synthesis of barium stars and compare with the observations. We find that within reasonable assumptions we can reproduce almost all systems which are in the range of 1000–3000 days. Systems with period shorter than about 1000 days must have experienced violent mass transfer and mass loss, so we do not try to explain them. However, we find an overproduction of systems with larger periods than 10000 days compared to the observations, which may indicate that the accretion at long periods is less efficient than assumed.

Acknowledgements

I would like to thank the following people, which without them I could have never finished this work. Onno Pols for his guidance, teaching, comprehension and for giving me the opportunity of carrying out my PhD studies at Utrecht University. Also thanks for holding that bucket for me, Onno! Rob Izzard, useful discussions about software and physics and also useless discussions about everything else. If we would not have shared the same office, I would still be trying to run that code of yours! Maria Lugaro, your advise and discussions kept me sane during this period. I don't know how longer I will stay like that anyway. Selma de Mink, thanks for the discussions about everything and nothing at the same time, all the Dutch translations you did for me (now the reader knows who to blame!) and also those Cola-breaks to which we owe our sanity. Evert Glebbeek, the hardcore physics and mathematics feedback from you was key in this work, and I guess that that did not contribute to the keep me sane, thanks!. Norbert Langer, Frank Verbout and the whole group of stellar evolution at the Sterrenkundig Instituut Utrecht, thanks for the helpful and insightful discussions. Marion Wijburg, for being always there when I needed help. Also the rest of the people at the institute, for all those nice "canteen and coffee room moments". Richard Stancliffe, for providing and explaining me your models and some other useful tips. Maarten Reyniers and Hans van Winckel, my co-authors in Leuven.

Constanza Gómez and Mark Gieles, one word for you: Bacán! Jan Gerard Dekker and Linda Truijens, you rule! Nate Bastian, the years in the same house and the F-it attitude were "hup!". Kloof and Grindpad, because stress has to be released somehow. My family back in Chile (you're too big to name you all!) for supporting me from the other side of the Atlantic, you are the best. Last but not least at all, I thank my wife, Catalina Arteaga, for putting up with me on the difficult times and for these wonderful years that we had spend together, I love you.

Bibliography

- Abia, C., Busso, M., Gallino, R., et al. 2001, *ApJ*, 559, 1117
- Abia, C., Domínguez, I., Gallino, R., et al. 2002, *ApJ*, 579, 817
- Allen, D. M. & Barbuy, B. 2006, *A&A*, 454, 917
- Anders, E. & Grevesse, N. 1989, *Geochim. Cosmochim. Acta*, 53, 197
- Aoki, W., Ryan, S. G., Norris, J. E., et al. 2002, *ApJ*, 580, 1149
- Barzyk, J. G., Savina, M. R., Davis, A. M., et al. 2007, *Meteoritics & Planetary Science*, accepted
- Bidelman, W. P. & Keenan, P. C. 1951, *ApJ*, 114, 473
- Bisterzo, S., Gallino, R., Straniero, O., et al. 2006, *Memorie della Societa Astronomica Italiana*, 77, 985
- Boffin, H. M. J. & Jorissen, A. 1988, *A&A*, 205, 155
- Bonačić Marinović, A., Izzard, R. G., Lugaro, M., & Pols, O. R. 2007a, *A&A*, 469, 1013
- Bonačić Marinović, A. A., Glebbeek, E., & Pols, O. R. 2007b, submitted to *A&A*
- Bondi, H. & Hoyle, F. 1944, *MNRAS*, 104, 273
- Boothroyd, A. I. & Sackmann, I.-J. 1988, *ApJ*, 328, 632
- Bowen, G. H. 1988, *ApJ*, 329, 299
- Brookshaw, L. & Tavani, M. 1993, *ApJ*, 410, 719
- Busso, M., Gallino, R., Lambert, D. L., Travaglio, C., & Smith, V. V. 2001, *ApJ*, 557, 802
- Busso, M., Gallino, R., & Wasserburg, G. J. 1999, *ARA&A*, 37, 239
- Carraro, G., Girardi, L., Bressan, A., & Chiosi, C. 1996, *A&A*, 305, 849
- Charbonnel, C. & Zahn, J.-P. 2007, *A&A*, 467, L15

- Cole, A. A., Tolstoy, E., Gallagher, III, J. S., & Smecker-Hane, T. A. 2005, *AJ*, 129, 1465
- Cui, W. & Zhang, B. 2006, *MNRAS*, 368, 305
- de Laverny, P., Abia, C., Domínguez, I., et al. 2006, *A&A*, 446, 1107
- de Ruyter, S., van Winckel, H., Maas, T., et al. 2006, *A&A*, 448, 641
- Denissenkov, P. A. & Tout, C. A. 2003, *MNRAS*, 340, 722
- Duquennoy, A. & Mayor, M. 1991, *A&A*, 248, 485
- Eggleton, P. 2006, *Evolutionary Processes in Binary and Multiple Stars (Evolutionary Processes in Binary and Multiple Stars, by Peter Eggleton, pp. . ISBN 0521855578. Cambridge, UK: Cambridge University Press, 2006.)*
- Eggleton, P. P. 1983, *ApJ*, 268, 368
- Eggleton, P. P., Dearborn, D. S. P., & Lattanzio, J. C. 2006, *Science*, 314, 1580
- Frankowski, A. & Tylenda, R. 2001, *A&A*, 367, 513
- Frost, C. A. & Lattanzio, J. C. 1996, *ApJ*, 473, 383
- Gallino, R., Arlandini, C., Busso, M., et al. 1998, *ApJ*, 497, 388
- Gatewood, G. D. & Gatewood, C. V. 1978, *ApJ*, 225, 191
- Gilroy, K. K. 1989, *ApJ*, 347, 835
- Giridhar, S. & Arellano Ferro, A. 2005, *A&A*, 443, 297
- Goldstein, H. 1980, *Classical mechanics (Classical mechanics (2nd ed.) by H. Goldstein. Addison-Wesley Series in Physics, 1980)*
- Goriely, S. & Mowlavi, N. 2000, *A&A*, 362, 599
- Groenewegen, M. A. T. & de Jong, T. 1993, *A&A*, 267, 410
- Han, Z., Eggleton, P. P., Podsiadlowski, P., & Tout, C. A. 1995, *MNRAS*, 277, 1443
- Han, Z., Podsiadlowski, P., & Eggleton, P. P. 1994, *MNRAS*, 270, 121
- Herwig, F. 2005, *ARA&A*, 43, 435
- Herwig, F., Bloeker, T., Schoenberner, D., & El Eid, M. 1997, *A&A*, 324, L81
- Herwig, F., Langer, N., & Lugaro, M. 2003, *ApJ*, 593, 1056
- Hollowell, D. & Iben, I. J. 1988, *ApJ Lett.*, 333, L25

- Hurley, J. R., Pols, O. R., & Tout, C. A. 2000, MNRAS, 315, 543
- Hurley, J. R., Tout, C. A., & Pols, O. R. 2002, MNRAS, 329, 897
- Hut, P. 1981, A&A, 99, 126
- Iben, Jr., I. 1977, ApJ, 217, 788
- Iben, Jr., I. & Renzini, A. 1983, ARA&A, 21, 271
- Iben, I. J. & Livio, M. 1993, PASP, 105, 1373
- Izzard, R. G., Dray, L. M., Karakas, A. I., Lugaro, M., & Tout, C. A. 2006, A&A, 460, 565
- Izzard, R. G., Tout, C. A., Karakas, A. I., & Pols, O. R. 2004, MNRAS, 350, 407
- Jahanara, B., Mitsumoto, M., Oka, K., et al. 2005, A&A, 441, 589
- Jorissen, A., Frayer, D. T., Johnson, H. R., Mayor, M., & Smith, V. V. 1993, A&A, 271, 463
- Jorissen, A. & Mayor, M. 1988, A&A, 198, 187
- Jorissen, A., Van Eck, S., Mayor, M., & Udry, S. 1998, A&A, 332, 877
- Karakas, A. I., Lattanzio, J. C., & Pols, O. R. 2002, PASA, 19, 515
- Karakas, A. I., Tout, C. A., & Lattanzio, J. C. 2000, MNRAS, 316, 689
- Karovska, M., Schlegel, E., Hack, W., Raymond, J. C., & Wood, B. E. 2005, ApJ Lett., 623, L137
- Kippenhahn, R. & Weigert, A. 1990, Stellar Structure and Evolution (Stellar Structure and Evolution, XVI, 468 pp. 192 figs.. Springer-Verlag Berlin Heidelberg New York. Also Astronomy and Astrophysics Library)
- Kroupa, P., Tout, C. A., & Gilmore, G. 1993, MNRAS, 262, 545
- Langer, N., Heger, A., Wellstein, S., & Herwig, F. 1999, A&A, 346, L37
- Lattanzio, J. C. 1989, ApJ Lett., 344, L25
- Liang, Y. C., Zhao, G., Chen, Y. Q., Qiu, H. M., & Zhang, B. 2003, A&A, 397, 257
- Liu, J. H., Zhang, B., Liang, Y. C., & Peng, Q. H. 2000, A&A, 363, 660
- Lugaro, M., Herwig, F., Lattanzio, J. C., Gallino, R., & Straniero, O. 2003, ApJ, 586, 1305
- Malaney, R. A. & Lambert, D. L. 1988, MNRAS, 235, 695
- Marhas, K. K., Hoppe, P., & Ott, U. 2007, Meteoritics & Planetary Science, accepted

- Marigo, P. 2002, *A&A*, 387, 507
- Marigo, P., Girardi, L., & Bressan, A. 1999, *A&A*, 344, 123
- McClure, R. D. 1984, *PASP*, 96, 117
- McClure, R. D., Fletcher, J. M., & Nemeč, J. M. 1980, *ApJ Lett.*, 238, L35
- McClure, R. D. & Woodsworth, A. W. 1990, *ApJ*, 352, 709
- Meixner, M., Gordon, K. D., Indebetouw, R., et al. 2006, *AJ*, 132, 2268
- Merrill, S. P. W. 1952, *ApJ*, 116, 21
- Meyer, B. S. 1994, *ARA&A*, 32, 153
- Meyer, F. & Meyer-Hofmeister, E. 1983, *A&A*, 121, 29
- Mowlavi, N. 1999, *A&A*, 344, 617
- Nagae, T., Oka, K., Matsuda, T., et al. 2004, *A&A*, 419, 335
- Nelemans, G. & Tout, C. A. 2005, *MNRAS*, 356, 753
- Nelemans, G., Verbunt, F., Yungelson, L. R., & Portegies Zwart, S. F. 2000, *A&A*, 360, 1011
- Paczyński, B. 1970, *AcA*, 20, 47
- Pastetter, L. & Ritter, H. 1989, *A&A*, 214, 186
- Pollard, K. R. & Lloyd Evans, T. 2000, *AJ*, 120, 3098
- Pols, O. R., Karakas, A. I., Lattanzio, J. C., & Tout, C. A. 2003, in *Astronomical Society of the Pacific Conference Series*, Vol. 303, *Astronomical Society of the Pacific Conference Series*, ed. R. L. M. Corradi, J. Mikolajewska, & T. J. Mahoney, 290–+
- Pols, O. R., Schroder, K.-P., Hurley, J. R., Tout, C. A., & Eggleton, P. P. 1998, *MNRAS*, 298, 525
- Pont, F. & Eyer, L. 2004, *MNRAS*, 351, 487
- Rasio, F. A., Tout, C. A., Lubow, S. H., & Livio, M. 1996, *ApJ*, 470, 1187
- Reimers, D. 1975, *Circumstellar envelopes and mass loss of red giant stars (Problems in stellar atmospheres and envelopes.)*, 229–256
- Reyniers, M., Abia, C., van Winckel, H., et al. 2007, *A&A*, 461, 641
- Reyniers, M. & van Winckel, H. 2007, *A&A*, 463, L1
- Reyniers, M., Van Winckel, H., Gallino, R., & Straniero, O. 2004, *A&A*, 417, 269

- Ritter, H. 1988, *A&A*, 202, 93
- Siess, L., Goriely, S., & Langer, N. 2004, *A&A*, 415, 1089
- Smiljanic, R., Porto de Mello, G. F., & da Silva, L. 2007, *A&A*, 468, 679
- Smith, V. V. & Lambert, D. L. 1990, *ApJS*, 72, 387
- Soker, N. 2000, *A&A*, 357, 557
- Soker, N. 2006, *New Astronomy*, 11, 396
- Stancliffe, R. J., Glebbeek, E., Izzard, R. G., & Pols, O. R. 2007, *A&A*, 464, L57
- Stancliffe, R. J., Izzard, R. G., & Tout, C. A. 2005, *MNRAS*, 356, L1
- Stancliffe, R. J., Tout, C. A., & Pols, O. R. 2004, *MNRAS*, 352, 984
- Stephenson, C. B. 1989, *Publications of the Warner & Swasey Observatory*, 3, 53
- Straniero, O., Chieffi, A., Limongi, M., et al. 1997, *ApJ*, 478, 332
- Straniero, O., Domínguez, I., Cristallo, R., & Gallino, R. 2003, *PASA*, 20, 389
- Theuns, T., Boffin, H. M. J., & Jorissen, A. 1996, *MNRAS*, 280, 1264
- Tout, C. A. & Eggleton, P. P. 1988, *MNRAS*, 231, 823
- Travaglio, C., Galli, D., Gallino, R., et al. 1999, *ApJ*, 521, 691
- van den Bos, W. H. 1960, *Journal des Observateurs*, 43, 145
- van der Sluys, M. V., Verbunt, F., & Pols, O. R. 2006, *A&A*, 460, 209
- van Eck, S., Goriely, S., Jorissen, A., & Plez, B. 2003, *A&A*, 404, 291
- van Winckel, H. 2003, *ARA&A*, 41, 391
- Van Winckel, H. & Reyniers, M. 2000, *A&A*, 354, 135
- Van Winckel, H., Waelkens, C., & Waters, L. B. F. M. 1995, *A&A*, 293, L25
- Vassiliadis, E. & Wood, P. R. 1993, *ApJ*, 413, 641
- Verbunt, F. & Phinney, E. S. 1995, *A&A*, 296, 709
- Waelkens, C., Van Winckel, H., Waters, L. B. F. M., & Bakker, E. J. 1996, *A&A*, 314, L17
- Waters, L. B. F. M., Cami, J., de Jong, T., et al. 1998, *Nature*, 391, 868
- Zacs, L. 1994, *A&A*, 283, 937

Zahn, J.-P. 1977, *A&A*, 57, 383

Zahn, J.-P. & Bouchet, L. 1989, *A&A*, 223, 112

Zinner, E., Nittler, L. R., Gallino, R., et al. 2006, *ApJ*, 650, 350